



HAL
open science

Rotational mechanical effects driven by the transfer of the acoustic orbital angular momentum

Benjamin Sanchez Padilla

► **To cite this version:**

Benjamin Sanchez Padilla. Rotational mechanical effects driven by the transfer of the acoustic orbital angular momentum. Physics [physics]. Université de Bordeaux, 2019. English. NNT : 2019BORD0452 . tel-02890688

HAL Id: tel-02890688

<https://theses.hal.science/tel-02890688>

Submitted on 6 Jul 2020

HAL is a multi-disciplinary open access archive for the deposit and dissemination of scientific research documents, whether they are published or not. The documents may come from teaching and research institutions in France or abroad, or from public or private research centers.

L'archive ouverte pluridisciplinaire **HAL**, est destinée au dépôt et à la diffusion de documents scientifiques de niveau recherche, publiés ou non, émanant des établissements d'enseignement et de recherche français ou étrangers, des laboratoires publics ou privés.

THÈSE PRÉSENTÉE
POUR OBTENIR LE GRADE DE
DOCTEUR DE
L'UNIVERSITÉ DE BORDEAUX

ÉCOLE DOCTORALE DES SCIENCES PHYSIQUES DE L'INGÉNIEUR
SPÉCIALITÉ : LASER, MATIÈRE ET NANOSCIENCES

Par Benjamin SANCHEZ PADILLA

TITRE
Rotational mechanical effects driven
by the transfer of acoustic orbital angular momentum

Sous la direction de : Etienne BRASSELET

Soutenue le 20 Décembre 2019

Membres du jury :

Mme. VOLKE-SEPULVEDA, Karen
M. THOMAS, Jean-Louis
M. WUNENBURGER, Régis
M. BARESCH, Diego
M. POULIGNY, Bernard
M. BRASSELET, Etienne

Associate professor
Directeur de recherche
Professeur des universités
Chargé de recherche
Directeur de recherche
Directeur de recherche

Rapporteur
Rapporteur
Examineur
Examineur
Examineur
Directeur de thèse

Titre : Effets mécaniques rotationnels pilotés par le moment angulaire angulaire orbital des ondes sonores

Résumé :

Ce travail de thèse traite des effets mécaniques rotationnels résultant de l'interaction son-matière en présence de transfert de moment angulaire de nature orbitale. Deux approches expérimentales sont mises en œuvre, toutes deux utilisant des ondes ultrasonores se propageant dans l'air et des objets de taille centimétrique obtenus par impression 3D imprimés et se comportant comme des miroirs structurés imprimant un profil de phase hélicoïdal au champ réfléchi. Le résultat principal consiste en la mesure directe quantitative du moment angulaire orbital porté par un faisceau vortex via deux approches indépendantes. La première est basée sur l'utilisation d'un miroir hélicoïdal placé à l'interface air-eau, et la seconde repose sur le développement d'un oscillateur mécanique de torsion forcé par le transfert de moment angulaire.

Mots clés : Moment angulaire, Vortex, Acoustique

Title : Rotational mechanical effects driven by the transfer of the acoustic orbital angular momentum

Abstract :

We study the rotational mechanical effects resulting from sound-matter interaction in the presence of orbital angular momentum transfer. A set of experimental realizations are implemented by using ultrasonic waves propagating in the air and 3D printed centimeter-sized objects acting as structured mirrors imparting a helical phase profile to the reflected wave. The main result consists of the quantitative direct measurement of the orbital angular momentum carried by acoustic vortex beams via two independent approaches. The first one is based on the use of a freely rotating helical mirror placed at air-water interface, and the second one relies on the development of a torsional mechanical oscillator driven by acoustic orbital angular momentum.

Keywords : Angular Momentum, Vortex, Acoustic

Laboratoire Ondes et Matière d'Aquitaine, UMR 5798

351 Cours de la Libération, bâtiment A4N, 33400 Talence

Preamble

As the thesis title suggests, I dedicated my PhD work to the interaction of sound with matter in presence of acoustic orbital angular momentum. However, prior to be involved in the topic of acoustics, I dedicated the first 6 months of my PhD years to the study of the diffraction of light through a novel class of refractive optical elements in collaboration with Vilnius University (Lithuania) that resulted in the publication of an article published in 2016 [1]. These optical elements are high-order axicons obtained by introducing cusp deformation (wrinkles) to the conical surface of an usual axicon, which leads to geometrical singularities (cusps). These axicons fabricated at the micron scale by femtosecond laser photopolymerization technique are characterized by transverse cross-section profile belonging to the families of hypocycloids and epicycloids. Experimental study of light propagation after it has passed through these elements has been reported and supported by numerical simulations in the paraxial regime. Also, the effects of spin-orbit interaction of light due to the nonparaxial nature of the diffracted light have been numerically investigated using finite-differences time domain (FDTD) simulations. This allows discussing the relationship between the topology of the contour associated to the wrinkled axicon and the generated optical phase singularities. Concretely, this study was the continuation of a previous study made at LOMA a few years before [2] where the role of contour topology of close-paths was discussed in the context of spin-orbit optical vortex generation. Even though this work is not the core of my thesis and would hardly find a logical place nearby the acoustic developments I carried out, it was my introduction to research in experimental physics. Because of that, I decided to add it as an Appendix at the end of the thesis with a reproduction of the corresponding published results.

Contents

Preamble	2
1 Introduction	4
1.1 Emergence of phase singularities in waves	4
1.2 Phase singularities: the early days	5
1.3 Orbital angular momentum associated with phase singularities . .	11
1.4 Detection and measurement of the orbital angular momentum of sound	13
1.4.1 Dissipative process	14
1.4.2 Non-dissipative process	16
2 Sound-matter system: definition and characterization	18
2.1 Sound-matter reflective geometry	18
2.2 Helical mirror	19
2.2.1 Design	19
2.2.2 3D printing modelling: design	22
2.2.3 3D Printing	25
2.2.4 Validation of printed helical mirrors	28
2.3 Acoustic source: modelling	30
2.3.1 Analytical results	30
2.3.2 Numerics: beam propagation method	32
2.3.3 Gaussian-field approximation	34
2.4 Acoustic source: experiments	35
2.4.1 Power characterization	37
3 Orbital acoustomechanics: a spinning experiment	42
3.1 Preliminary experiments	42
3.1.1 Preparing the experimental set-up	42
3.1.2 Qualitative observation of spinners	43

3.2	Towards a quantitative description	46
3.2.1	The particular case of $\ell = 1$	47
3.3	Influence of the topological charge	49
3.4	Determination of the acoustic torque	50
3.4.1	General consideration	50
3.4.2	Viscous torque corrections: a comment	53
3.5	Improving the experimental implementation	55
3.5.1	Upgrading experimental setup	55
3.5.2	Defining the appropriate Glycerol-Water mixture	56
3.6	Quantitative measurements: first attempt	58
3.7	Quantitative measurement: final attempt	61
3.7.1	Improvement of experimental setup	61
3.7.2	Acoustic torque measurement	63
3.8	Discussion of the power mismatch between theory and experiment	68
4	Orbital acoustomechanics: a torsional pendulum experiment	70
4.1	Theoretical background: predictions	71
4.2	Preliminary experiments	74
4.2.1	Definition of a pendulum design	74
4.2.2	3D printing: design and fabrication	75
4.2.3	Experimental setup	77
4.2.4	First observations	79
4.2.5	Quantitative analysis: setup and acquisition	81
4.2.6	Data extraction and preliminary analysis	82
4.3	Towards quantitative experiments	83
4.3.1	Improved data processing	83
4.3.2	Benchmarking the modulated source: model	84
4.3.3	Benchmarking the modulated source: experiment	86
4.3.4	Optimal pendulum design	87
4.4	Acoustic torque measurements	89
A	Wrinkle Axicons	96
	Bibliography	109

Introduction

1.1 Emergence of phase singularities in waves

A wave is an energy transport phenomenon generated by the perturbation of a medium or a field that evolves in time and space. The amplitude of a scalar wave is described in complex notation as

$$\Psi(\mathbf{r}, t) = \rho(\mathbf{r}, t)e^{i\theta(\mathbf{r}, t)} \quad (1.1)$$

where ρ is the magnitude, θ is the phase, \mathbf{r} is the position vector and t is the time. The magnitude and phase functions depend of the geometry, the nature of the source and the medium in which the wave propagates, making the wave propagation a non trivial problem in most of the real cases. Noteworthy, inhomogeneous wave structures emerge even in simple ideal cases such as the interference of a finite number of monochromatic plane waves. The plane wave is the idealization of a perturbation, often used as the basis of any oscillating phenomenon. It is characterized by its infinite spatial extension, a constant amplitude $\rho = \rho_0$, and a phase of the form $\theta = \mathbf{k} \cdot \mathbf{r} - \omega t$, where \mathbf{k} is the wave vector with magnitude $|\mathbf{k}| = 2\pi/\lambda$, λ is the wavelength, and ω is the angular frequency. Namely,

$$\Psi(\mathbf{r}, t) = \rho_0 e^{i(\mathbf{k} \cdot \mathbf{r} - \omega t)} \quad (1.2)$$

It is well known that the coherent superposition of two monochromatic plane waves differing only by their propagation direction leads to interference fringes, see Fig. 1.1(first column) where the spatial distribution of intensity and phase are shown in a given observation plane. Non-zero intensity regions exhibit continuous values of the phase that run between 0 and 2π along the interference fringes. In contrast, the phase is undefined along the lines of zero intensity, which corresponds to a π phase step and a change of sign of the amplitude in a direction perpendicular to the fringes. As the number of interfering plane waves

increases, another kind of phase discontinuities appear: phase singularities, see Fig. 1.1(second column). They are points of zero intensity associated to a local phase dependency characterized by an integer number $\ell = \pm 1$, called *topological charge*, which is defined as the line integral of a close loop inscribing the singularity

$$\ell = \frac{1}{2\pi} \oint d\theta = \frac{1}{2\pi} \oint \theta'(\varphi) d\varphi \quad (1.3)$$

The sign of ℓ defines the handedness of the helical wavefront in the neighbourhood of the singularity. See Fig. 1.2 that illustrates the wavefront for the case of right-handed ($\ell > 0$), left-handed ($\ell < 0$) and a plane ($\ell = 0$) wave. The case of interference between three plane waves is illustrated in Fig. 1.1(second column). As the number of waves further increases, the intensity field increases in complexity and the position of the singularities becomes random. However, the topological charge of the singularities remains $\ell = \pm 1$. This is depicted in in Fig. 1.1(third column) for $N = 10$. In practice, one can experience the emergence of phase singularities in the speckle field obtained, for instance, from the diffuse reflection of a laser beam, or the reflection of an ultrasonic pulse from a rough surface.

In the next section we introduce the origin of the study of phase singularities and the formation of helical wavefronts, also known as screw phase dislocations, starting from their first detection. Then, the formation of artificially engineered high-order phase singularities is introduced, motivated by its connection with the orbital angular momentum carried by a propagating wave. Then, we review the studies of phase singularities in the area of acoustics and their use related with the transfer of orbital angular momentum of sound. Finally, we provide a survey of the state of the art regarding the techniques of detection and measurement of transfer orbital angular momentum via dissipative and non dissipative processes.

1.2 Phase singularities: the early days

The study of phase singularities could be traced from the early days of radio-echoing, a technique used to estimate the shape and distance via the time delay of radio signals. In the 1960s, the technique of radio-echoing started to be used as a method to measure the thickness of Antarctic ice sheets as the change of

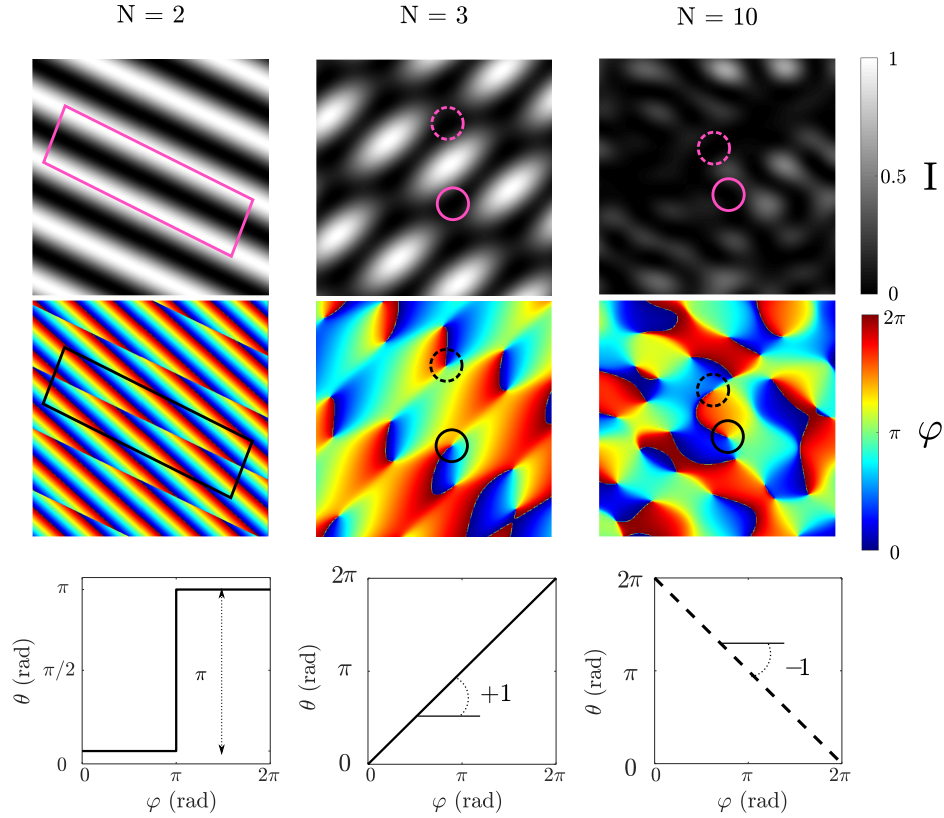


Figure 1.1: Amplitude and phase of the interference pattern between $N = 2, 3$ and 10 plane waves with random magnitudes and random propagation directions. Left: $N = 2$. The intensity field shows stripes of zero amplitude that extend along the lines of phase dislocations. Perpendicular to the interference stripes, the phase exhibits a shift of π between stripes. Middle: $N = 3$. The emergence of singularities of charge $\ell = \pm 1$ starts, shown as points of null intensity in the intensity field. Right: $N = 10$. Although the complexity of the intensity and phase fields increase with N , the values of the topological charge of the singularities remain $\ell = \pm 1$.

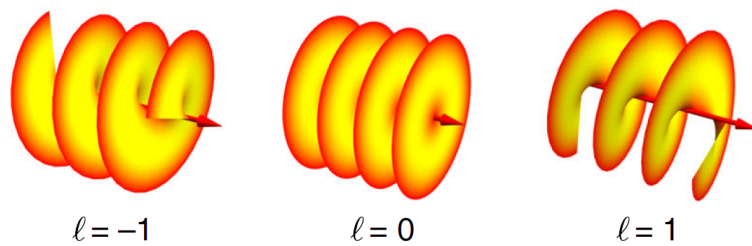


Figure 1.2: Illustration of wavefronts of waves carrying a phase singularity with topological charge $\ell = (-1, 0, +1)$. Adapted from [3].

thickness reflects, indirectly, the change of the world climate and the worldwide sea level. Prior to this technique, the first methods to detect the thickness of the ice sheets consisted in the placement of an inland station at the South Pole and detect the local rate of change of gravity, and interpret this change in term of the increase or decrease of the thickness of the ice sheet. It was proved later that 90% of the values measured were mostly due to the sinking of the station [4]. Later, the use of radio-echoing was proposed as a more accurate method of measurement. The implementation of this method proved to give a good rate of successful results during the expeditions to Antarctica as reported by Robin et al. in his expedition carried out in 1964 [5]. During that expedition, a distortion of the spatio-temporal shape of the reflected radio signal, coined *spatial fading pattern*, was reported.

In the early 1970s, Nye et al. [6] performed a laboratory analogue experiment using ultrasonic waves instead of radio waves. The experiment consisted in a scaled-down experiment using an ultrasonic pulse source and an aluminium foil that allowed mimicking the radio pulses and the bedrock surface. The sensitivity of the experiments allowed a detailed study of the phase, and wavefront dislocations were observed as points of zero intensity. Two years later, Nye and Berry [7] understood that these dislocations result from the interference of a number of waves derived from the same source and propagating with different directions, as it happens in a scattering problem, which can induce a sudden changes in the phase of the wave. In the area of optics, Baranova et al. [8] studied the emergence of similar phase singularities in inhomogeneous optical waves characterized by the existence of points with zero amplitude in a plane, which form lines in three dimensions. This was experimentally confirmed by interfering two laser beams from the same source, one with the wavefront distorted by means of a non-uniform phase plate simulating a speckled field, and the other one working as a reference field [9]. Experimental results of interference of speckled field with tilted reference wave observed by Baranova et al. [10] are depicted in Fig. 1.3. Once the theoretical foundations of phase singularities have been established, multiple methods to modulate on demand the wave front in a singular manner were developed. The most straightforward option is the use of a spiral phase plate. A spiral phase plate is a screw-like dislocated 3D plate that imparts a phase profile $\phi = \phi(\varphi)$ to the wave that interact with it, where φ is the azimuthal angle. The mechanism through which the spiral phase plate introduces the screw-like

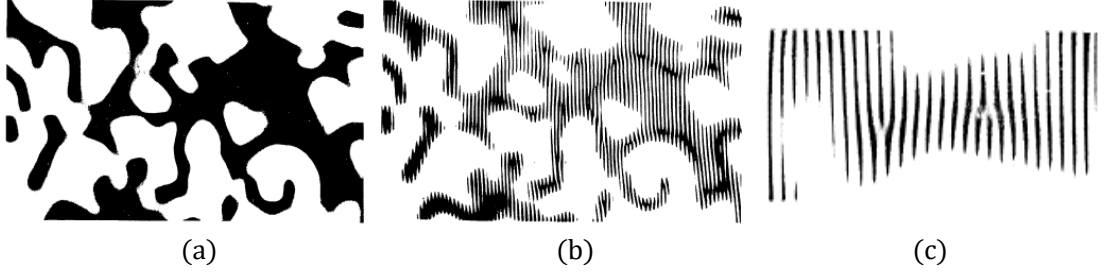


Figure 1.3: (a) Speckle pattern of laser light source. (b) Same pattern modulated by the interference with a tilted reference wave. (c) Zoom on two phase singularities having opposite topological charge. Adapted from [10].

phase to a wave could be classified accordingly to the following process: transmission, reflection and emission. Noteworthy, these mechanisms are associated with distinct height of the spiral step in order to introduce a phase singularity with topological charge ℓ . Considering the propagation of a scalar wave at normal incidence onto a spiral phase plate, the step height is $h_s = \frac{\ell}{f} \left| \left(\frac{1}{c_1} - \frac{1}{c_0} \right)^{-1} \right|$ in transmission and $h_s = \frac{\ell c_0}{2f}$ in reflection, with f the wave frequency, c_1 the phase velocity in the plate and c_0 the phase velocity in the medium surrounding the plate. In emission, the spiral wave generator has a step height of $\ell\lambda$.

In the area of electromagnetism, an early report of helicoidal spatial phase modulators was done by Bryngdahl in 1973 while studying the interference fringes of optical elements with radial and angular phase dependencies [11]. Fresnel-lens-type were designed to simulate the phase of an helicoidal shape filter. Surprisingly, the use and study of spiral phase plates as elements introducing azimuthal-dependent phase delays has been popularized only two decades later. One can cite the work of Khonina et al. [12] in which they report the creation of a *phase rotor filter* by lithographic technique, an optical element whose complex transmittance linearly depends on the azimuthal angle. Also, there is the work of Kristensen et al. of 1993 for microwaves in a cavity, where the key intracavity element is an helicoidal plate made of teflon [13]. Also, in 1994 Beijersbergen et al. implemented the use of a spiral phase plate to convert a TEM_{00} visible laser beam into a beam with helicoidal wavefront [14]. This was made by fabricating a monolithic spiral phase plate from a transparent acrylic plate using a milling tool to remove the material radially. The fabrication challenges associated to smaller wavelengths were overcome as the nanofabrication technology evolved. This can be illustrated by the work of Peele et al. in 2002, who used an spiral

phase plate built by photomask projection micromachining to introduced a spiral phase distribution to incident x-ray waves [15]. Other ranges of the electromagnetic spectrum have been studied such as the GHz and THz domains. In the GHz range we mention the work of Tamburini et al. [16] in which they used a split parabolic antenna to introduce a screw-like phase to radio waves. In the THz range, there is for instance the work of Miyamoto et al., in which they used a spiral phase plate mechanically carved in Tsurupica material [17]. A visual summary of spiral phase plates for electromagnetic waves from radio-waves to X-rays is shown in Fig. 1.4.

In the area of acoustics, Berry told us that, to his knowledge, the first experimental demonstration of a controlled dislocation was done by his colleague Walford around 1974. By sending an ultrasonic beam to a cardboard cut in helicoidal shape with a pitch of half-wavelength, see Fig. 1.5(a), he detected intensity changes of the reflected wave that are associated with the generation of an ultrasonic vortex beam with unit topological charge. In 1999, Hefner and Marston [18] used a cut annular sheet of polyvinylidene fluoride adopting a spiral shape and attached it to an acoustic transducer. This acoustic source immersed in a water tank and emitting waves at 300 kHz generated an intensity distribution similar to a Laguerre-Gaussian beam, see Fig. 1.5(b). In 2004, Gspan et al. [19] used an absorbing material carved with the desired helical shaped and irradiated by light pulses. Due to the thermal expansion of the material, acoustic wave pulses with a screw-like wavefront are generated, see Fig. 1.5(c). In 2015, Wunenburger et al. [20], introduced a screw dislocation to a transmitted focused ultrasonic wave using a 3D printed plastic spiral phase plate, see Fig. 1.5(d). In

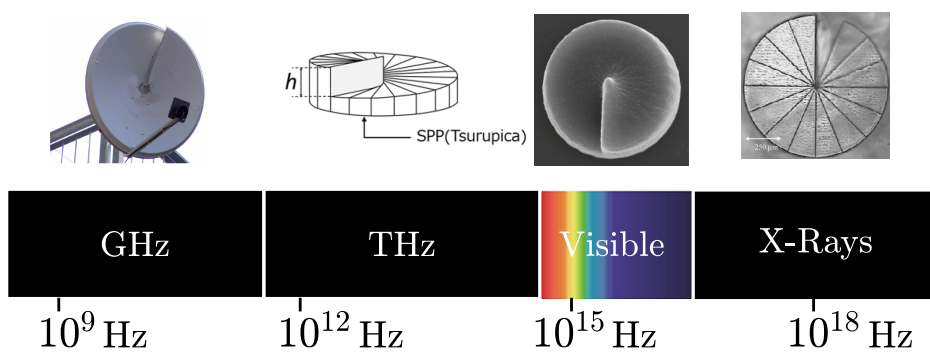


Figure 1.4: Summary of electromagnetic spiral phase plates implemented over a very broad range of frequencies covering radio waves to X-rays.

this thesis, by using a 3D printed monolithic spiralling structures, we introduce phase singularities by reflection, see Fig. 1.5(e), which will be discussed in detail in the chapter 2.

Although there are other techniques to introduce phase singularities to a field, such as the use of holographic masks fabricated via computer-synthesized gratings, see [21, 22], here we restrict our presentation to spiral phase plates since the latter corresponds to the specific framework of this thesis. Finally, it is interesting to note that shaping the structure of waves using spiral phase plates has also been extended to situation other than electromagnetism and acoustics. Namely, shaping phase singularities for electron and neutron wave functions have been realized in recent years using appropriate materials, see [23] and [24] respectively.

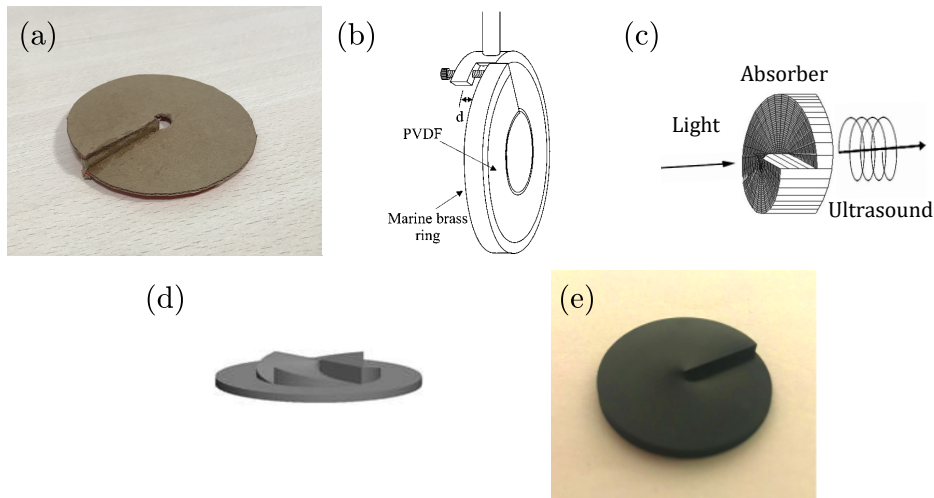


Figure 1.5: (a) Personal reconstruction of the spiral phase plate originally built by Walford around 1974 according to Berry. (b) Sketch of the acoustic transducer used by Hefner et al. formed by an annular sheet of polyvinylidene fluoride (PVDF) cut as a spiral. Adapted from [18]. (c) Scheme of spiral phase plate absorber for optically-generated sound pulses. Adapted from [19]. (d) 3D printed spiral phase plate mask used for ultrasonic transmission vortex generation in fluids. Adapted from [20]. (e) 3D printed acoustic helical mirror that is further used in this thesis (further details are given in chapter 2), enabling reflective acoustic vortex generation in air.

1.3 Orbital angular momentum associated with phase singularities

The concept of waves carrying angular momentum is rather old. In the area of optics, Sadovsky [25] and Poynting [26] independently predicted the existence angular momentum for circular polarized light. In the area of quantum mechanics, it was proved that the amount of angular momentum is associated to the spin of the photon. This was tested experimentally by Beth [27] in 1936 by exploiting the mechanical consequences of the polarization state changes as circular polarized light passes through a half wave plate. By placing the half-wave plate at the tip of a torsion pendulum, Beth detected and measured the spin angular momentum of light. Indeed, the resulting net change of spin angular momentum per photon by an amount of $\pm 2\hbar$ (the sign corresponds to the input handedness of the circularly polarized light) leads to a torque exerted by the light on the half-wave plate, as depicted in Fig. 1.6(a). Much later, in 1992, Allen et al. [28], inspired by the results of Beth and the analogy between quantum mechanics and paraxial optics, established theoretically that electromagnetic waves with an azimuthal dependency of its amplitude of the form $\exp(i\ell\varphi)$ carries an angular momentum per photon equal to $\ell\hbar$. The demonstration was performed by considering the so-called Laguerre-Gaussian modes, that form a complete and exact basis of the paraxial field in a cylindrical coordinate system. The complex amplitude of these modes, that are characterized by two indices $\ell \in \mathbb{Z}$ and $p \in \mathbb{N}$, have the following expression (assuming propagation along z axis towards $z > 0$)

$$\begin{aligned}
 A_{\ell,p}(r, \varphi, z, t) &= \frac{C_{\ell,p}}{w(z)} \left(\frac{r\sqrt{2}}{w(z)} \right)^{|\ell|} L_p^\ell \left(\frac{2r^2}{w^2(z)} \right) \\
 &\times \exp \left[-\frac{r^2}{w^2(z)} + \frac{ikr^2z}{2(z^2 + z_R^2)} \right] \\
 &\times \exp[-i(2p + |\ell| + 1)\zeta(z)] \exp(i\ell\varphi - i\omega t + kz)
 \end{aligned} \tag{1.4}$$

where $C_{\ell,p} = \sqrt{2p! / (\pi(p + |\ell|)!)}$ is a normalization constant, $L_p^\ell(\cdot)$ is the generalized Laguerre-Gauss polynomial with radial index p and azimuthal index ℓ , $\zeta(z) = \tan^{-1}(z/z_R)$ is the Gouy phase of the fundamental Gaussian beam, $w(z) = w_0\sqrt{1 + (z/z_R)^2}$ is the beam radius, w_0 is the beam waist, and $z_R = \pi w_0^2/\lambda$ is the Rayleigh range. Noteworthy, for $\ell \neq 0$, a Laguerre-Gaussian beam carries on-axis optical phase singularity. The intensity and phase distribution of a few

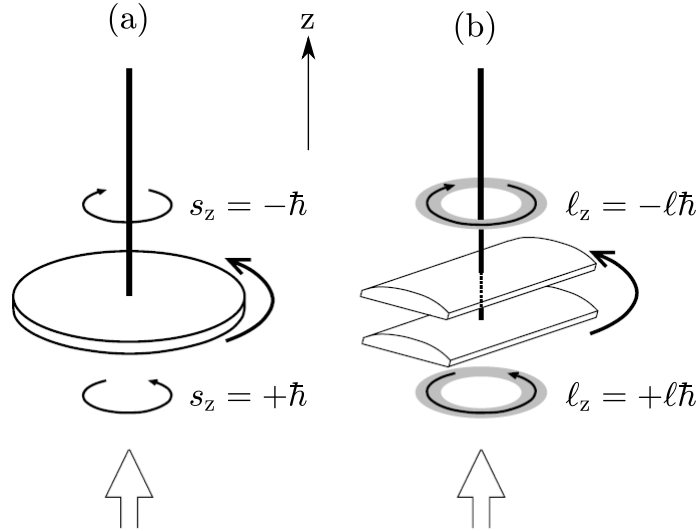


Figure 1.6: Illustration of the experiment by Beth for spin angular momentum detection (a) and the analogue suggested experiment by Allen et al. for orbital angular momentum detection (b) experiments. (a) A $\lambda/2$ birefringent plate experiences a torque as the incident spin angular momentum (have \hbar per photon) carried by a circular polarized light is flipped. (b) A set of cylindrical lenses acting as a Laguerre-Gaussian converter is expected to experience a torque as the incident orbital angular momentum (have $\ell\hbar$ per photon) carried by a Laguerre-Gaussian beam mode of azimuthal order ℓ is flipped. Adapted from [28].

Laguerre-Gaussian modes are shown in Fig. 1.7. Importantly, the nature of this angular momentum differs from the spin one. In fact, this momentum is of an orbital nature, hence associated with spatial degrees of freedom, in contrast to the spin angular momentum related to the polarization state of light. Moreover, Allen et al. proposed an experimental analogy with respect to the work by Beth in order to detect and measure the mechanical effect of the transfer of orbital angular momentum from light to matter, as illustrated in Fig. 1.6(b). The idea is to suspend a Laguerre-Gaussian mode converter made from a pair of cylindrical lenses hanging at the tip of a torsion wire. As a Laguerre-Gaussian beam of order ℓ passes through the converter, light transfers a net amount of $2\ell\hbar$ per photon to the material system as the azimuthal order of the incident beam is flipped from ℓ to $-\ell$. This result triggered a growing interest regarding possible applications of phase singularities, when mechanical effects come at play. In the area of optics, this was beneficial for the development of optical manipulation techniques, see [29] for a review. However, it is in the acoustic domain that we are focusing our interest in this thesis and we further deal with developments made in acoustics.

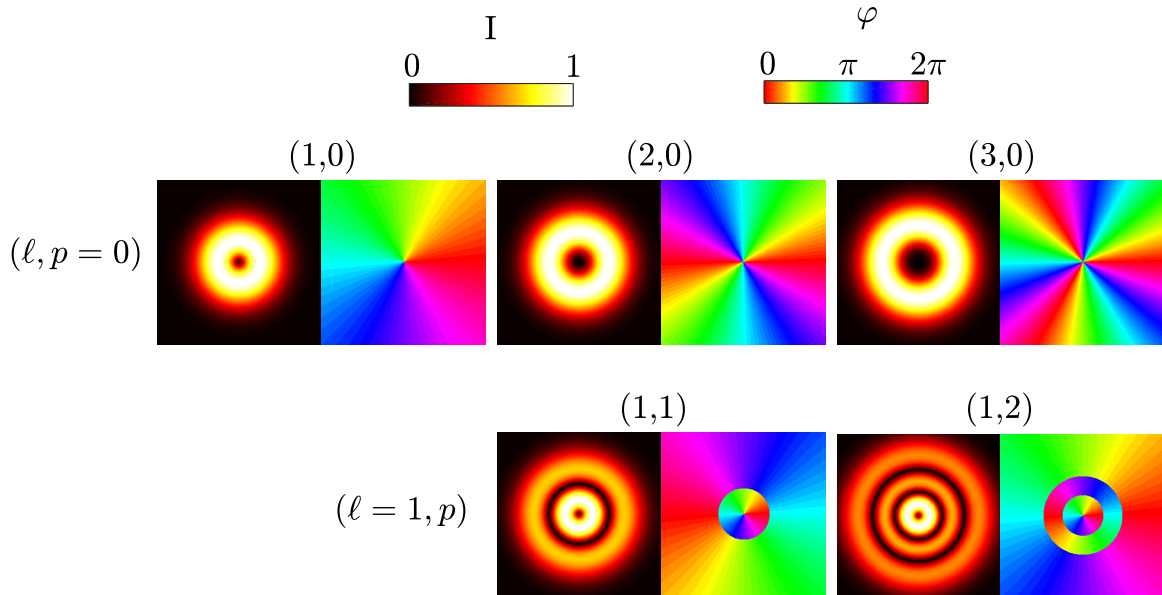


Figure 1.7: Intensity and phase of a few Laguerre-Gaussian beam modes at $z = 0$, for different values of p and ℓ .

In acoustics, helical wavefronts were reintroduced by Hefner & Marston [30] in 1998 while calculating the flux of orbital angular momentum of acoustic beams cylindrical symmetrical with azimuthal phase dependency of $\exp(i\ell\varphi)$, in particular the Laguerre-Gaussian beams. In 2003, Thomas & Marchiano [31] showed the analogy between acoustic and optical vortex beams by introducing the concept of pseudomomentum and obtained an identical result as the one derived by Allen et al. in the optical domain. In 2006, Lekner et al. [32] extended the study of Hefner & Marston [30] with the introduction of exact (nonparaxial) helicoidal solutions of the Helmholtz equation for tightly focused acoustic beams.

After these first theoretical works dealing with “singular acoustics”, several groups started to investigate the mechanical consequences of angular momentum of sound to matter by dissipative and non-dissipative processes.

1.4 Detection and measurement of the orbital angular momentum of sound

In this section, we review separately the experimental state of the art of the mechanical effects of orbital angular momentum transfer, distinguishing two cases:

when an incident field is absorbed by an object (dissipative processes) and when a object alters the incident orbital angular momentum of an incident field without absorbing it (non-dissipative processes).

1.4.1 Dissipative process

The sound-matter transfer of both linear and angular momentum by absorption is, to date, the situation that has been the most explored. The conservation of linear and angular momentum for the “sound-matter” system implies that a perfectly absorbing element intercepting a vortex beam of power P and topological charge ℓ propagating along $z > 0$ experiences a force $\vec{F} = P/c\hat{z}$ and a torque $\vec{\Gamma} = \ell P/\omega\hat{z}$, where \hat{z} is the unit vector along the propagation direction of the incident beam. One needs $\ell \neq 0$ in order to induce rotational mechanical effects. The experimental techniques enabling the detection and measurement of the angular momentum via mechanical consequences are using so far either a torsional pendulum or a freely rotating object that we call hereafter a “spinner”. These two approaches are described hereafter.

Torsional pendulum

In 2008, Volke-Sepúlveda et al. [33] and Skeldon et al. [34] presented independently the first demonstration of orbital angular momentum transfer from acoustic vortices to matter using propagating field in air via absorption, see Fig. 1.8(a) and 1.8(b). Both experimental setup consisted of a torque pendulum made of an absorptive disk hanging on top of an array of 8 individual loudspeakers distributed along a circle. Every source produces a continuous wave that is phase-delayed with respect to its neighbour in order to generate a total field that is a vortex with topological charge ℓ . At steady state, the torque generated by the absorption of the incident angular momentum is balanced by the elastic restoring torque from the twisted wire. As a results, the pendulum is rotated by angle θ_0 , proportional to the acoustic torque. Volke-Sepúlveda et al., performed the study with acoustic vortex of charge $\ell = \pm 1$ and ± 2 , while Skeldon et al. [34] worked with $\ell = \pm 1$. In 2018, Li et al. [35], extended the study of transfer of angular momentum by absorption by using a polar array of sixteen acoustic sources allowing the generation of vortices of charges from $\ell = \pm 1$ up to ± 7 , see Fig. 1.8(c).

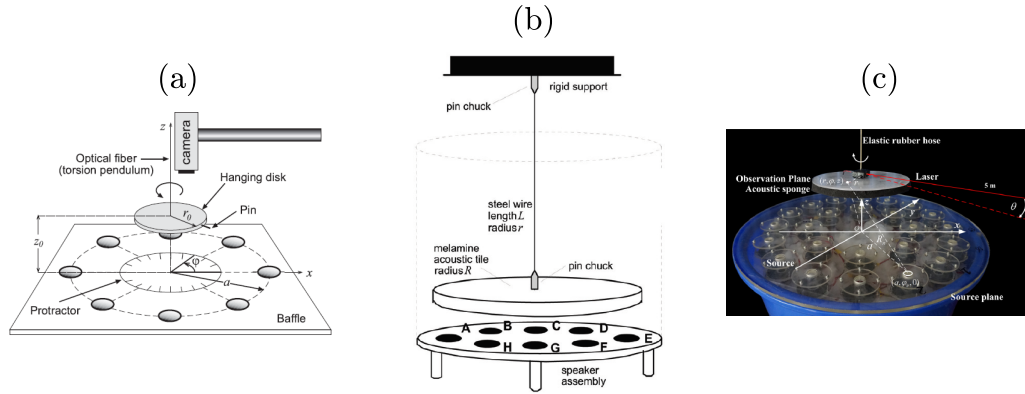


Figure 1.8: Illustration of experiments of transfer of angular momentum by a dissipative process using a torsional pendulum. Adapted from [33], [34] and [35].

Spinners

In 2012, Anhäuser et al. [36] and Demore et al. [37] reported independently the first direct measurement of acoustic orbital angular momentum via the observation of the steady rotational motion of an absorber made free to rotate on-axis. On the one hand, Anhäuser et al. used an absorbing disk placed at the interface between two fluids (aqueous glycerol solution and silicon oil) and centred with the incident beam axis owing to a needle, see Fig. 1.9(a). On the other hand, Demore et al. used an absorbing disk placed in a chamber filled with degassed water and attached to a 5 ml syringe which allows the disk to spin and move vertically, granting measurements of the transfer of both angular and linear momentum from sound to matter, see Fig. 1.9(b). In both experiments, a focused ultrasonic transducer array was used as an acoustic vortex source. At steady state, the torque generated by orbital angular momentum transfer is balanced by the viscous torque exerted by the fluid surrounding the spinner. This leads to a spinning motion at a constant angular frequency that is proportional to the acoustic torque. Noteworthy, Anhäuser et al. noticed that sound attenuation as the incident vortex beam propagates through the fluid also leads to orbital angular momentum transfer to the fluid itself. This phenomenon is the angular analogue of the usual acoustic streaming that refers to a force density directed along the beam propagation direction as sound transfers linear momentum to matter as it is attenuated during its propagation. Accordingly, the appearance of an azimuthal flow was referred as rotational acoustic streaming. As a result, a refined balance of torque has to take into account the fact that the total az-

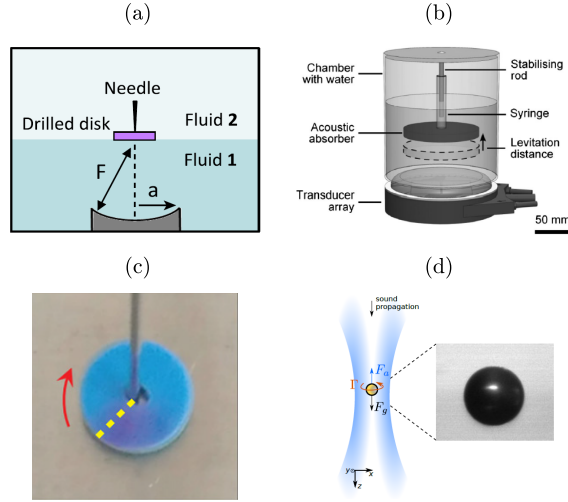


Figure 1.9: Illustration of experiments of transfer of angular momentum by a dissipative process using spinners immersed in fluids. Adapter from [36], [37], [38] and [39].

imutal velocity field possesses a rotational streaming contribution. In 2018, Li et al. [38], proposed an experiment similar to that of Anhäuser et al.. Indeed, they used a disk of 2.5 mm radius held by a needle and irradiated by and acoustic vortex, see Fig. 1.9(c), but using a different source for the acoustic vortex beam. In 2018, Baresch et al. [39] performed the trapping and spinning of immersed elastic particles by applying a negative axial gradient force using a focused acoustic vortex, see Fig. 1.9(d). Here again, the acoustic torque is calculated from its balance with the viscous torque.

1.4.2 Non-dissipative process

Beside dissipative orbital angular momentum processes, one could also formally consider its non-dissipative counterpart, in presence of a change of the orbital angular momentum state of a beam with power P , say from a topological charge ℓ_{input} to ℓ_{output} . Indeed, from angular momentum conservation, this leads to an acoustic torque $\Gamma = (\ell_{\text{input}} - \ell_{\text{output}})P/\omega$ exerted on the non-absorbing scattering object. This situation has been explored in a single work so far, a few years ago, by Wunenburger et al. [20], see Fig. 1.10. In the latter work, the idea consisted in mimicking the situation that happens in optics, where an incident Gaussian beam ($\ell_{\text{input}} = 0$) passes through a non-absorbing refractive spiral phase plate having a topological charge ℓ . In that case, the output beam is an acoustic vor-

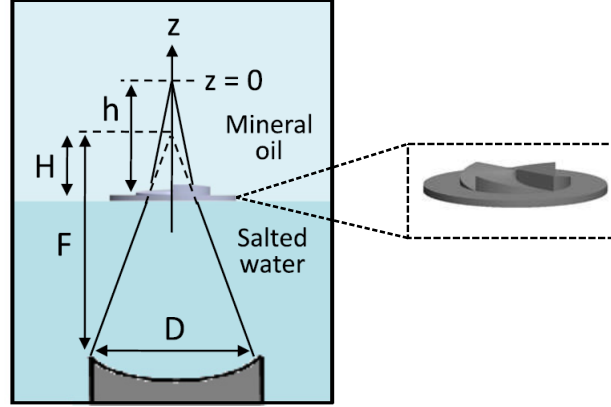


Figure 1.10: Illustration of experiment of Wunenburger et al. A 3D printed helical structure was placed on the surface on the boundary of mineral oil and salted water. The helical structures was irradiated by a focused Gaussian acoustic beam introducing a phase factor of $\exp(i\ell\varphi)$ transforming the acoustic wave into a vortex. Adapted from [20].

text beam with topological charge $\ell_{\text{output}} = \ell$, which results in a radiation torque exerted on the object that expresses as $\Gamma = \ell P/\omega$. In practice, Wunenburger et al. used a 3D printed spiral-shaped disk operating as a spiral phase plate of charge $\ell = 4$, and irradiated by a focused ultrasonic acoustic beam carrying zero orbital angular momentum ($\ell = 0$). The spiral phase plate imprints an azimuthally dependent phase factor $\exp(i\ell\varphi)$ to the transmitted field, hence generating an acoustic vortex of charge ℓ . Ensuring transfer of orbital angular momentum to the spiral phase plate makes it to spin at steady angular velocity after a transient. However, the fact that sounds propagates through an absorbing material with substantial absorption prevents obtaining in practice a pure vortex mode conversion. Indeed, the amplitude of the incident field is also modulated azimuthally, which breaks the axisymmetry required to ensure the generation of the sought after vortex beam. Nevertheless, it is important to recall that the material absorption does not prevent to conclude that the acoustic radiation torque arise from chiral sound scattering. Also, the latter work stressed that the unavoidable reflection was actually playing a role in the total angular momentum balance, however without altering the main conclusion of the work.

Sound-matter system: definition and characterization

After reviewing the state of the art of the rotational effects of acoustic orbital angular momentum at the end of the previous chapter, which emphasized the barely studied case of non-dissipative angular momentum transfer process, we present our contribution to the latter situation. The central issue is, therefore, the definition of the sound-matter interaction geometry enabling us to get rid of the sound absorption limitations pointed out in the work of Wunenburger et al. [20]. Keeping the option of using a spiral phase plate as the chiral sound-scattering element implies either to use an absorption-free material or, more drastically, to discard the propagation of sound inside the material. The former option of an absorption-free material is the ideal situation, which involves the use of a material with as small as possible propagation losses at the considered frequency. In contrast, the latter option is the most viable for experimental implementation as it requires the use of a reflective (instead of transmissive) spiral phase plate.

In this chapter, the analysis of this approach is first presented in terms of the characteristics of the wave-matter interaction, such as the properties of the used material and the sound wave. The characterization of the material system and the used acoustic source will be also presented.

2.1 Sound-matter reflective geometry

Let us consider two materials in contact, labelled as ‘0’ and ‘1’, and bounded by a planar interface. In the medium ‘0’, a plane wave propagates and impinges at normal incidence with respect to the interface between the two media. Assuming

1D propagation, an acoustic plane wave is described as

$$p(x, t) = p_0 \exp i(kx - \omega t) \quad (2.1)$$

where k is the complex wave number

$$k = \frac{\omega}{c} + i\alpha \quad (2.2)$$

where c is the speed (or phase velocity) of the carrier wave, and α is the attenuation coefficient. The reflective coefficient for the pressure field is given as

$$r = \frac{\rho_1 k_0 - \rho_0 k_1}{\rho_1 k_0 + \rho_0 k_1} \quad (2.3)$$

where ρ_0 and ρ_1 corresponds to the density of the medium ‘0’ and ‘1’ respectively. The reflectivity coefficient, expressed as $R = |r|^2$, can be reformulated as

$$R = \left| 1 - \frac{2\rho_0 k_1}{\rho_1 k_0 + \rho_0 k_1} \right|^2 \quad (2.4)$$

From Eq. (2.4) we can observe that it is possible to reach the condition of $R \sim 1$ by fulfilling the condition of $\rho_0 c_0 \ll \rho_1 c_1$, independently of the absorption coefficients. Practically, using air as the incident medium and a solid material with typical characteristics $\rho_1 \sim 1000 \text{ kg m}^{-3}$ and $c_1 \sim 1000 \text{ ms}^{-1}$, one can achieve conditions of $R = 1$ within 0.03 % whatever the value of α . Consequently, we opted for using a 3D printed reflective spiral phase plates, i.e. helical mirrors, that operate in the air and a transducer emitting ultrasonic waves at 100 kHz frequency in the air, in a continuous manner.

2.2 Helical mirror

2.2.1 Design

Our helical mirrors characterized by the integer number ℓ are designed to introduce a phase factor of $\exp(-i\ell\varphi)$ to the reflected acoustic wave. They consist in structures having circular cross-section, flat base and azimuthally dependent height $h(\phi) = \pm h_s(\phi/2\pi)$, where $h_s > 0$ is the step height, see Fig. 2.1. Considering a normally incident acoustic wave have a smooth axisymmetric phase profile

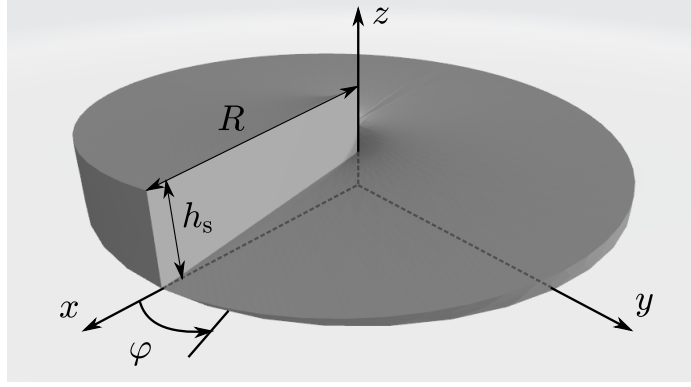


Figure 2.1: Diagram of a spiral phase plate where h_s corresponds to the height and φ is the azimuthal angle in the xy plane.

and impinging on the screw-like surface, the value of the topological charge ℓ' of the reflected vortex field just after the reflection is given by

$$\ell' = -\ell \quad \text{with} \quad \ell = \frac{2h_s}{\lambda} \quad (2.5)$$

where λ is the wavelength of the acoustic wave. For a topological charge of $\ell = 1$, we have $h_s = \lambda/2$. In the case of high-charge helical mirrors ($|\ell| > 1$), a piece-wise design is adopted. Namely, the helical mirror is split in $|\ell|$ sectors each of them having the role of imparting a phase change between 0 and 2π in a linear manner with respect to φ , see Fig. 2.2. In terms of the reflected field, there is no difference between the single-ramp and multi-ramp designs for integer charges $|\ell| > 1$ if one neglects diffraction over distances that corresponds to the step height.

As the helical mirrors will be set into rotation, the mechanical properties associated to their geometry, such as center of gravity, x_G , y_G and z_G , and the moment of inertia J around the z -axis are quantities of interest. The Cartesian coordinates of the center of gravity is calculated as

$$x_G = \frac{\rho_1 \int x dx dy dz}{M} = 0 \quad (2.6)$$

$$y_G = \frac{\rho_1 \int y dx dy dz}{M} = \begin{cases} 0 & \text{piece-wise ramp } (|\ell| > 1) \\ \frac{2R}{3\pi} & \text{one ramp} \end{cases} \quad (2.7)$$

$$z_G = \frac{\rho_1 \int z dx dy dz}{M} = \begin{cases} \frac{h_s}{3} & \text{piece-wise ramp } (|\ell| > 1) \\ \frac{h_s|\ell|}{3} & \text{one ramp} \end{cases} \quad (2.8)$$

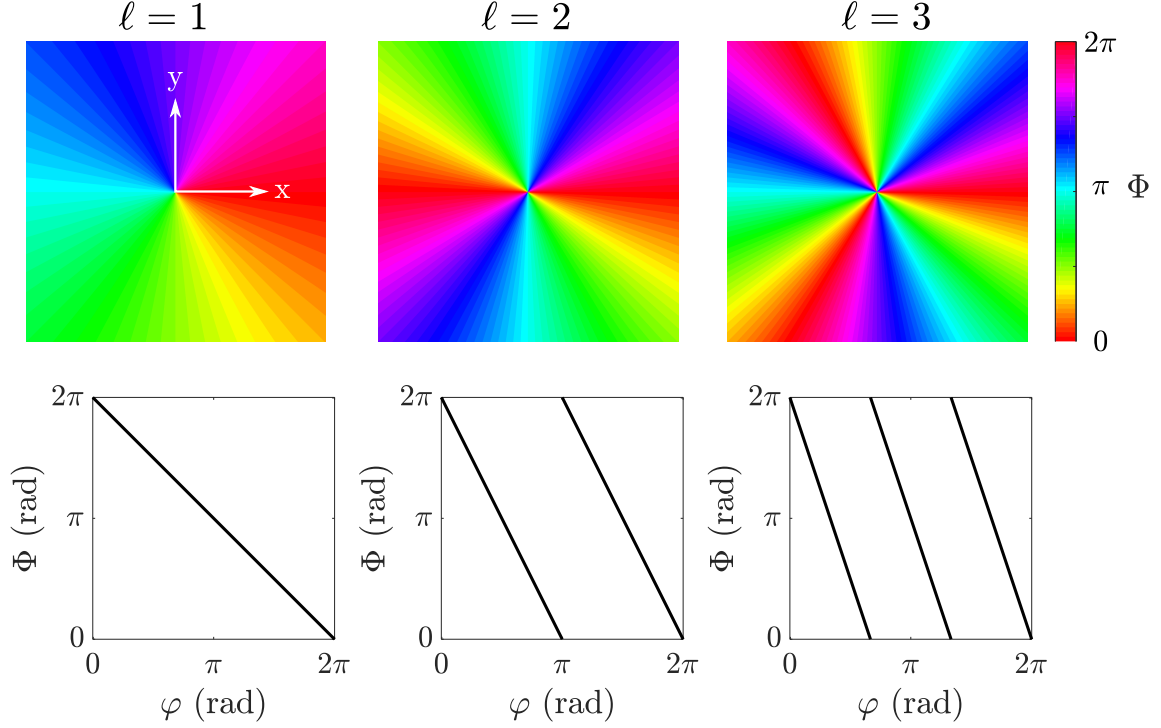


Figure 2.2: Phase distribution Φ in the transverse plane that is imparted to the reflected field and phase as a function of the azimuthal angle φ for helical mirror with integer topological charge $\ell = 1, 2$ and 3. Namely, we deal with a transmittance function $\exp(il'\varphi)$ with $\ell' = -\ell$ for a helical mirror of order ℓ .

where ρ_1 is the density of the material of the mirror, $M = \int \rho dx dy dz$ is the mass of the mirror and R is the radius of the mirror. The location of the center of mass in the transverse plane for helical mirror of charge $\ell = 1, 2, 3$ are depicted in Fig.2.3. The moment of inertia around the axis of rotation z , J , is calculated as

$$J = \int \rho r^2 r dr d\theta dz = \frac{1}{4} \rho \pi R^4 h_s \quad (2.9)$$

Noting that the volume of the helical mirror is $V = \pi R^2 \left(\frac{h_s}{2}\right)$, Eq. 2.9 is rewritten as

$$J = \frac{1}{2} M R^2 \quad (2.10)$$

where $M = \rho V$ is the mass of the helical mirror, which corresponds to the moment of inertia of a circular disk of mass M and radius R . Notice that, for a multi-ramp mirrors, the axis of rotation passes through its center of mass. Therefore, the acoustic torque is expressed as $\vec{\Gamma} = \Gamma \vec{z}$. However, for single-ramp mirrors, the fact that the center of mass is not located along the z axis implies a gravitational

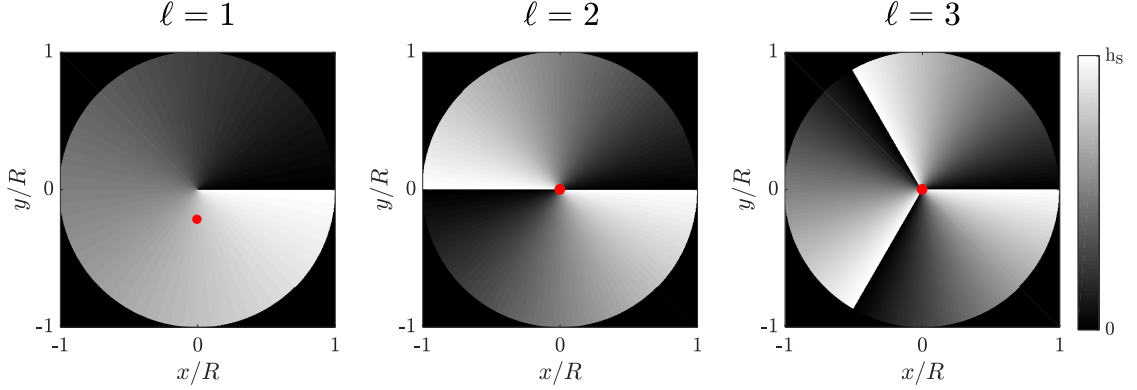


Figure 2.3: Illustration of position of center of mass $(x_{\text{CM}}/R, y_{\text{CM}}/R)$, denoted as a red dot, for ℓ -ramp helical mirrors with topological charge $\ell = 1, 2$ and 3 .

torque that tends to tilt mirror out of its initial plane in which is lying, namely, the (x, y) plane. When considering a mirror deposited on a non rigid system such as a fluid interface as we further use in this chapter, the axisymmetry is broken. In practice this may lead to mechanical drawbacks towards quantitative assessment of the acoustic torque. In order to avoid the latter issue, a two-ramp design with step height $h_s = \lambda/4$ is introduced when $|\ell| = 1$.

2.2.2 3D printing modelling: design

AutoCAD is a 3D modelling software used in the industry to design mechanical structures. For this thesis, it is used to design the helical mirrors with the desired geometrical characteristics, namely, thickness, radius and topological charge. The method to design the helical mirrors is described hereafter (see also Fig. 2.4):

- (a) The **AutoCAD** functions *line*, *arc* and *helix* are selected to draw the skeleton of one sector of the mirror. First, a segment with the length $R = 15$ mm is drawn. Second, we draw an arc line with angle $2\pi/\ell$, centered on one end of the latter segment and connected to the center with a straight line. Third, we draw a helical line running over $(1/\ell)$ of a turn with height of $h_s = 1.72$ mm, which corresponds to half of a wavelength at 100 kHz frequency, and centered on the origin of the sector. Finally, we draw a rectangle, perpendicular to the flat surface of the sector, with height h_s and length R , which is the wall of the helical mirror step for the considered sector.

- (b) Using the function *loft*, we generate the surface associated to two curves. In this case, we generate horizontal and vertical surfaces that correspond to the side walls, the planar base and the screwed roof of the helical mirror. First, the walls are drawn by selecting the helix and arc lines, as well as the top and bottom lines of the rectangle of the step. Second, the base is drawn by selecting the arc and diameter line. Third, the roof is drawn by selecting the helix and the vertical on-axis segment of step passing through the center. At this point, we have a shell of one of the sectors of the mirror.
- (c) The function *polar array* generates copies of a selected structure and distribute them equidistant to a point. In this case, the center of the array corresponds to the center of the mirror, and the number of sector corresponds to ℓ . First, we click in the function of *polar array*. Second, we select the shell corresponding to one sector of the mirror. Third, we select the center from which the polar arrangement will be generated. Fourth, we select ℓ as number of sectors generated, where here corresponds to $\ell = 2$. The number of sectors have to be input manually as 6 sectors are selected by default. Now, the shell of the helical mirror is completed. However, each sector of the shell is bound by the function *polar array*, so we need to unbind them.
- (d) The function *explode* separate in simple elements (lines and surfaces) the selected structure. First, We use this function to unbind the sectors that have been combined at the latter step of the design process. Second, we use the function *union* to make a single shell for defining the helical mirror. Third, we select the function *sculpt* to generate a solid bounded by the walls of the obtained empty shell. Now that the helical structure of the mirror is obtained, we design a pedestal on which the mirror will be placed in order to avoid the zero-thickness issue at $\varphi = 0$.
- (e) We select the function *cylinder* to make a disk-shape pedestal with height $h_p = 1$ mm and radius $R = 15$ mm.
- (e) We select the helical structure and, using the function *move*, we place it on the top of the pedestal and align their axis. We select the base and the helical mirror and use the function *union* to join them as a single structure. The design of the helical mirror is now ready.

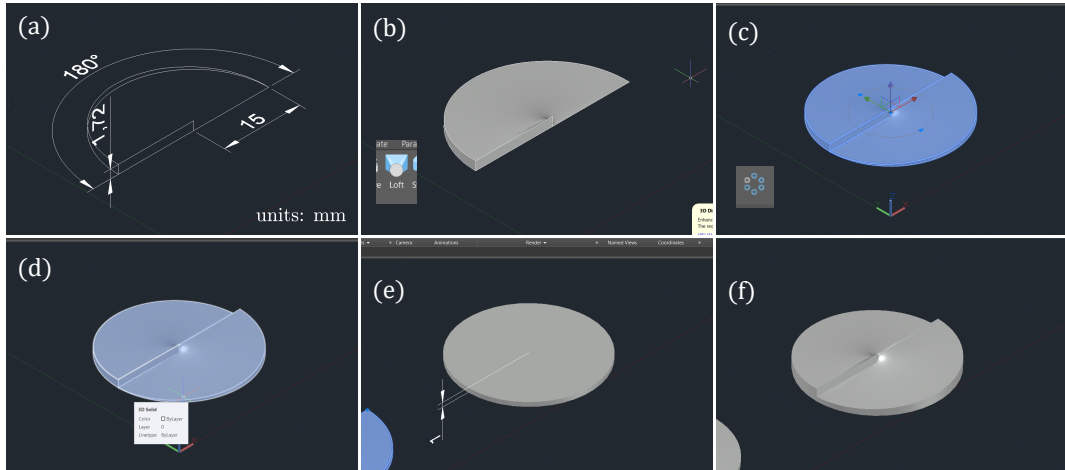


Figure 2.4: Illustration of the main steps needed to design a helical mirror with $\ell = 2$. (a) Defining the geometry of one of the sectors of the helical mirror (radius, step height and angular extent). (b) Making the shell of the sector. (c) Generating all sectors of the helical mirror and placing them. (d) Unbinding the sectors into individual parts, making a whole shell of the helical mirror and generating the desired solid volume to be printed (e) Making a pedestal on which the helical structure will sit. (f) Placing and aligning the helical structure on top of the pedestal.

Having the design of the mirror, the next step consists in exporting the AutoCAD file as an *.stl* file which is the file extension that most of the 3D printing softwares use. In our case, we use the 3D printing software **Print Studio**. The steps to prepare the 3D model are detailed hereafter (see Fig. 2.5):

- (a) The interface of **Print Studio** displays the area of the building head of the 3D printer on which the structure will be fabricated. By selecting the import option, the file is selected and placed in the printing area. One of the first thing to consider is the centering and placement of the object to be printed. It is recommended that the disk is centered with respect to the printing head.
- (b) After centering the structure, the next step is to check for any structural error concerning the design, such as disjoint planes or empty holes. Usually, when the structure is presented in red color, this indicate the presence of a discontinuity in the object. Here, such errors appear always along the on axis singularity. By selecting the option *automatic repair* the problem is fixed automatically in most cases. If the software freezes during the



Figure 2.5: Illustration of the main steps to generate the file that will be used by the printer to fabricate the structure. (a) Selecting the structure and centering it with respect to the printing head. (b) Checking and fixing possible structural errors that are presented in red color. The structure turns to blue when all the problems are fixed. (c) Select the thickness of the printing layer. Eventually, the software generates a file that includes all necessary informations to be sent to the printer.

correction process, it is necessary to check the design of the structure along the vertical central axis in order to see if the substructures are connected by a same line on the center. If still failing, one may choose to start over a new design. Once the problem is solved, the structure turns in blue color.

- (c) The final step before sending the file to the 3D printer is the definition of the thickness of the printing layers. The values of thickness are restricted by default to 50, 25 and 10 μm . In our case, we choose 10 μm corresponding to the highest quality for this particular printer (50 μm is also used once for checking the influence of the layer thickness, see later in chapter 4). Once the thickness is selected, the software generates a file that includes all necessary informations that will be sent to the printer.

2.2.3 3D Printing

The 3D printing file is further upload to the 3D printer. An **Autodesk Ember 3D Printer** is used, which is based on photopolymerization stereolithographic technique. The Autodesk PR57-K Black prototype resin is used as photosensitive resin. The steps to set the 3D printer are detailed below, see Fig. 2.6. We stress the importance of wearing nitride gloves and safety glasses during the manipulation of the resin and 3D printed structures before a curing process. The sequence of action are the following:

- (a) Shake the resin gently for 10 to 20 seconds.
- (b) Open the sliding door in front of the printer and pour the shaken resin in the resin tray until the resin upper surface lies between **Min** and **Max** marks located on one side of the tray.
- (c) With an hexagonal key, loosen the building plate before starting the printing. This is to prepare the plate for a calibration process as the printing starts.
- (d) Once the calibration process is launched, the resin tray starts to move from one side to the other to calibrate its position respect to the window through which the UV light passes. Then, the fabrication stage displaces towards the window of the resin tray.
- (e) Once the fabrication plate is positioned parallel to the window of the tray, we use two fingers of each hand to carefully press the building stage towards the tray in order to assure that both surfaces are parallel. Once this is done, we fix the building head with an hex key.
- (f) Close the sliding door of the printer and launch the printing.

The average time of printing a helical mirror is around 36 min. Once the printing is finished, remove the building plate and, with a napkin, clean the excess of resin. With a bit of isopropyl alcohol, clean the resin on top of the structure and carefully remove it with a spatula. Immerse the structure in isopropyl alcohol for about 10 min. Finally, take out the structure, dry the excess of alcohol and irradiate it with an UV light for 40 minutes to polymerise the surface of the structure as the final curing process. In our case, a source of 365 nm wavelength and 6 Watt of power was used for curing process.

Typical 3D printed helical mirrors are shown in Fig. 2.7. Fabricated high-quality structures are however fragile and must be handled with care. The set of ℓ -ramp helical mirrors with integer topological charge $-5 \leq \ell \leq 5$ and two-ramp helical mirrors with $\ell = \pm 1$ have been built in collaboration with Vilnius University (L. Jonusauskas and M. Malinauskas).

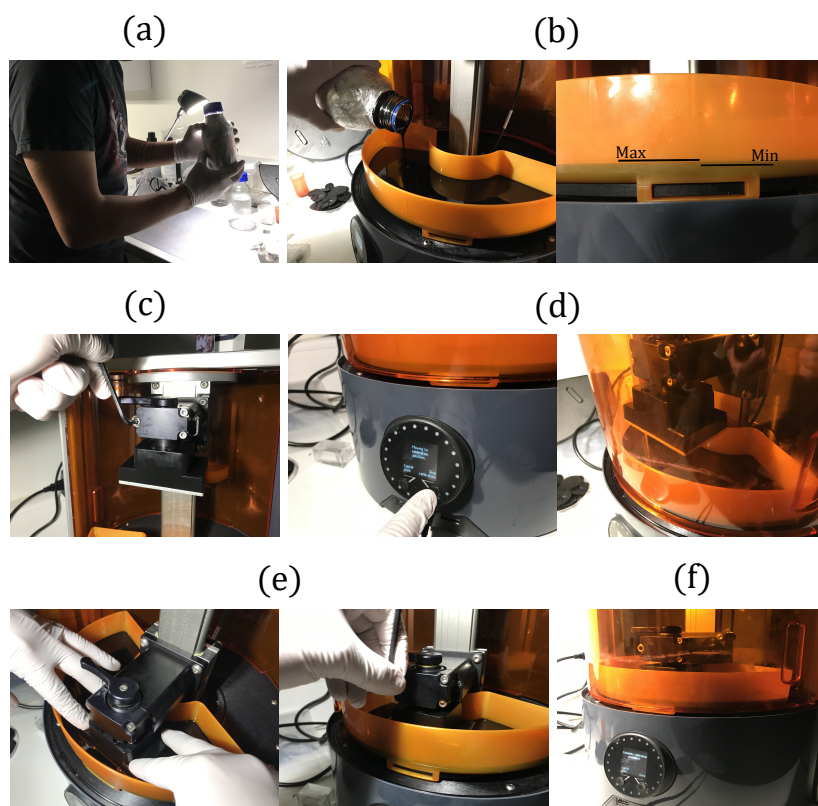


Figure 2.6: Steps of preparation for 3D printing. (a) Shaking the resin. (b) Pouring the resin in the tray. (c) Unfastening the building stage using an hex key. (d) Launching the calibration process. (e) Fixing the building stage with the hex key. (f) Launching the printing.

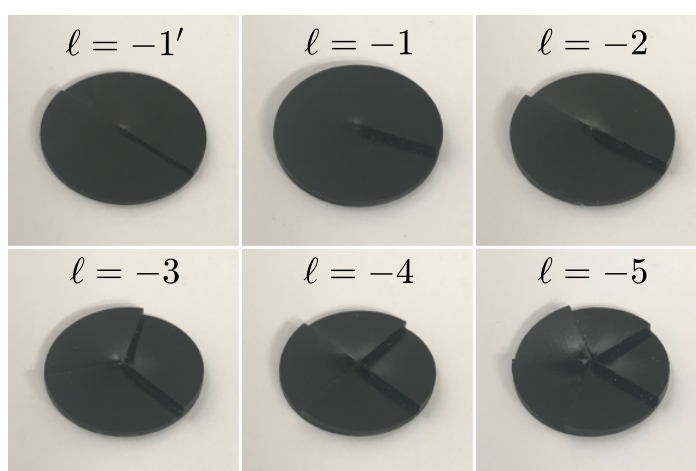


Figure 2.7: Set of 3D printed helical mirrors for $-5 \leq \ell \leq -1$ and $\ell = -1'$ (two-ramps).

2.2.4 Validation of printed helical mirrors

Once the first batch of helical mirrors has been printed, the validation of the geometrical parameters led us to a surprise, which was not immediately noticed. Indeed, the printed step height were not equal to the designed values, both for the spiral and the pedestal. In fact, at first being not aware about such a serious fabrication issue, we had no reason to be suspicious and we implemented the first experimental attempts of detection and measurement of rotational mechanical effects of acoustic vortices. It was only at the final analysis stage that we realized this problem. The price to pay for this situation was substantial delay in the project as we had to establish a protocol to achieve the desired topological charge. In Table 2.1 we present a typical example of the mismatch between the designed and measured values of the height of each step of a helical mirror with topological charge $\ell = 5$, recalling that the designed spiral step is $h_s = 1.72$ mm and the pedestal height is $h_p = 1$ mm. The mismatch corresponds to a relative discrepancy of 67% for h_s and 54% for h_p . We did not find an explanation since we carefully followed the protocols of designing and printing as indicated in the user manual of the software and printer. Moreover, the company **Autodesk** abruptly announced the end of production of their recently released 3D printer Ember, without providing an explanation to the consumers. In addition, we were not able to obtain information concerning this issue or even address the problem directly to the company. Since then, we had to work to find a solution by ourselves with the purchased system in order to achieve our goal anyway. To get the correct value of step height, we opted for a trial and error process. The idea is to fabricate a set of structures with various designed values h_d for the spiral step and to compared them with step height h_s of the printed elements. We found that for a helical mirror with 30 mm diameter and $\ell = 5$, the optimal height to design for a target value $h_s = 1.72$ mm is $h_d = 2.21$ mm. Using this value as a

sector #	1	2	3	4	5	$\langle \cdot \rangle \pm \text{std}$
h (mm)	2.68	2.71	2.81	2.70	2.65	2.71 ± 0.06
h_p (mm)	1.56	1.57	1.67	1.56	1.37	1.546 ± 0.10
h_s (mm)	1.12	1.14	1.14	1.14	1.28	1.164 ± 0.06

Table 2.1: Measurements of the total height (h), height of the pedestal (h_p) and height of the step (h_s).

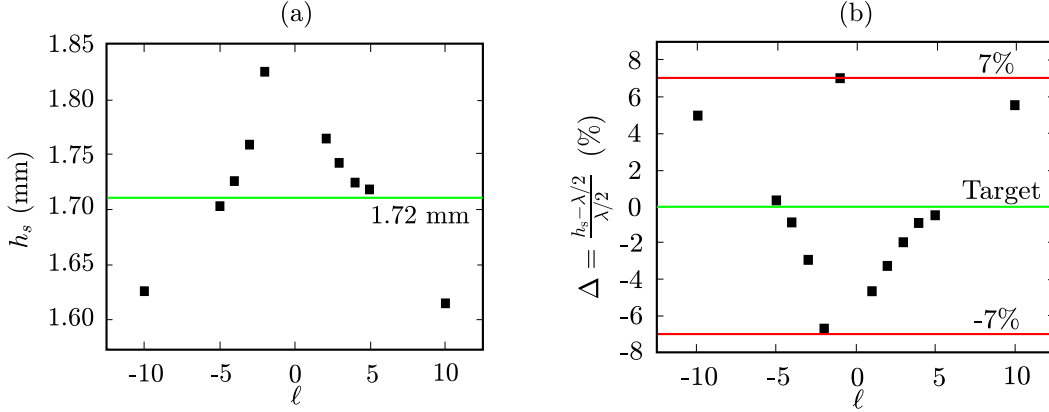


Figure 2.8: Measured step height for helical mirrors with printing design value $h_d = 2.21$ mm. (a) Average step height over the ℓ sectors for topological charges $-10 \leq \ell \leq 10$. (b) Percentage of the relative deviation with respect to the ideal step height value $h_s = 1.72$ mm.

reference, all the other structures were printed without a specific trial and error process. In Fig. 2.8 we present the obtained values of h_s for different values of ℓ , see Fig. 2.8 (a), and the relative deviation $\Delta = (h_s - \lambda/2)/(\lambda/2)$ with respect to the desired value of $h_s = \lambda/2$, see Fig. 2.8(b). From these results, we obtain a deviation less than 7% in the range $-10 \leq \ell \leq +10$ which we found satisfying enough to pursue our studies.

In addition, we also checked the quality of the central part of the helical mirror. Indeed, a morphological singularity is introduced by design in the center. The file used by the 3D printer corresponds to a tessellation of the designed shell. When the printing software tries to define the singularity, errors of continuity unavoidably emerge. The software bypass this by smoothing the core, hence deforming the surface. In order to quantify the deformation of the core, a helical mirror with topological charge $\ell = 2$ and radius $R = 12$ mm is cut in half through its center and parallel to the two steps, see Fig. 2.9(a). The radial profile of the step height is extracted numerically from a picture via contour analysis, see Fig. 2.9(b). The obtained profile is shown in Fig. 2.9(c), using as a reference the value of $h_s(r = 0)$ as shown in Fig. 2.9(b), where r is the distance from the center of the mirror. The profile is empirically fitted with the ansatz $h_s(r) = h_0(1 - \exp(-r/r_0))$. In this example we find $h_0 = 1.79$ mm and $r_0 = 0.10$ mm. We estimate from such a topographic inspection of the helical mirror that the non-uniform region has a maximal radius $r_0 \sim 1$ mm. Noting that the extreme situation that consists to discard the mechanical effect of sound on a disk of radius r_0 , typically implies

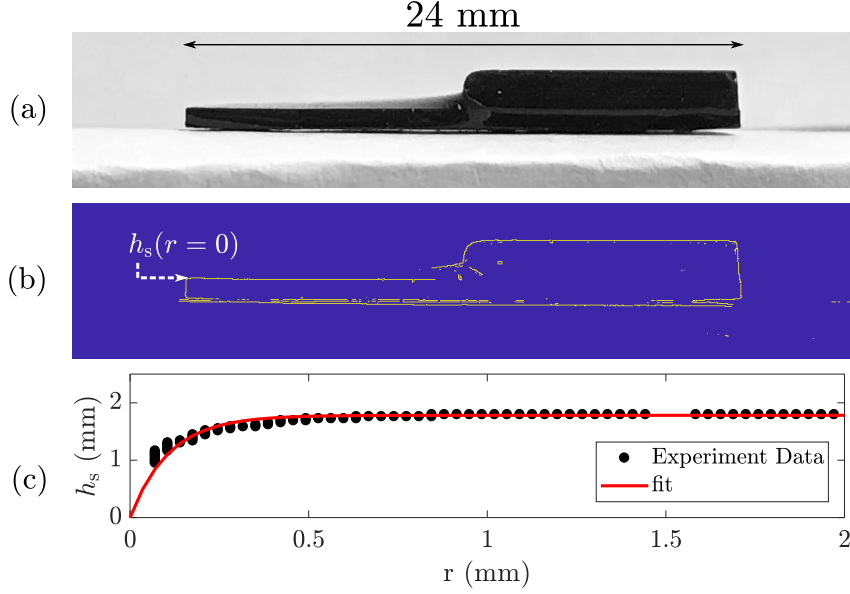


Figure 2.9: (a) Cross-section of a helical mirror with topological charge $\ell = 2$. (b) Contour of the cross-section shown in (a). (c) Height radial profile, taking the height of the base as the reference value $h_s(r = 0)$.

uncontrolled sound matter interaction over a fraction of less than 1% of the total area of the helical mirror. Therefore, such imperfections can be considered acceptable in practice.

2.3 Acoustic source: modelling

As it will be discussed later in this section, we use a planar disk-shaped piezoelectric transducer operating in the air at 100 kHz frequency. Here, we start by the ideal description of our acoustic source field and the presentation of the used simulation tools whose implementation is validated by confronting obtained values with known analytical solutions.

2.3.1 Analytical results

The pressure field of the acoustic transducer is modelled as a circular planar disk of radius a mounted in a baffle of infinite spatial extent as we are considering that all the pressure field propagates in the region $z > 0$ without back reflection. In addition, we discard any effects of diffraction due to the borders of the

transducer, see Fig. 2.10. For a piston moving sinusoidally at uniform velocity $v(t) = v_0 \sin(\omega t)$, with v_0 a constant, we have

$$p(r, \theta) = \frac{-i\omega\rho_0 v_0}{2\pi} \int_S \frac{\exp(ikR)}{R} dS \quad (2.11)$$

where S is the surface of the piston, ω is the frequency of the generated sound wave, ρ_0 is the mean mass density of the medium in which sound propagates (air in our case), $k = \omega/c_0$ is the wave number, c_0 is the speed of sound in the air, and $R = |\mathbf{r} - \mathbf{r}'|$. Also here, we neglect propagation losses. Integrating Eq. (2.11) for any point is complicated and in most cases it can only be solved by numerical approximations, see for instance [40]. However, closed-form solutions can be found in particular cases. For instance:

(a) Far Field: $r \gg a$

$$p_{\text{far}} = p(r, \theta) = A\pi a^2 \left[\frac{2J_1(ka \sin \theta)}{ka \sin \theta} \right] \frac{e^{ikr}}{r} \quad (2.12)$$

where $A = -i\omega\rho_0 v_0/2\pi = -ip_0/\lambda$, $p_0 = \rho_0 c v_0$ is a pressure amplitude, λ is the wavelength, θ is the angle between the transducer axis the position vector at the observation point, see Fig. 2.10, and J_1 is the first-order Bessel function of first kind.

(b) Axial field: $\theta = 0$

$$p_{\text{axial}} = p(r = z, \theta = 0) = A \frac{4\pi}{k} \sin \left(k \left[\sqrt{z^2 + a^2} - z \right] / 2 \right) \times e^{ik \left[\sqrt{z^2 + a^2} + z \right] / 2} \quad (2.13)$$

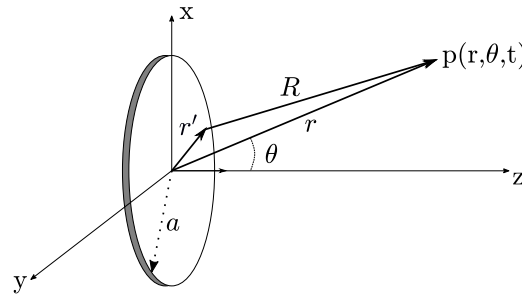


Figure 2.10: Diagram of acoustic transducer modelled as a planar disk of radius a mounted in a baffle of infinite spatial extent.

Note that, for $z \gg a$, Eq. (2.13) corresponds to Eq. (2.12) evaluated at $\theta = 0$. Also, the magnitude expression given by Eq. (2.12) allows us to separate the radial and angular component, r and θ respectively. Namely,

$$\begin{aligned} |p_{\text{far}}(r, \theta)| &= \left| \frac{A\pi a^2}{r} \right| \left| \frac{2J_1(ka \sin \theta)}{ka \sin \theta} \right| \\ &= |p_{\text{far}}(r)| H(\theta) \end{aligned} \quad (2.14)$$

In the literature, $|p_{\text{far}}(r)|$ is known as the *axial pressure* and $H(\theta)$ is known as the *directional factor*. After defining the pressure field in the axial and far field, we define the acoustic intensity I as $|p|^2$, which corresponds to the energy per unit of area of the propagating wave. From here, we can define the intensity associated to the far field and the axial field pressures, $I_{\text{far}} = |p_{\text{far}}|^2$ and $I_{\text{axial}} = |p_{\text{axial}}|^2$, respectively. Comparing Eq. (2.12) at $\theta = 0$ with Eq. (2.13), we define the region in which the far field approximation is valid. In Fig. 2.11(a) we present the intensity of the pressure field in decibel scale, $I_{\text{dB}} = 10 \log(I(z)/I_{\text{axial}}(0))$ of the axial solution I_{axial} and the far field solution I_{far} and the error between the two values $\epsilon = \log(I_{\text{far}}/I_{\text{axial}})$. Fig 2.11(a) allows introducing a characteristic propagation distance $z_{\text{R}} = ka^2/2$, usually called Rayleigh length distance. For propagation distances longer than z_{R} , $p_{\text{axial}}(r > z_{\text{R}})$ typically presents an asymptotic behaviour that is close to the far field expression. In Fig. 2.11(b) we present the directional factor $H(\theta)$ for a circular planar transducer with a relative size of $ka = 10$, which roughly corresponds to the circular transducer used in this thesis.

2.3.2 Numerics: beam propagation method

As discussed above, the description of the acoustic source by an analytical function of the pressure field is restricted to limit cases. However, if one is interested in the near field, numerical simulations are necessary. One of the available methods is the *beam propagation method* (BPM), which is the one we used in this thesis. Since BPM method is a generic approach to all kinds of waves, let us define the wave function $\Psi(x, y, z)e^{-i\omega t}$ of a wave propagating along the z axis with a wave number $k = \omega/c_0$. From the knowledge of the field at $z = 0$, $\Psi(x, y, 0)$, the field can be calculated at any position z according to the following steps:

- (a) Obtain the plane wave spectrum of the field at $z = 0$ via 2D Fourier transform.

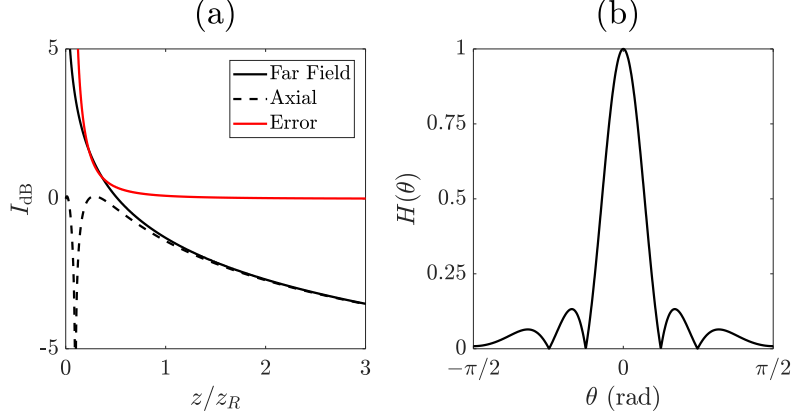


Figure 2.11: (a) Comparison of the intensity of the pressure field for exact axial solution I_{axial} and far field solution I_{far} , and the error between the two intensities (see text for details) as a function of the distance from the transducer scaled with the Rayleigh length $z_R = ka^2/2$. (b) Directional factor $H(\theta)$ for a transducer with reduced radius $ka = 10$.

- (b) Apply the propagator factor $\exp(ik_z z)$ to all the constitutive plane waves, where $k_z = (k^2 - k_x^2 - k_y^2)^{1/2}$.
- (c) Return to the real space by applying the inverse 2D Fourier transform.

This approach is summarized in Fig. 2.12. In order to benchmark our homemade BPM calculations, we propose to evaluate the normalized intensity of the field emitted by a uniform source with a circular aperture having a normalized radius $ka = 10$ after propagation distances $z = 0.5z_R$, z_R and $2z_R$ and compare it with the intensity expected from the analytical solution, see Fig. 2.13. A measurement of the absolute error between the two values is obtained by calculating the difference, $\delta(I(r)/I(0)) = |I_{\text{BPM}}(r)/I_{\text{BPM}}(0) - I_{\text{analytics}}(r)/I_{\text{analytics}}(0)|$. Absolute error is typically < 0.01 for $z > z_R$.

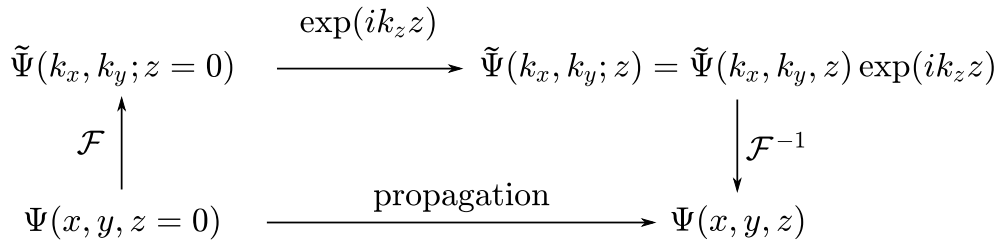


Figure 2.12: Diagram of BPM algorithm, where \mathcal{F} (\mathcal{F}^{-1}) refers to the 2D (inverse) Fourier Transform in the transverse plane.

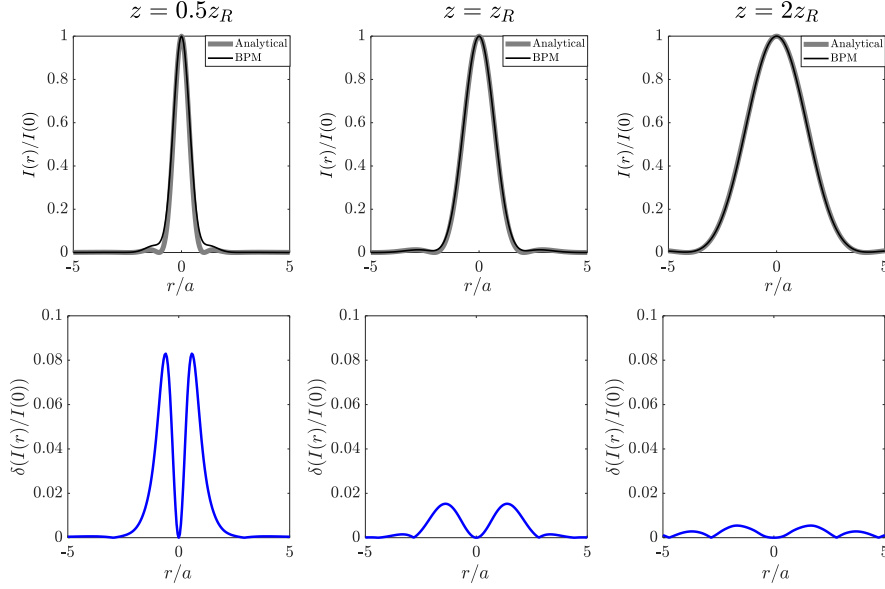


Figure 2.13: Top row: Normalized analytical and numerically calculated intensity profiles of the field generated by a uniform disk-shape source field placed at $z = 0$ at propagation distances $z = 0.5z_R$, z_R and $2z_R$. Bottom row: absolute error between the BPM calculations and the analytical solution.

2.3.3 Gaussian-field approximation

Besides the possible use of analytical expressions in specific cases or the general use of BPM, other kind of approximate analytical description of the acoustic field is valuable. An example is the Gaussian description of the field at a distance $z > z_R$. Calculations of intensity profile and effective fitted Gaussian profile for circular aperture are depicted in Fig. 2.14. It is seen that the intensity field at a distance of $z > z_R$, if simulated with a Gaussian profile, would present an error of less than 0.01 with respect to the original profile. The simulation section is ending here with providing, in Fig. 2.15(a) the axisymmetric intensity field of the acoustic transducer that we used in experiments obtained by BPM. Each plane of propagation is normalized by its own maximum for better readability. In order to simplify further the description of an acoustic field, we compare the latter situation with the situation without hole, namely, a plane transducer. The results are shown in Fig. 2.15(b). The small level of discrepancy between the two cases lead us to consider for further analysis that our transducer is a plane one, especially noting that our experimental investigation towards the measurement of the acoustic torque are made at a typical distance larger than $z = 20$ mm. In

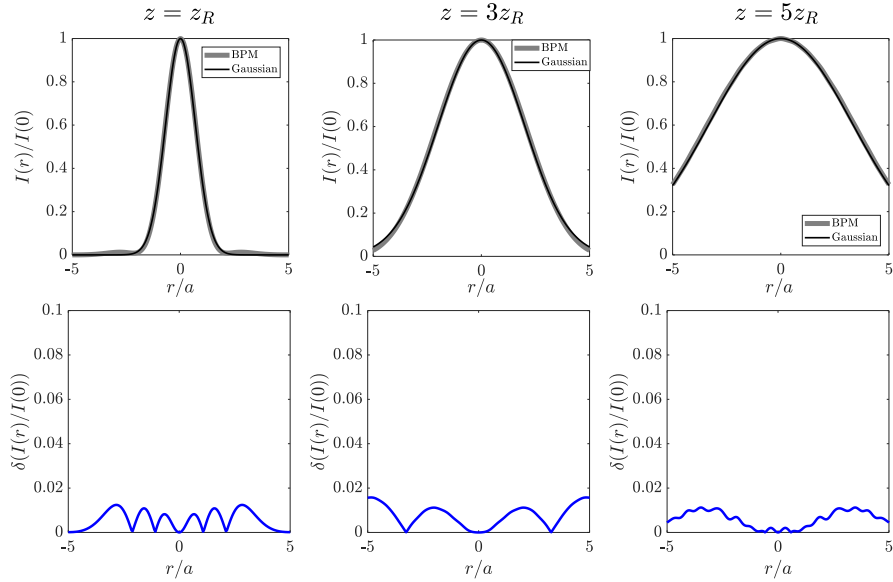


Figure 2.14: Top row: Normalized intensity profile calculated with BPM of the field emitted by a circular aperture placed at $z = 0$ mm at propagation distances $z = z_R$, $3z_R$ and $5z_R$. Thin dark curves refers to its Gaussian fit. Bottom row: Absolute error between BPM calculations and Gaussian fit.

particular, the white dash curve in Fig. 2.15(b) corresponds to the distance from the propagation axis z at which the normalized intensity is equal to e^{-2} and the black solid line originating from the center of the transducer corresponds to the linear fit of the asymptotic behaviour of the white curve. From the black line, the Gaussian divergence angle is determined as $\theta_0 = 0.274$ rad (15.7°).

2.4 Acoustic source: experiments

As an acoustic source, we used the acoustic transducer from **tec5** that is a part of their **AG Ultrasonic Levitator**, see Fig. 2.16. It consists of a piezoelectric transducer of 10 mm diameter with a hole of 1 mm passing through its center, and driven by a power source at a constant frequency of 100 kHz. The power source supply of the transducer is equipped with an analogue power controller and a panel indicating the acoustic power in arbitrary units. The power source works in the range of $3.5 < \tilde{P}_0 < 6.5$ where \tilde{P}_0 stands for the total emitted acoustic power in arbitrary units, where the number refers to the value displayed by the power supply. It can be driven externally via a function generator. Using a

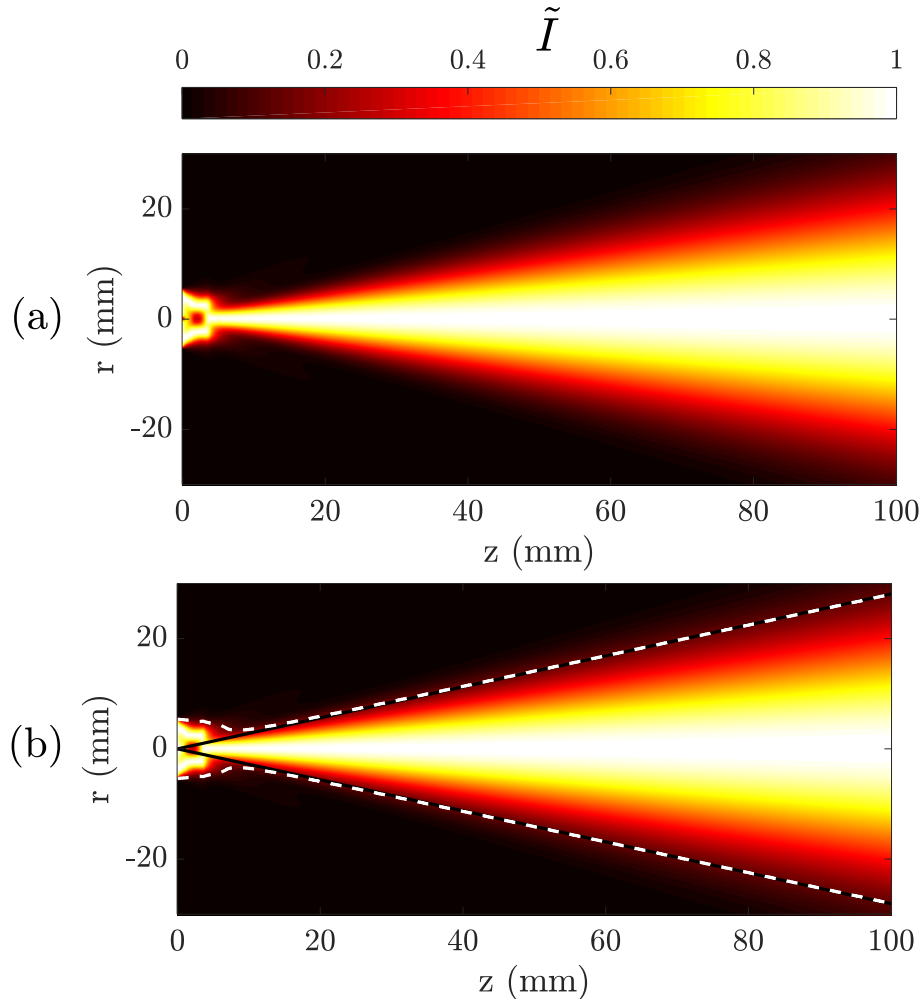


Figure 2.15: Meridional normalized intensity profile calculated by BPM for a 10 mm diameter circular transducer. The normalized intensity \tilde{I} is defined as $\tilde{I}(x, y) = I(x, y)/\max[I(x, y)]$. (a) Transducer with a 1 mm diameter hole in its center. (b) Plane transducer.

piezoelectric sensor in order to convert the periodic variations of pressure of the acoustic wave source into a periodic voltage, see Fig. 2.17(a), we can monitor the pressure field. The latter is actually measured to have a 100 kHz frequency with a precision less than 1%, as stated in the specifications of the manufacturer.

Once the acoustic transducer is on, we found that a warming-up time is necessary as the power source presented a decrease of the acoustic power until it reaches a steady value after a transient. In order to estimate quantitatively the latter transient time, we monitor the pressure field as a function of the time using the 10 mm diameter piezoelectric sensor placed at a couple of centimetre distance from

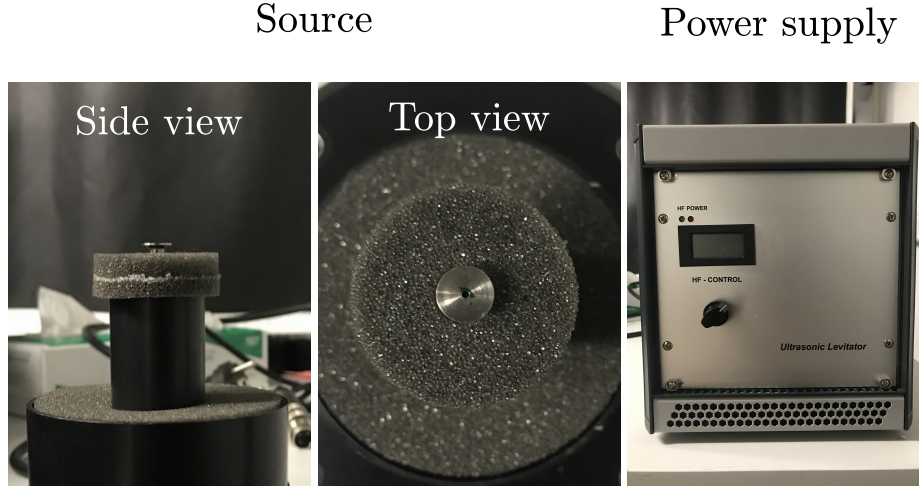


Figure 2.16: Illustration of the acoustic transducer (side and top view) and its power supply.

the transducer. As the transducer and the piezoelectric sensor form a cavity, we adjust the position of the sensor to a high-pressure region allowing easier detection of the signal. A data acquisition system from National Instruments (NI-DAQ) is connected to the piezoelectric sensor, reading the variations of voltage that corresponds to local changes of pressure of the field. The acoustic power P is proportional to $\langle p^2 \rangle$ and the pressure p is proportional to the voltage V . The information concerning the stabilization of the power of the acoustic source is extracted from $\langle V^2 \rangle$. The experimental values are fitted using the following ansatz

$$V(t) = V_0 - V_1 (1 - \exp(-t/\tau)) \quad (2.15)$$

where V_0 , V_1 and τ are the adjustable parameters. The results of the fit is shown in Fig. 2.17(b), which gives a relaxation time $\tau = 10.5$ min. In practice we wait 40 min before starting any measurement as a protocol ensuring a proper stabilization of the acoustic source.

2.4.1 Power characterization

Another characteristic of interest is the acoustic power P_0 delivered by the transducer. Its measurement is made by implementing radiation pressure experiments with the aid of an electronic scale whose surface can be considered as an acoustic perfect mirror. As sound reflects on it, a transfer of linear momentum between the acoustic wave and the scale, a net force is exerted on the scale, which is

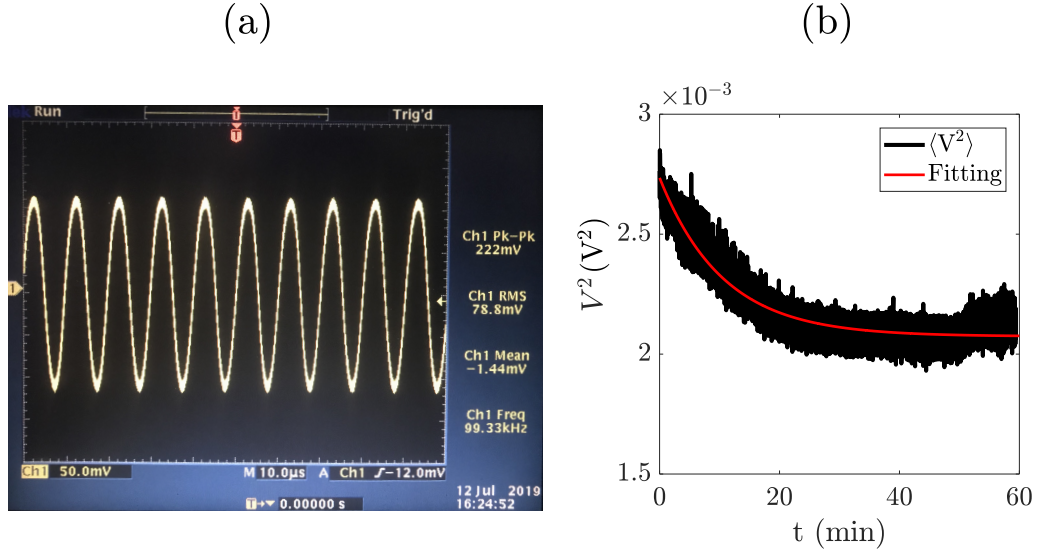


Figure 2.17: (a) Screen of the oscilloscope during a measurement of the pressure field using a piezoelectric sensor. The carrier frequency of the acoustic signal is measured to be 100 kHz with a precision $< 1\%$. (b) Transient dynamics of the quantity associated with the acoustic power detected by a piezoelectric sensor. Exponential relaxation adjustment (red curve) allows determining the characteristic transient time needed to achieve steady power emission.

read as a value of mass, m . In a first approximation, neglecting any cavity effect between the scale and the transducer, the acoustic power is related to the mass according to the expression:

$$P_0 = \frac{mgc_0}{2 \cos \theta} \quad (2.16)$$

where g is the gravity acceleration, c_0 is the speed of sound in the air and θ is the angle of incidence of the wave respect to the normal to the plane of the scale. Two approaches are considered: (a) oblique ($\theta = 45^\circ$) and (b) normal incidence ($\theta = 0^\circ$) for the acoustic source. Also, with the aim at being in conditions as close as possible to the experimental situations (see chapter 3), 3D printed disk 30 mm diameter is placed on the scale as depicted in Fig. 2.18.

Oblique incidence

The acoustic source is oriented at $\theta = 45^\circ$ incident angle, see Fig. 2.18(a). To ensure that all the acoustic wave is inscribed in the disk, a distance $d = 25$ mm from the transducer is chosen. A simulation of the projected intensity distribution on the disk is depicted in Fig. 2.19. This leads us to validate that almost all the acoustic power is collected by the flat mirror. An **ae ADAM PW 254** analytical

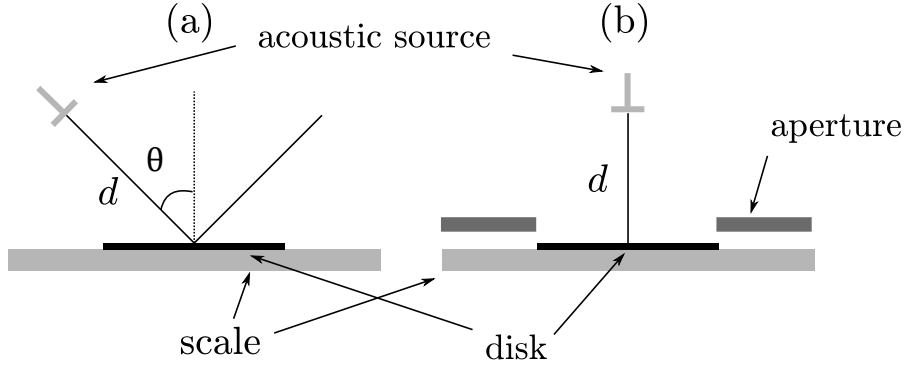


Figure 2.18: Sketch of the radiation pressure experiments for total acoustic power measurement at (a) oblique and (b) normal incidence.

balance with a sensibility of 0.1 mg is used for the mass measurements. The mass measurements are performed for all the values of power displayed in the power supply panel of the acoustic transducer. Namely, for \tilde{P}_0 ranging from 3.5 to 6.5 by 0.1 step. The results are shown in Fig. 2.20(a), for which 10 measurements are made at each power value. In particular, we show in Fig. 2.20(b) a set of 20 independent measurement at $\tilde{P}_0 = 5$, which is the value used in the experiments discussed in chapters 3 and 4. In the latter case, we find $P_0 = 25.0 \pm 0.7$ mW.

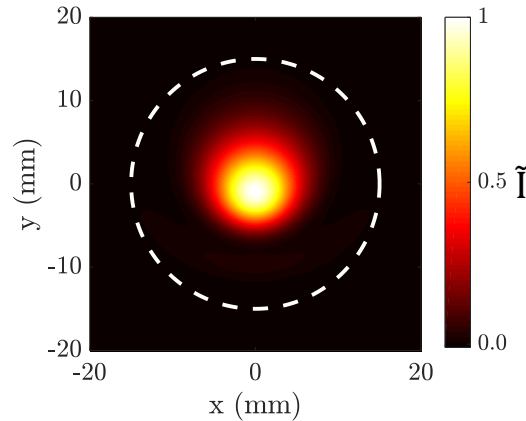


Figure 2.19: Simulation of the acoustic intensity profile in the plane of the scale for the experiment shown in Fig. 2.18(a) with $\theta = 45^\circ$. The white dashed circle corresponds to the rim of the disk shaped flat mirror having a 30 mm diameter.

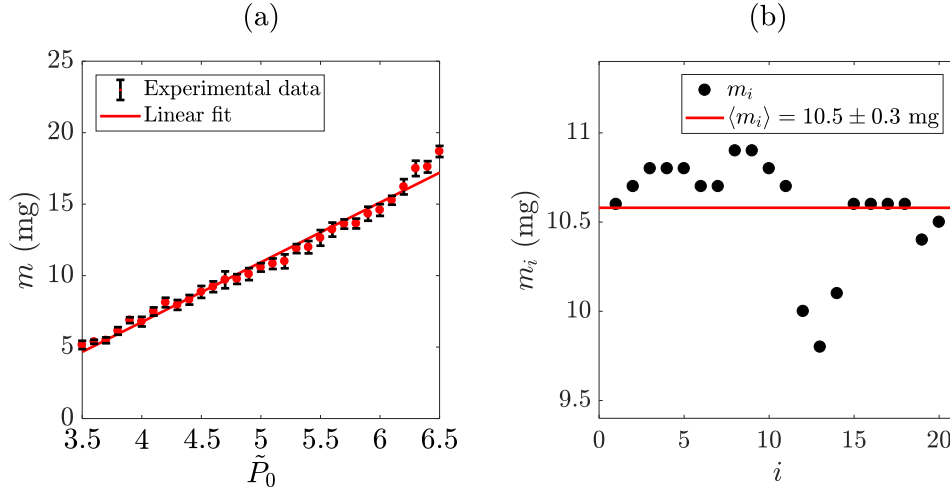


Figure 2.20: (a) Mass as a function of power \tilde{P}_0 . (b) Details of set of 20 independent measurements at $\tilde{P}_0 = 5$, which gives $P_0 = 25.0 \pm 0.7$ mW.

Normal incidence

Here, we perform the same experiment that above, but using $\theta = 0^\circ$, see Fig. 2.18(b). Importantly, now we have to pay attention to the fact that a cavity forms between the transducer and the flat mirror. Towards a quantitative description,

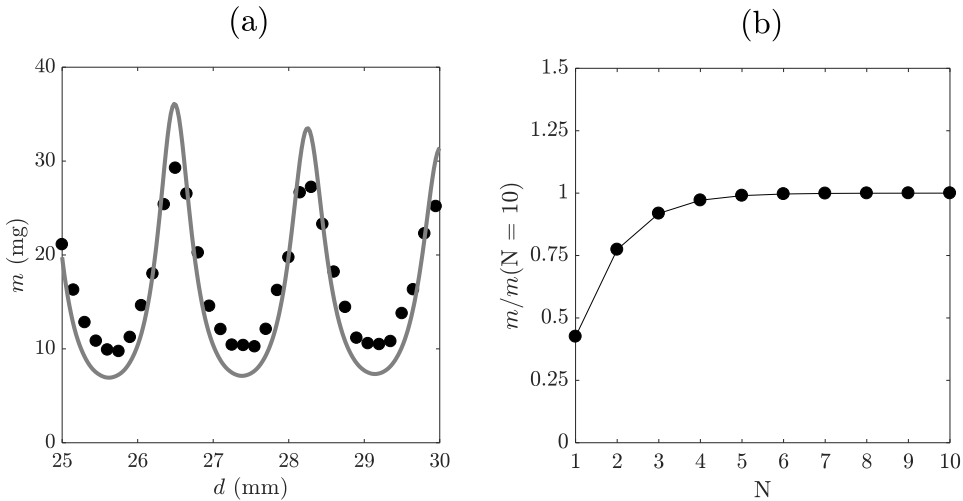


Figure 2.21: (a) Mass as a function of the transducer-mirror distance at normal incidence. Markers refer to measurements and solid curve refers to best adjustment using P_0 and a distance offset as adjustable parameters. (b) Illustration of the calculated convergence regarding the applied force (here we plot the corresponding effective mass) as a function of the number of round-trips N between the transducer and the mirror, at $d = 25$ mm.

we ensure that there is only interaction between the acoustic source and the mirror by placing an aperture of diameter 30 mm on top of the disk, without touching neither the scale nor the flat mirror deposited on it. The results of the mass measurements are shown in Fig. 2.21 for $\tilde{P}_0 = 5$. The observed oscillations as a function of the distance d between the transducer and the mirror reveal clearly a cavity effect. Extracting the total acoustic power P_0 from these oscillations thus requires careful analysis.

This is done using BPM simulation, considering multiple reflections between the transducer (considered as a mirror) and the mirror. We find that, considering a few “impacts” of the wave on the mirror is enough to obtain a converged value of the acoustic force exerted on the disk mirror. The simulation results are shown in Fig. 2.21(b) for a given separation distance $d = 25$ mm, where the mass that would correspond to the applied force is plotted as a function of the number of round-trip N inside the cavity. This information is then used to fit the experimental data of mass as a function of d , imposing $N = 7$ in the simulations. Best fit is obtained for $P_0 = 27.9$ mW.

Orbital acoustomechanics: a spinning experiment

In the previous chapter, the two key elements enabling the implementation of experiments dealing with controlled orbital angular momentum transfer have been presented, namely, the acoustic source field and the helical mirrors. Let us recall that the specificity of the present work is to address the case of non-dissipative orbital angular momentum transfer between sound and matter. In this chapter, the experimental developments in the framework of freely rotating helical mirrors are reported. Spinning dynamics experiments is thus the core of this chapter, starting with qualitative observation before going progressively to the quantitative assessment of the acoustic radiation torque exerted by sound on the irradiated helical mirrors.

3.1 Preliminary experiments

3.1.1 Preparing the experimental set-up

For the freely rotating spinning experiment, we use a pool of 37 mm of diameter and 25 mm of depth, with a transparent plexiglass slab at the bottom working as an optical window. The helical mirrors are marked with a white dye working as a tracer. The pool is filled with pure water and the mirror lies at the air-water interface owing to surface tension. The protocol used to place the helical mirror at the interface is explained hereafter and summarized in Fig. 3.1:

- (a) The pool is filled up to the top using a pipette until a convex air-water interface is obtained.
- (b) The helical mirror is placed next to the pool and gently slid from the side of the pool while water is removed until the mirror get inside the pool. This

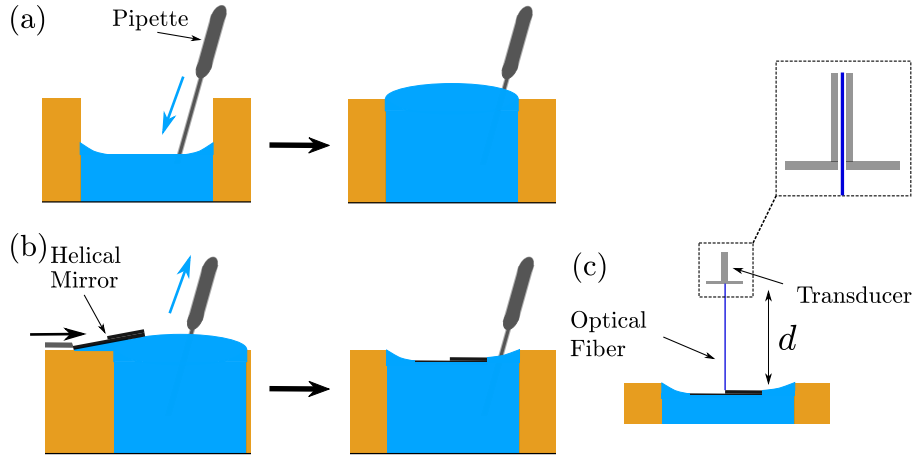


Figure 3.1: Experimental protocol for mirror placing in the pool. (a) Filling the pool with water (b) Placing the mirror at air-water interface and inducing the self-centering of the mirror. (c) Aligning the mirror with respect to the transducer.

process has to be done slowly as the water can wet the upper surface of the mirror, hence making it to sink. The extraction of water changes the curvature of the interface, from convex to concave. This eventually leads to a situation where the mirror is self-centered by capillary effects. Here, we take care to keep the air-pool-water contact line attached to the rim of the pool in order to ensure axisymmetry of the system. If the contact line detaches, the process is restarted from step (a).

- (c) The acoustic transducer is placed 0.5 cm above the centered mirror and aligned on-axis with the mirror, owing to an optical fiber passing through the central hole of the transducer. Then, the transducer is approached to the upper surface of the mirror until the transducer and the mirror are in contact. This defines the origin of the transducer-mirror distance d . Finally, the transducer is moved up to set the distance of study.

3.1.2 Qualitative observation of spinners

A first set of experiments are run to define the experimental procedures that will eventually lead to a quantitative assessment. A diagram (not on scale) of the experimental setup is shown in Fig. 3.2(a). Ten helical mirrors, left- and right-handed, with 10 mm diameter are used, see Fig. 3.2(b). The acoustic transducer

is placed at a distance from the mirror of $d = 35$ mm and we set the acoustic power to $\tilde{P}_0 = 3.5$. The spinning experiments are performed as follow (see Fig. 3.2(c) and 3.2(d)):

- The mirrors is first irradiated by the acoustic wave during 30 s, which is enough to ensure that a steady rotation is achieved.
- The dynamic of the mirror is then recorded for a time interval corresponding to 10 full turns, see Fig. 3.2(c) for a sequence of snapshots illustrating one full turn.
- From the recorded video file, we calculate the correlation coefficients between the first frame and all the subsequent ones in order to retrieve a quantitative dynamic trace of the rotational motion. The rotation frequency is then extracted from the Fourier transform of the dynamics of the correlation coefficient, see Fig. 3.2(d) for a typical data set.

The angular frequency as a function of the topological charge is displayed in Fig. 3.4(a), which does not exhibit the a priori expected linear behaviour. A possible reason is that, recalling that the mirror and the transducer form a cavity (see chapter 2), there could be a position-dependent effective power for distinct experiments. Indeed, we have typically a precision of 0.5 mm in the distance between the transducer and the mirror. Therefore, it is likely that the experiments are not performed at a constant distance d . To solve this situation, the spinning frequencies are measured in the range $25 \text{ mm} < d < 27 \text{ mm}$ and fitted with the function $f(d) = A + B \cos(kd + C)$, where $(A, 0 < B < 1, C)$ are adjustable parameters. The latter expression corresponds to the most simple version of the effect of multiple reflections between the mirror and the transducer, namely assuming interferences between two waves. In practice, this simple picture works well enough to describe the behaviour of the frequency in the present range of study as shown in Fig. 3.3. Then we update Fig. 3.4(a) using the maximal frequency at the closes distance to $d = 26$ mm. The results are shown in Fig. 3.4(b). The non-linear trend is kept. Still, we note a reasonable symmetry of the behaviour for $\ell > 0$ and $\ell < 0$, as expected from reverse acoustic radiation torque with changing the sign of the topological charge of the helical mirror. Therefore, in the following experiments we focus on $\ell > 0$ only. Moreover, the experiments show a good reproducibility and a low systematic error. Thus, even though the

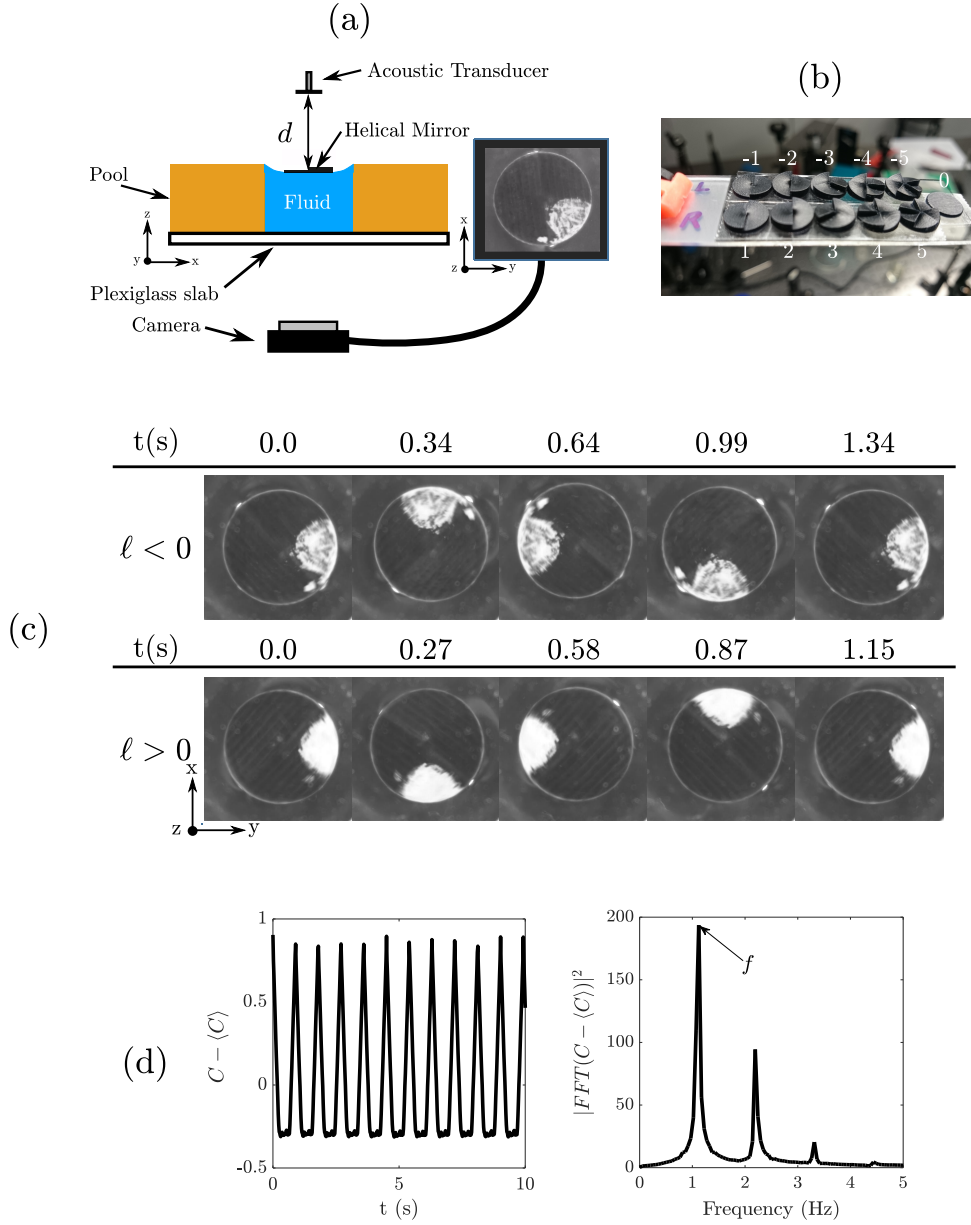


Figure 3.2: (a) Experimental setup to observe the transfer of orbital angular momentum to a freely rotating helical mirror placed at air-fluid interface. The back side of the spinner is painted to have naked-eye visualization of the rotation motion. (b) Set of 10 mm diameter helical mirrors with integer values of ℓ from -5 to 5. Note that $\ell = 1$ mirrors have two-ramp design. (c) Snapshots of the rotation of helical mirror with 10 mm diameter and $\ell = \pm 2$, at $\tilde{P}_0 = 3.5$. (d) Typical dynamics of the correlation coefficient between the image at time t and $t = 0$ and its corresponding frequency power spectra evaluated by fast Fourier transform processing (FFT).

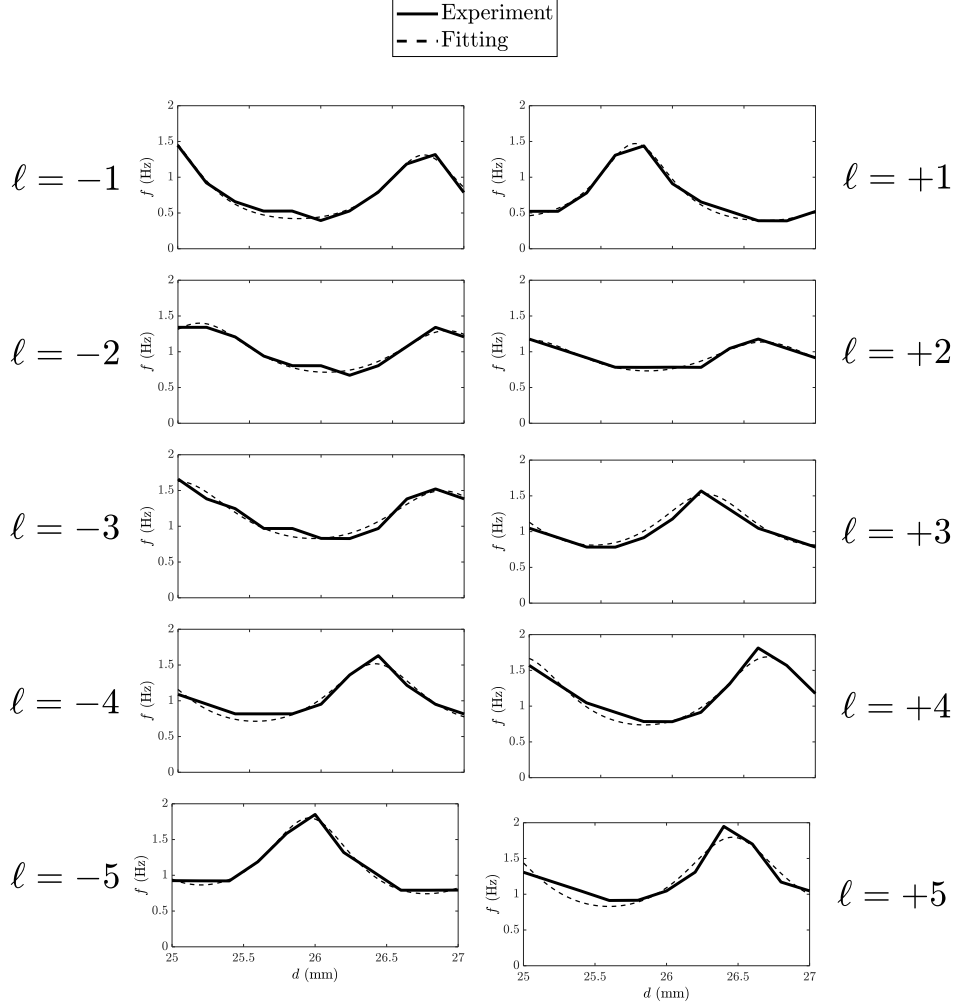


Figure 3.3: Measured spinning frequency as a function of d for helical mirrors with integer topological charge $-5 < \ell < 5$, and for total acoustic power $\tilde{P}_0 = 3.5$.

details of the observed trend is at first unclear, these preliminary results confirm the observation of a non dissipative transfer of angular momentum from sound to matter.

3.2 Towards a quantitative description

Once having experienced the first spinning dynamics, we extended the size of the used helical mirror to 30 mm diameter in order to better intercept acoustic wave within the explored range of distance between the transducer and the helical mirror. A new set of helical mirrors with integer topological charge from $\ell = 1$

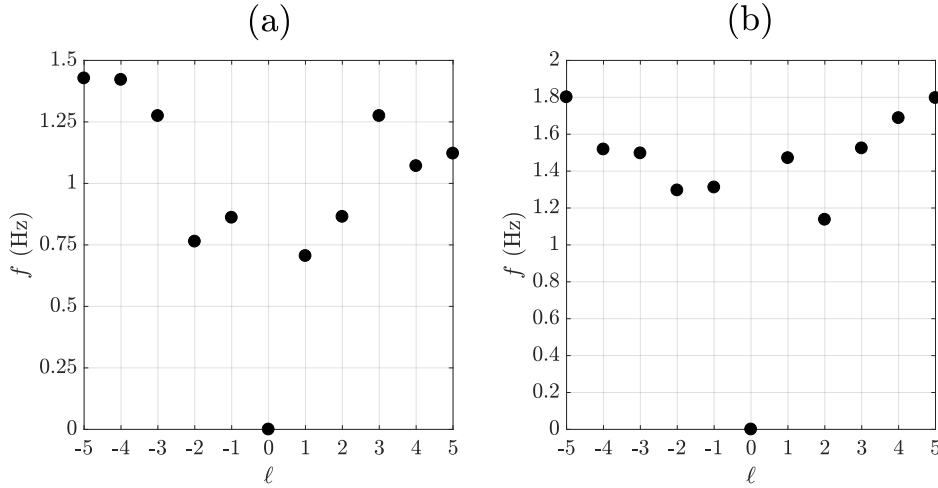


Figure 3.4: (a) Steady spinning frequency as a function of the topological charge ℓ for helical mirrors with 10 mm diameter, placed at 35 mm distance from the transducer and irradiated at a power level $\tilde{P}_0 = 3.5$. (b) Same as in (a) but taking the maximum frequency at the closest distance from $d = 26$ mm after a study in the range $25 \text{ mm} < d < 27 \text{ mm}$.

to $\ell = 5$ are fabricated for this purpose and additional two-ramp mirror $\ell = 1$. The power of the source is now set to $\tilde{P}_0 = 5.0$. Measurements of the rotational frequency is performed from $d = 0.5$ mm to $d = 25$ mm by steps of 0.15 mm. Concerning the video analysis, the extraction of correlation coefficients between frames is improved by painting half of the base of each mirror in white in order to have a periodic black-and-white pattern, see Fig 3.5(a). In addition to the painting, the effective size of video analysis is reduced to a smaller area closer to the center of rotation, and we increase the sampling rate of the video to 300 frames per second. For each d , 10 full turn rotation are recorded in order to ensure spinning frequency determination with identical precision using FFT processing, see Fig 3.5(b) that illustrates a typical result.

3.2.1 The particular case of $\ell = 1$

As said above, the helical mirror with $\ell = 1$ is available with on-ramp and two-ramp design. As mentioned in chapter 2, only the two-ramp design ensures on-axis rotation with respect to the center of mass. However, both mirrors are expected to experience the same transfer of angular momentum, hence they should spin the same frequency under identical irradiation conditions. The measured values of frequency as a function of d for $\ell = \pm 1$ are shown in Fig 3.6 for single-

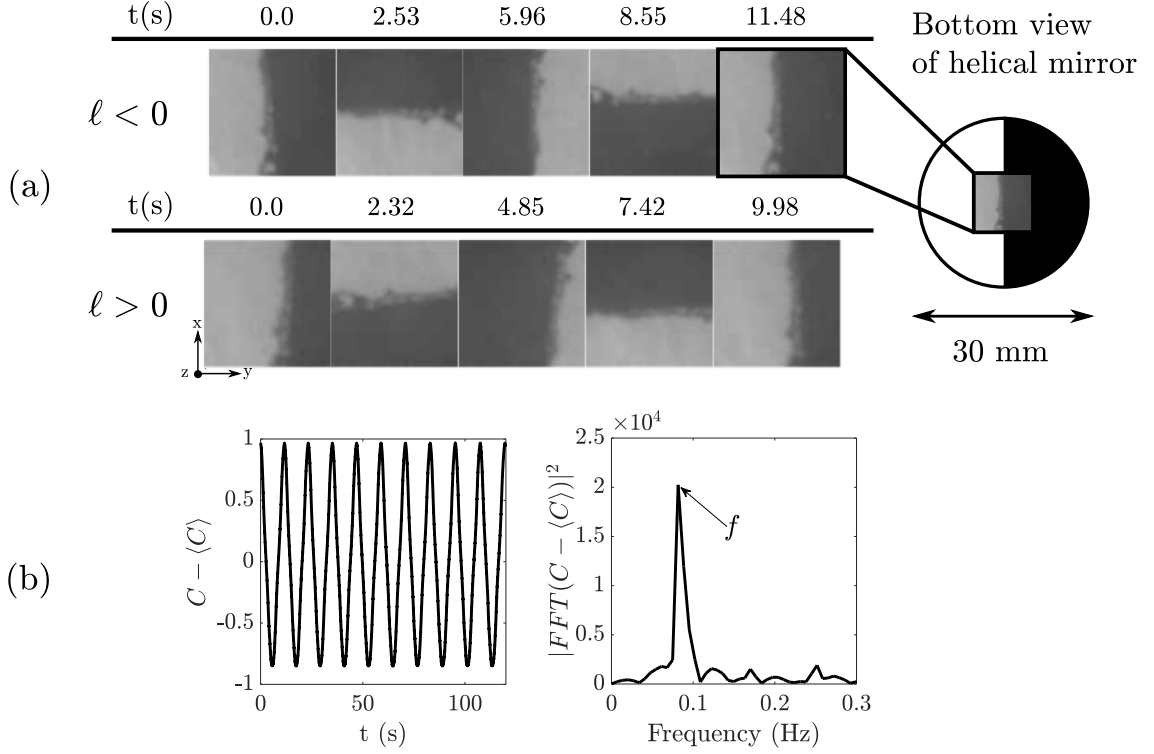


Figure 3.5: (a) Cropped snapshots of the rotation of left- and right-handed helical mirror with 30 mm diameter and $\ell = 1$, at $\tilde{P}_0 = 5$. (b) Typical correlation coefficient dynamics and corresponding FFT as in Fig. 3.2.

ramp and two ramp design. In both cases, an oscillatory behaviour is found, though its modulation depth is substantially larger for the two-ramp design. Since oscillating spinning frequency implies cavity effect between the transducer and the mirror, our observations clearly indicate distinct field distribution associated with the reflection of the incident wave as it impinges onto the mirror. In order to understand more quantitatively what is going on, we perform numerical BPM simulations and evaluate the total effective power actually acting on the mirror by taking in account 10 round-trips of the wave between the transducer and the mirror in both cases. The results are shown in Fig. 3.7(a). In fact, simulations predict striking different behaviour for the distance-dependent effective power P_{eff} . Namely, no oscillation is predicted for the single-ramp design while oscillations with long modulation depth occur for the two-ramp design. This can be understood by looking at the intensity distribution in the plane of the transducer after the first reflection of the mirror, see Fig. 3.7(b). Indeed, there is almost no reflected power bouncing back to the transducer for single-ramp, which

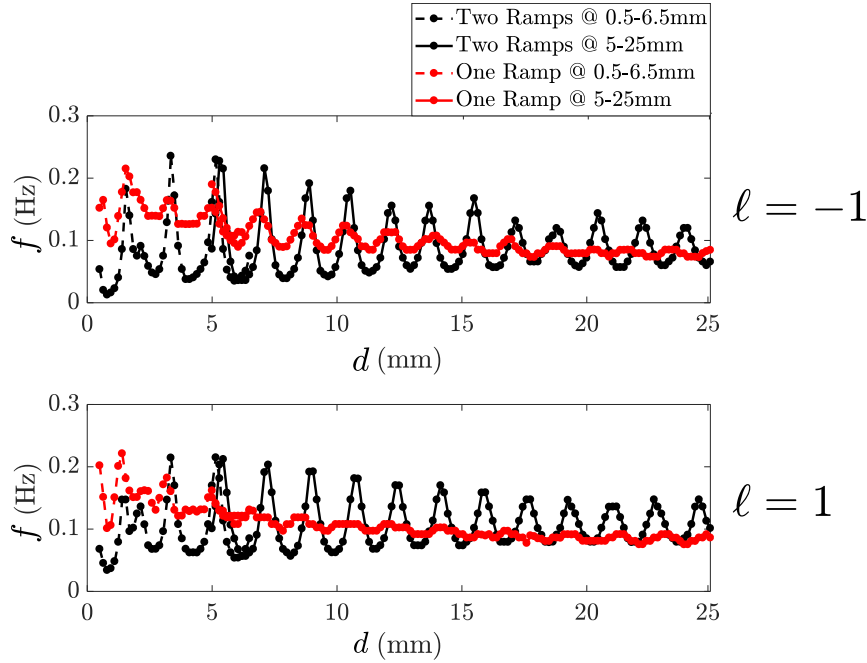


Figure 3.6: Frequency as a function of the distance for helical mirrors with 30 mm diameter and $\ell = \pm 1$, for single-ramp and two-ramp designs, at $\tilde{P}_0 = 5$. Experiments in the range of 0.5-6.5 mm and 5-25 mm correspond to two independent experimental set of measurements, which explains the slight mismatch of the data around $d = 5$ mm.

prevents cavity effects to take place, in contrast to the two ramp design. Interestingly, the occurrence of the residual oscillations observed experimentally can be grasped by noting that fabricated helical mirror are never perfectly matching with the designed spiral step height, as discussed in chapter 2. This is illustrated in Fig. 3.7(c) where we compare the spinning frequency as a function of d for $\ell = 1$ and $\ell = 1.1$, assuming a 10% deviation for the step height. The corresponding reflected intensity profile in the plane of the transducer for $d = 25$ mm is shown in Fig. 3.7(d). Summarizing, the emergence of oscillations associated with broken axisymmetry for the reflected field supports our previous qualitative explanation.

3.3 Influence of the topological charge

The spinning experiments as a function of the distance are performed for the helical mirrors with integer charge from $\ell = 1$ to $\ell = 5$ at a distance $0.5 < d < 25$ mm. The experimental results are summarized in Fig. 3.8(a). The amplitude

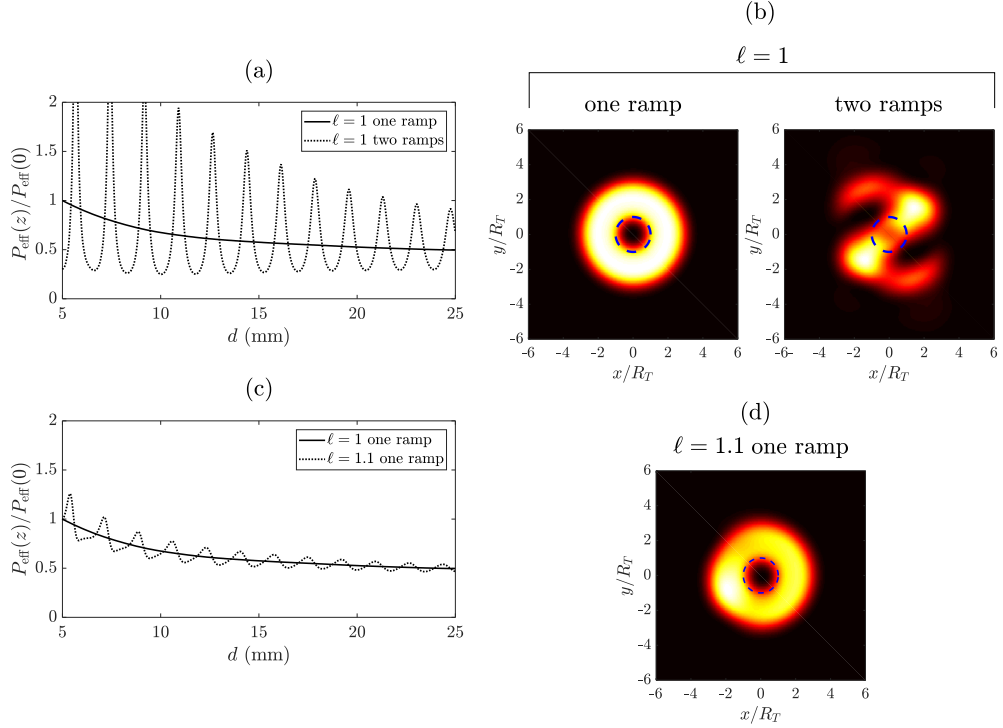


Figure 3.7: (a) Simulations of the normalized effective power impinged on the helical mirror for $\ell = 1$ as a function of d , both for single-ramp and two-ramp designs. (b) Calculated normalized intensity distribution of the field reflected from the mirror in the plane of the transducer (see its contour indicated by dashed circle taking $d = 25$ mm). (c) Same as in (a) but for $\ell = 1.1$. (d) Same as (b) but for $\ell = 1.1$.

of the oscillations for the spinning frequency as a function of d decreased as d increased. Eventually, the frequency settles around a constant value between 20 mm and 25 mm. Therefore, we choose to report on the dependence on the topological charge by taking the mean and standard deviation values of frequency determined from the latter interval for d . The corresponding results of frequency as a function of the topological charge are shown in Fig. 3.8(b).

3.4 Determination of the acoustic torque

3.4.1 General consideration

Now that we have access to the spinning frequency as a function of ℓ , a model is needed to extract a measurement of the acoustic torque from the experimental data. As sound reflects off the helical mirror, its amplitude acquired a pure

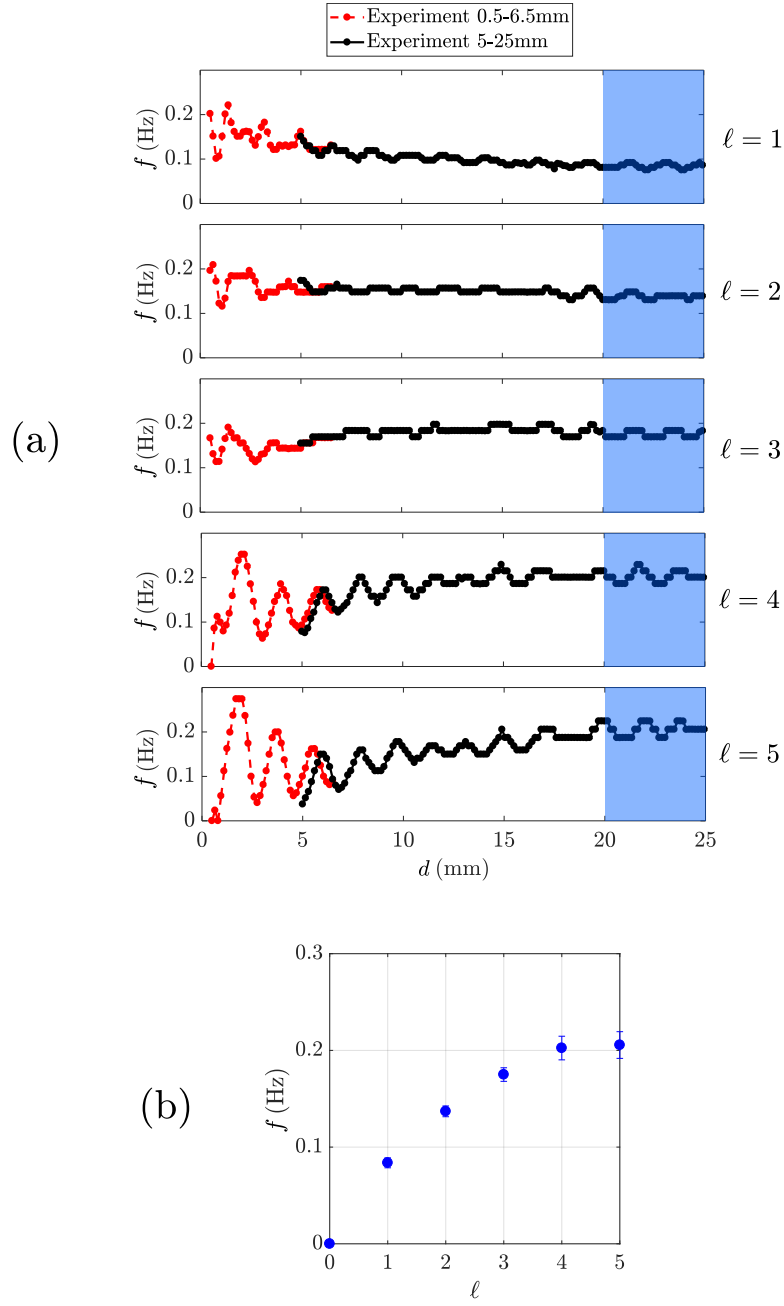


Figure 3.8: (a) Spinning frequency as a function of distance from the transducer for integer topological charges $1 \leq \ell \leq 5$ in the range 0.5 – 25mm for 30 mm-diameter helical mirrors and power $\tilde{P}_0 = 5$. The shaded area refer to the range over which is made an average for reporting on the dependence of f on ℓ . (b) Experimentally measured spinning frequency f as a function of ℓ according to the data presented in (a).

phase factor $\exp(-i\ell\varphi)$ by considering the helical mirror as a pure helical phase mask, which assumes ideal helical morphology and neglects diffraction effects over spatial scales of the order of the wavelength (let us recall that $h_s \sim \lambda$). The conservation of the total angular momentum for the “sound-matter” system implies that an acoustic torque $\vec{\Gamma} = \frac{\ell P}{\omega} \vec{z}$ is exerted on the helical mirror.

With the aim at measuring the acoustic torque, we rely on the equation of motion of the rotating helical mirror, whose time-dependant angular frequency dynamics $\Omega(t) = \frac{d\varphi}{dt}$ is described by the equation:

$$J \frac{d\Omega}{dt} = \Gamma_{\text{ac}} + \Gamma_{\text{visc}} \quad (3.1)$$

where $\vec{\Gamma}_{\text{visc}} = \Gamma_{\text{visc}} \vec{z}$ is the viscous drag torque exerted in the rotating object, whose value Γ_{visc} depends of the sign of the topological charge. At steady state, the acoustic radiation torque and the viscous torque are balanced, namely, $\Gamma_{\text{ac}} + \Gamma_{\text{visc}} = 0$. In other words, if we are able to measure the viscous torque, we are measuring the acoustic one. To do so, an option consists in describe quantitatively the viscous torque.

The simplest approach is that neglecting inertial effects, which implies that the Reynolds number $\text{Re} = \frac{\Omega D^2 \rho}{4\eta}$ is small enough, where η is the dynamic viscosity of the surrounding fluid and ρ its density. In that case, Γ_{visc} is a linear function of Ω according to

$$\Gamma_{\text{visc}} = -\frac{16}{3} \eta R^3 \Omega \quad (3.2)$$

which is an analytical formula taken from the case of infinitely thin disk immersed in an unbounded fluid. Note that the latter formula neglects the influence of the upper half-space due to the high contrast of viscosity between the air and the fluid. In the case of air-water interface we have that $\eta_{\text{liquid}}/\eta_{\text{air}} \sim 7 \times 10^2$.

Using the value of power obtained in chapter 2, namely 20.5 mW, we obtain the prediction shown in Fig. 3.9 by the red markers. There is an important quantitative mismatch with the experimental data. In fact, we can understand the latter once the Reynolds number is evaluated since we find $\text{Re} \sim 300$. Nevertheless, even though the Stokes approximation is not valid, we can benefit from the analytical derivation of the inertial correction to the viscous torque made by Ovseenko [41]. Namely, the first-order correction expresses as:

$$\Gamma_{\text{visc}}^{\text{nl}} = -\frac{16}{3} \eta R^3 \Omega (1 + \alpha \text{Re}^2) \quad (3.3)$$

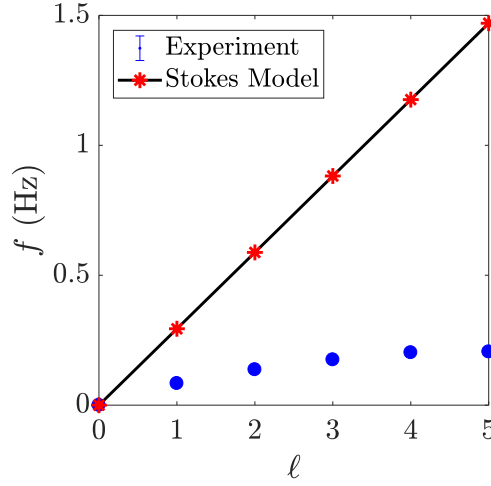


Figure 3.9: Frequency f as a function of topological charge ℓ for experimental values and theoretical values of frequency derived from a Stokes model for the viscous torque.

where α is an adimensional parameter that depends to the geometry and boundary conditions of the system. According to Ovseenko, we have in our case $\alpha \simeq 7 \times 10^{-4}$. In order to test such inertial correction, we perform a non-linear fitting of the experimental values by balancing Eq (3.3) with the acoustic torque, say

$$\Gamma_{\text{visc}}^{\text{nl}}(\alpha, \Omega, \Omega^3) + \frac{\ell}{\omega} P_{\text{eff}} = 0 \quad (3.4)$$

by setting P_{eff} and α as adjustable parameters. This is illustrated in Fig. 3.10 where the result of the non-linear fitting is shown as the blue curve, which gives $\alpha = 0.14 \times 10^{-4}$ and $P_{\text{eff}} = 10.1$ mW which corresponds to a value of acoustic power smaller than the one directly measured.

3.4.2 Viscous torque corrections: a comment

Here we would like to stress that the observed non-linear dependence of the spinning frequency as a function of the topological charge is not particular to our experiments. Indeed, this has also been reported by Demore et al. [37] when measuring the transfer of angular momentum by absorption of acoustic vortex beam, see Fig. 3.11(a), and more recently by Li et al. [38], see Fig. 3.11(b). In the article by Demore et al., the non-linearity is attributed to an experimental drawback leading to a decrease of the incident beam power as the topological charge increases. However, if we consider from their experiments the lowest ro-

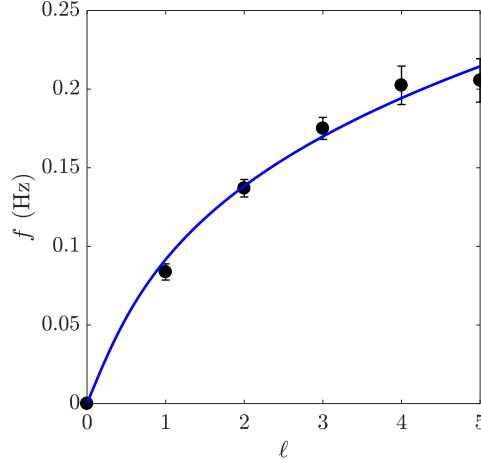


Figure 3.10: Fitting of the experimental data shown in Fig. 3.9 according to the balance between the acoustic torque and the corrected viscous torque given by Eq. (3.3).

tation frequency expected from the Stokes approximation given a unit charge incident vortex, a minimal absorbed power of 20 W, the 550 kHz carrier frequency and the 10 cm diameter absorbing disk, this leads to $\alpha \text{Re}^2 \sim 10^5$. We therefore point out here that a likely explanation of the unexpected non-linear trend observed experimentally relies in the stray deviation to the Stokes approximation. Nevertheless, we note that Demore et al. were able to be quantitative at the end of their study, by making observations at the early stage of the dynamics where initial corrections of the viscous torque were not yet fully at work. In the case of Li et al., their attempt to measure experimentally the acoustic radiation torque is based on the Stokes approximation. Noting that they observed

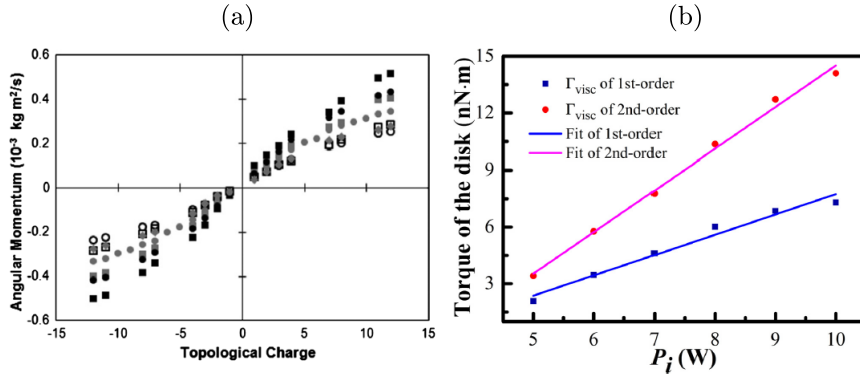


Figure 3.11: (a) Angular momentum as a function of the topological charge for different acoustic power values. (b) Torque as a function of incident power. Adapted from [37] and [38].

typically 10 Hz rotation frequency with 5 mm-radius absorbing objects, one gets $\alpha \text{Re}^2 > 10$. Therefore, a non-linear correction to the viscous torque must be taken in account for a quantitative attempt to measure the acoustic torque, which was unfortunately not done by the authors.

3.5 Improving the experimental implementation

3.5.1 Upgrading experimental setup

The previous section has shown the necessity to pay attention to the Reynolds number while modelling the viscous drag towards a quantitative assessment of the acoustic radiation torque from spinning experiments. From the experience learned during previous experimental attempts, a new round of improvements for the experimental setup has been made. Namely:

- *Contact line control*

In the previous experimental setup, the helical mirror was capillary trapped and centered in the middle of the pool owing to the meniscus formed by the edges of the pool and the edge of the mirror. We realized that the contact line at the edge of the mirror presented an irregular pattern that depends of the topological charge. As the disk starts to rotate, the broken axisymmetry prevents from a safe modelling using axisymmetric Stokes flow. In order to solve this situation, the helical mirror is now placed on a circular pedestal of 32 mm diameter and 1 mm of thickness. Therefore, when the system ‘mirror + boat’ is placed at the air-water interface, the contact line attaches at the rim of the boat, hence ensuring an axisymmetric fluid interface environment.

- *Taming acoustic reflection feedback from air-water interface*

As the accurate modelling of the observed effects implies a good knowledge of the acoustic field, it is relevant to minimize any influence of unwanted reflections by optimizing the design of the setup. Here, we improve the system by placing a circular aperture with 32 mm diameter at the top of the pool in order to suppress sound reflection from the curved air-water interface around the mirror that could reach the transducer.

- *Trade-off between spinning frequency and Stokes approximation*

In order to reduce the value of αRe^2 , a mixture of water and glycerol is used instead of pure water. Adjusting the fraction of glycerol added to the water, the density and the viscosity are modified, which allows a fine control of the value of Re . A set of experiments with different glycerol-water ratios is performed to define optimal operation conditions.

- *Taming Fabry-Perot modulation of the spinning frequency*

As we illustrated Fig. 3.6, the cavity effects between the mirror and the transducer may lead to substantial modulation of the spinning frequency depending on the distance between the mirror and the transducer. This is a drawback in terms of reproducibility between different events due to our limited precision when setting the distance d . However, we learned from previous attempts that the modulation depth of the d -dependant spinning frequency becomes fairly negligible at $d \sim 25$ mm. Therefore, further experiments are performed imposing $d = 25$ mm.

- *Motion tracking sensibility*

To improve the sensibility of the detection of the spinning angular dynamics a small mark is painted at the bottom of the boat, at its rim, see Fig. 3.12.

A sketch of the improved experimental setup is shown in Fig. 3.12. Before reporting on the results obtained with this upgraded approach, hereafter we first present a study from which we eventually choose an appropriate glycerol-water mixture.

3.5.2 Defining the appropriate Glycerol-Water mixture

In order to safely neglect the role of inertial effects on the viscous drag torque, we are searching a condition where $\alpha\text{Re}^2 \ll 1$ taking our evaluation $\alpha \sim 10^{-4}$. Experimentally, this can be tested by measuring the spinning frequency for various glycerol-water mixtures. Since the determination of Re also requires the knowledge of ρ and η of the fluid, we extracted them from the empirical formulas of Cheng [42]. The values of density and viscosity for different weight fractions of glycerol in water at experimental laboratory conditions of 1 atm of pressure and a temperature of 22° are depicted in Fig. 3.13. The red dots in Fig. 3.13 corre-

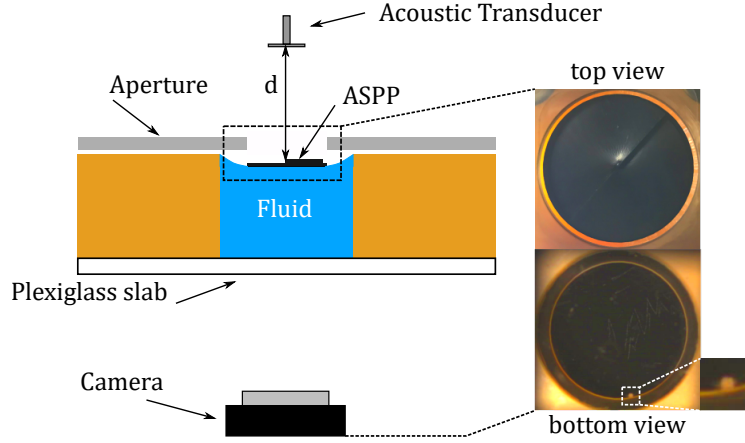


Figure 3.12: Sketch of the improved experimental setup. An aperture of 32 mm of diameter is placed on top of the pool and aligned with the mirror. A small marker is painted to the boat of the mirror to follow the angular displacement of the disk.

spond to the glycerol %wt values chosen for the spinning frequency experiments. These experiments are performed with a helical mirror with $\ell = 4$ placed at a distance of $d = 25$ mm from the transducer and incident power \tilde{P}_0 . The results are summarized in Fig. 3.14. Obviously, larger quantities of glycerol is preferable, however, this comes with a drastic reduction of the spinning frequency, which is detrimental for the sake of a robust measurement when considering extensive experimental investigations. Therefore we choose 80%wt glycerol as a practical trade-off for our investigation at $d = 25$ mm.

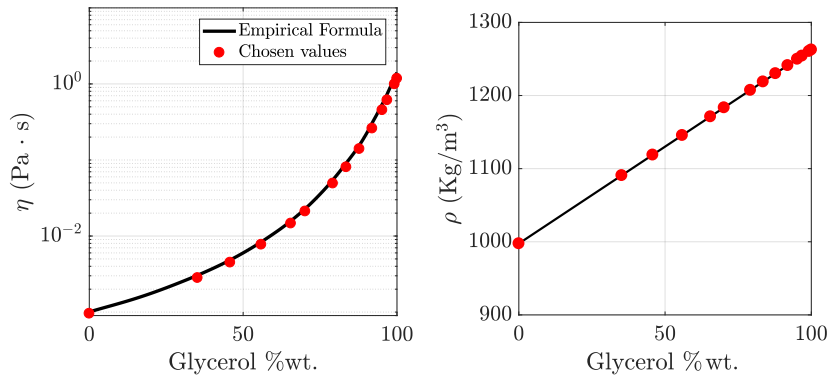


Figure 3.13: Solid lines: density and viscosity for different ratios of glycerol-water mixtures from [42]. Red dots: values used in the experiment.

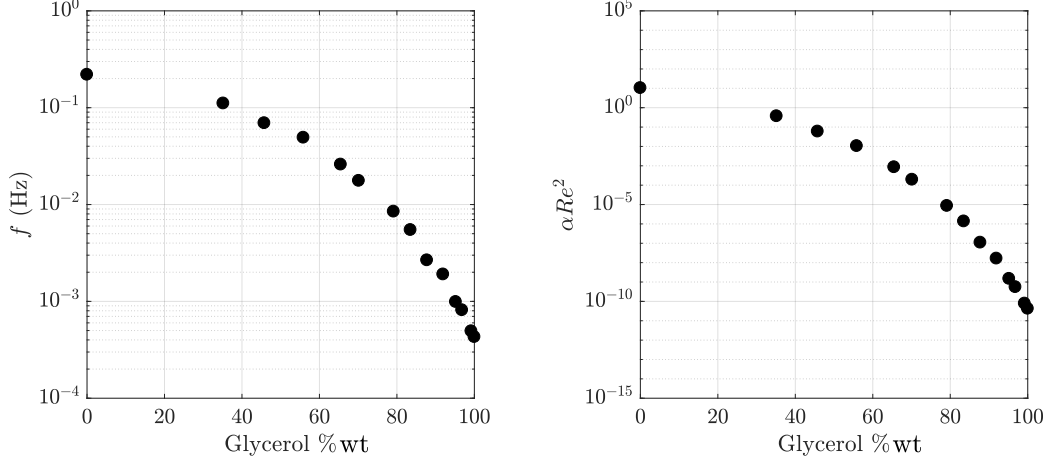


Figure 3.14: (Left) Experimental results of spinning frequency for different mixtures of glycerol %wt (see text for experimental conditions). (Right) Correction coefficient αRe^2 associated to the experimental values of frequency, accounting for the actual values of density and viscosity according to Fig. 3.13.

3.6 Quantitative measurements: first attempt

A set of 5 experiments are performed at a distance $d = 25$ mm, one for each topological charge. The experiments consists in irradiating the mirror at constant power $\tilde{P}_0 = 5$ for 15 min and measurement of spinning frequency is made at steady state. Experimental results are shown in Fig. 3.15. Observed rotational motion is robust and almost free from noise as illustrated in 3.15(b) that shows a typical circular motion of the marker at the bottom of the helical mirror. These results allow evaluating the acoustic torque via Stokes model via the relationship, see Fig. 3.16(a) (red markers)

$$\Gamma_{ac}^{\text{Stokes}} = \frac{32}{3} \pi \eta R^3 f \quad (3.5)$$

Fitting curve obtained according to $\Gamma_{ac}^{\text{Stokes}} = \frac{\ell P}{\omega}$ using P as the single adjustable parameter gives $P^{\text{Stokes}} = 7.8$ mW, see dash line in Fig. 3.16(a). The obtained power value is substantially different from the expected power of 14.8 mW from the analysis made in in chapter 2. In particular, we noticed that at $d = 25$ mm corresponds to a minimum of the effective power experienced by the mirror. The obtained power mismatch invites us to question the validity of the Stokes modelling, keeping in mind that the experimental system does not correspond to the criteria of an unbounded fluid.

Therefore, in order to solve this issue, we performed a model-free approach in

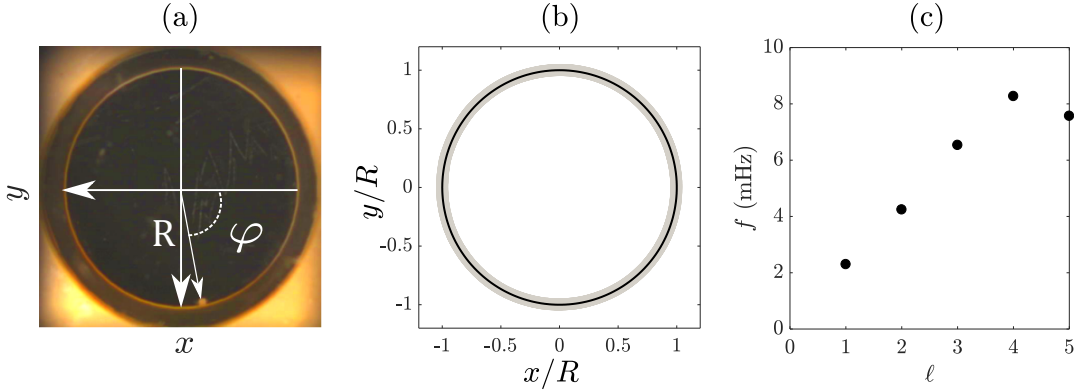


Figure 3.15: (a) Photo of helical mirror from behind showing the tracker as a white dot at a distance R from the center. (b) Typical trajectory of the marker (grey) during the rotation of the mirror adjusted by a circle (black). (c) Spinning frequency as a function of ℓ .

the Stokes regime, by writing

$$\Gamma_{\text{ac}}^{\text{Free}} = C \langle \Omega \rangle \quad (3.6)$$

where $\langle \Omega \rangle$ is the steady angular spinning frequency and C is the viscous coefficient. In this case, the angular spinning frequency is extracted from the angular displacement of the marker printed on the back side of the mirror, see Fig 3.16(b). From Fig. 3.16(b), the corresponding long-term linear dependency of the azimuthal angle referring to the angular position of the marker, emphasizes the stationarity of the experiment, that is to say a constant value of power delivered by the transducer as well as a stable air-water interface. From the slope of the linear fitting of the steady angular displacement, we extract $\langle \Omega \rangle$. The viscous coefficient is extracted from the study of the relaxation dynamics once the irradiation is turned off at $t = t_0$. The relaxation dynamics derived from Eq. (3.1) is expressed as

$$\varphi(t) = \Omega(t_0)t - \Omega(t_0)\tau [1 - e^{-t/\tau}] \quad (3.7)$$

where $\tau = J/C$ the characteristic relaxation time. We evaluate C by fitting the data for over 1 s duration using Ω_s and τ as adjustable parameters, noting that J is measure independently, see Fig. 3.16(b) dark thin curve. This was done for 5 independent experiments for each ℓ from 1 to 5 for two distinct pedestal. For each experiment, the helical mirror is replaced according to the protocol described earlier. The evaluated results of acoustic torque derived from a model-free viscous drag is shown in Fig. 3.16(a) black markers. Noticing that Stokes

model and model-free analysis shows good agreement for $\ell = 1$ to 4. For $\ell = 5$, the behaviour between the two models presents differences in terms of the predicted torque, which could be associated to the fact that the experiments were made in one-shot and no statistics were performed. Nevertheless, in the model-free calculation the trend associated to the linear behaviour of the acoustic torque as a function of ℓ is preserved. Just like in the Stokes model, a linear fitting is performed setting P as fitting parameter. The value of power associated in this case corresponds to $P^{\text{Free}} = 8.9$ mW. Therefore, we still face the issue of power mismatch that we do not understand.

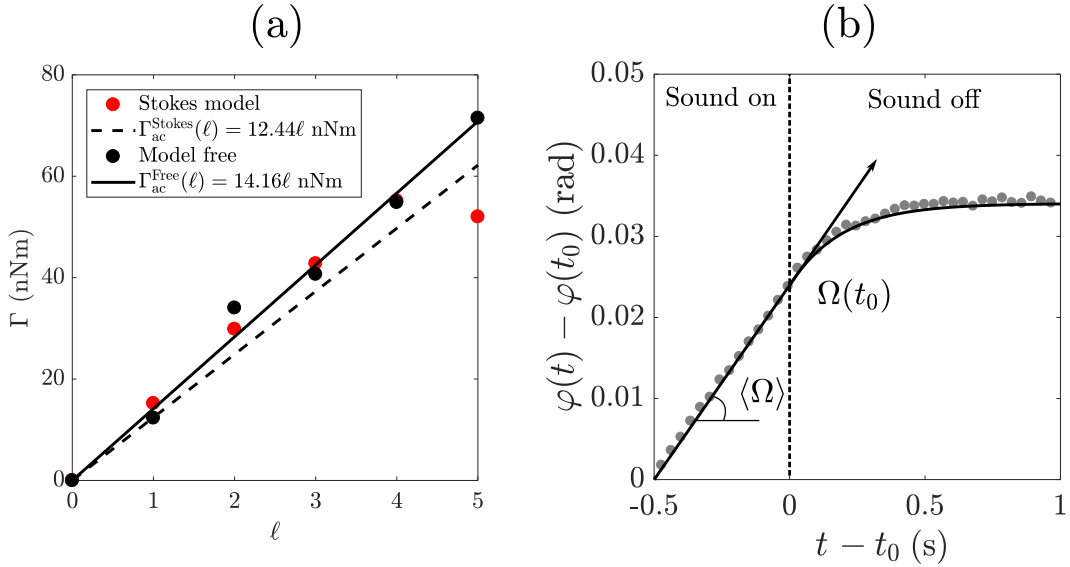


Figure 3.16: (a) Experimental values at 85 glycerol %wt of acoustic torque extracted from Stokes model (red marker) and model-free (black marker), and linear fitting for each model. The five experiments were performed in one-shot, so no statistics were performed. The values of power P extracted from the linear fitting corresponds to $P^{\text{Stokes}} = 7.8$ mW and $P^{\text{Free}} = 8.9$ mW. (b) Typical relaxation dynamics of the angular position of the helical mirror, where $t = t_0$ refers to the time at which the acoustic source is turned off. Thick gray curve: experimental data. Dark thin curve: fit giving access to the ratio C/J . Data refers to $\ell = 5$ helical mirror.

3.7 Quantitative measurement: final attempt

3.7.1 Improvement of experimental setup

In order to drastically get rid of undesirable cavity effects, the most convenient option is to increase d , which is made at the expense of the power intercepted by the helical mirror. The corresponding drawback regarding ensuring the reduction of the spinning frequency is mitigated by reducing the viscosity, while preserving αRe^2 sufficiently small. In order to help the decision, we performed simulation of the power $P(d)$ intercepted by the helical mirror and the corresponding power $P^*(d)$ intercepted by the transducer. The results are summarized in Fig. 3.17. From the simulation, we choose $d = 100$ mm as a practical trade off between maximizing the power intercepted by the helical mirror and minimizing the Fabry-Pérot cavity effect between the mirror and the transducer, which is favoured at larger distances. This is illustrated in Figs. 3.17(a) and 3.17(b) that respectively display the dependence in power P on the distance d and the corresponding P^* of the reflected field intercepted by the transducer. This was calculated by using BPM of the propagated acoustic field from the transducer, calculating the power $P(d) = \int I(d)dS$ in the area S of the helical mirror for different distances of d . Each value of $P(d)$ was normalized to the power in the plane of the transducer $P(0)$. The calculations of P^* were performed by calculating the intensity field of the reflected acoustic beam in the plane of the transducer, integrating in the area of the transducer and normalizing to $P(0)$. The (x, y) meridional cross-section of the calculated normalized intensity distribution $\tilde{I} = |A(x, 0, z)|^2 / \max_{x,y}[|A(x, 0, z)|^2]$ of the incident and reflected field for $d = 100$ mm are shown in Figs. 3.17(c) and 3.17(d). In particular Fig. 3.17(d) allows qualitative understanding of the dependence of P^* on ℓ displayed in Fig. 3.17(b). Indeed, the doughnut intensity profile of the reflected vortex wave leads to a drastic reduction at short distance ($d \lesssim 10$ mm) of the cross-section of the field with the transducer when using an helical mirror ($\ell \neq 0$) instead of a flat one ($\ell = 0$). This effect is strengthened as ℓ increases as expected from the fact that the area of the vortex core region increase with $|\ell|$. For intermediate distance ($10 \lesssim d \lesssim 100$ mm), interference between the field contributions from the flat mirror and the helical mirror leads to non monotonous behaviour. This is supported by the case of $\ell = 1^*$ referring to an helical mirror of infinite extension, which exhibits no power oscillation. Finally, the behaviour at large distances

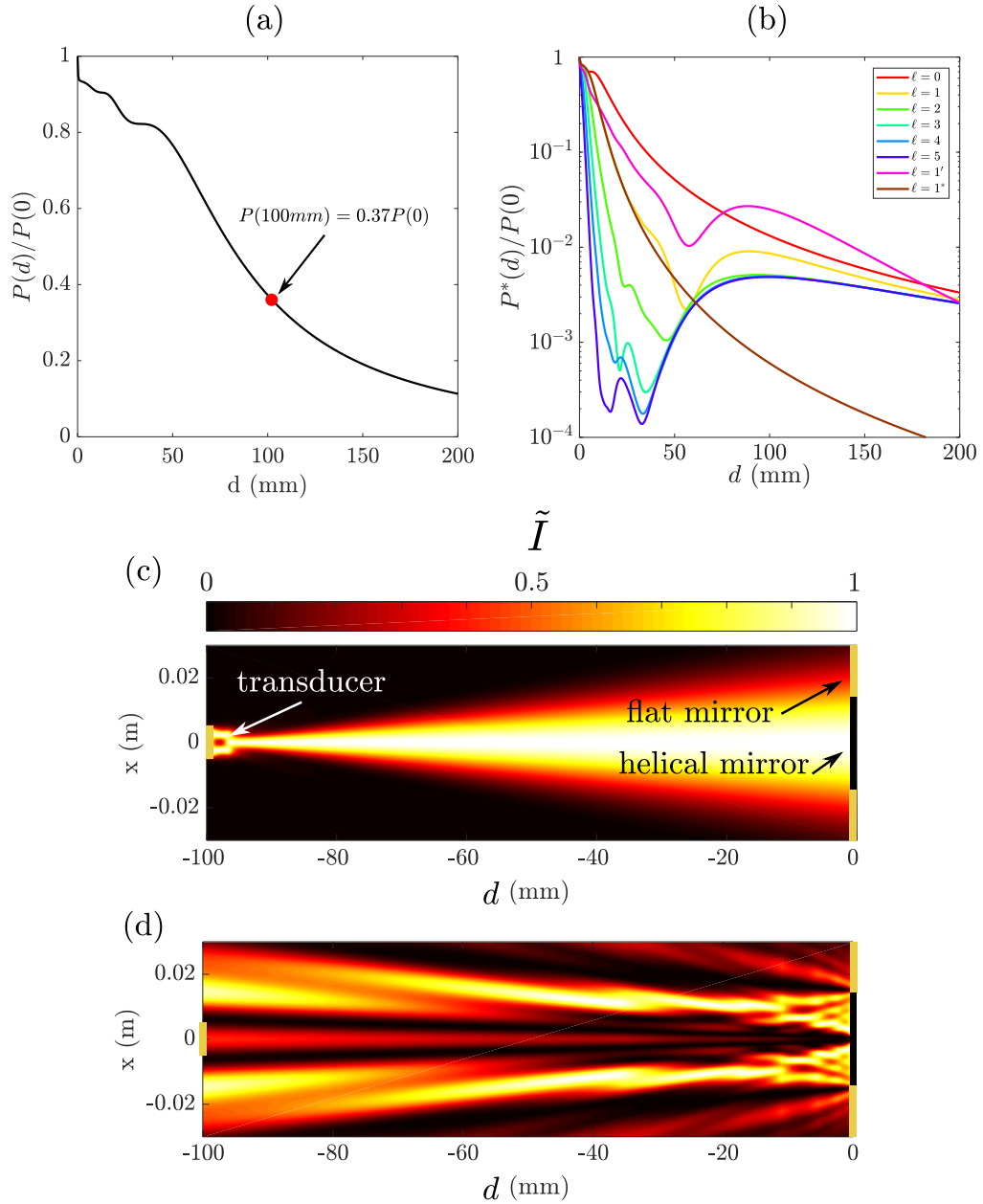


Figure 3.17: (a) Power P intercepted by the helical mirror placed as a function of its distance d from the transducer. (b) Corresponding power P^* of the wave reflected field intercepted back by the transducer for $0 < \ell < 5$ and $\ell = 1'$ corresponds to two-ramp $\ell = 1$. Also, $\ell = 1^*$ refers to helical mirror with infinite extent. Both P and P^* are normalized to the total output power P_0 of the transducer. (c) Normalized intensity distribution of the incident wave in the meridional plane (x, z) as a function of d . (d) Same as panel (c) for the reflected field with $\ell = 2$.

($d \lesssim 100$ mm) is dictated by the reflection from the outer plate leading to a nonzero on-axis intensity, see 3.17(d), and an asymptotic behaviour independent of $|\ell|$. From Fig. 3.17(a) we can see that the power at $d = 100$ mm corresponds to $P(100\text{mm}) = 0.37P_0$. As we are working in the Stokes regime, it is expected that at the value of rotational angular frequency to be affected reducing the possibility of detection. To solve this issue, a mixture of glycerol of 65 %wt is used as it has shown to be a good compromised between angular frequency and viscosity to keep the condition of $\text{Re} \sim 1$.

For this novel set of experiments, two further improvements are brought, see Fig. 3.18(a). The first modification consists in improved reproducibility in the air-water-spinner surface. This is done by extracting water from the pool until the upper face of the helical mirror aligns with the upper surface of the pool. Another benefit of this method is that the measurement of the distance from the transducer to the disk can be done directly with a ruler placed at the side of the pool, without touching the mirror. The second modification consists in a new way to align the transducer with the center of the mirror. In previous experiments, the centering was performed by using an optical fiber passing through the hole at the center of the transducer. However, after a few centimeters, the optical fiber is no longer straight enough due to its coiled packing. This is solved by illuminating the transducer hole with a white light source making a cone of light that illuminates the helical mirror. As the cone of light and the transducer have a common axis, by centring the cone of light with the helical mirror we ensure the alignment of the mirror with the transducer. Finally, to define the instant t_0 at which the acoustic source is blocked, an visual element that appears in the video while the source is blocked is introduced to the experiment, see Fig 3.18(b).

3.7.2 Acoustic torque measurement

A set of 5 independent experiments per helical mirror are performed using two boats of 30 mm diameter. The use of another boat was to show that the experimental values of acoustic torque are independent to the boat used. For each experiment, the helical mirror is removed and replaced according to the protocol described earlier. The experiment consists in recording the steady state and relaxation dynamic of the mirror while irradiated at power $\tilde{P} = 5$. From each

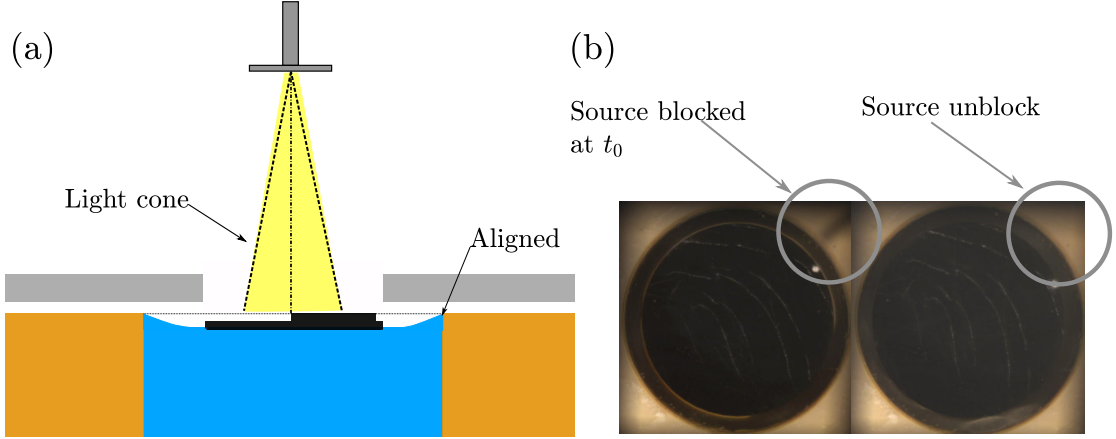


Figure 3.18: Third modification of the experimental setup protocol. (a) A white light source is used to illuminate through the hole of the transducer up to the helical mirror. The center of the light cone associated with the center of the transducer is aligned with the axis of the helical mirror to ensure alignment between transducer and helical mirror. (b) A needle (that moves with the beam blocker) was placed between the pool and the camera, working as a visual system that indicates the time t_0 of the blocking of the acoustic source and the beginning of the relaxation. Despite being out of focus, it is easily distinguishable.

experiments, values of C , $\langle \Omega \rangle$ and $\Omega(t_0)$ are extracted in the same manner as in the case of $d = 25$ mm. Example of steady state and relaxation dynamics for $\ell = 1$ to 5 are shown in Fig. 3.19. Since the steady rotation and the relaxation dynamics are associated with distinct irradiation conditions, we evaluated the acoustic torque from irradiation-free quantities, namely, $\Gamma = C\Omega(t_0)$ noting that $\frac{\Omega(t_0)}{\Omega} = 1.08 \pm 0.18$, see Fig. 3.21 to see the ratio of $\frac{\Omega(t_0)}{\Omega}$ for different topological charges. The results of these 50 independent experiments are shown as black circle marks in Fig. 3.21(b). The results are generalized to half-integer topological charges $\ell = n - 1/2$ with n an integer from 1 to 5, which is done by using an n -step design with n -dependent step height $h_n = \frac{\lambda}{2} \left(1 - \frac{1}{2n}\right)$. Here again, five independent experiments are performed for each value of ℓ . The corresponding results of these 25 independent additional experiments are shown as blue squares in Fig. 3.21(b). Noteworthy, non-integer values of ℓ do not correspond to the case of pure mode vortex conversion as originally discussed with Allen et al. This is illustrated in Fig. 3.20, which corresponds to intensity and phase at the far field of acoustic waves reflected from the helical mirrors with topological charge $\ell = 1/2, 1, 3/2$ and 2 discarding the outer contribution reflected off the outer flat mirror. Indeed, axisymmetrical doughnut-shape intensity profile and on-axis

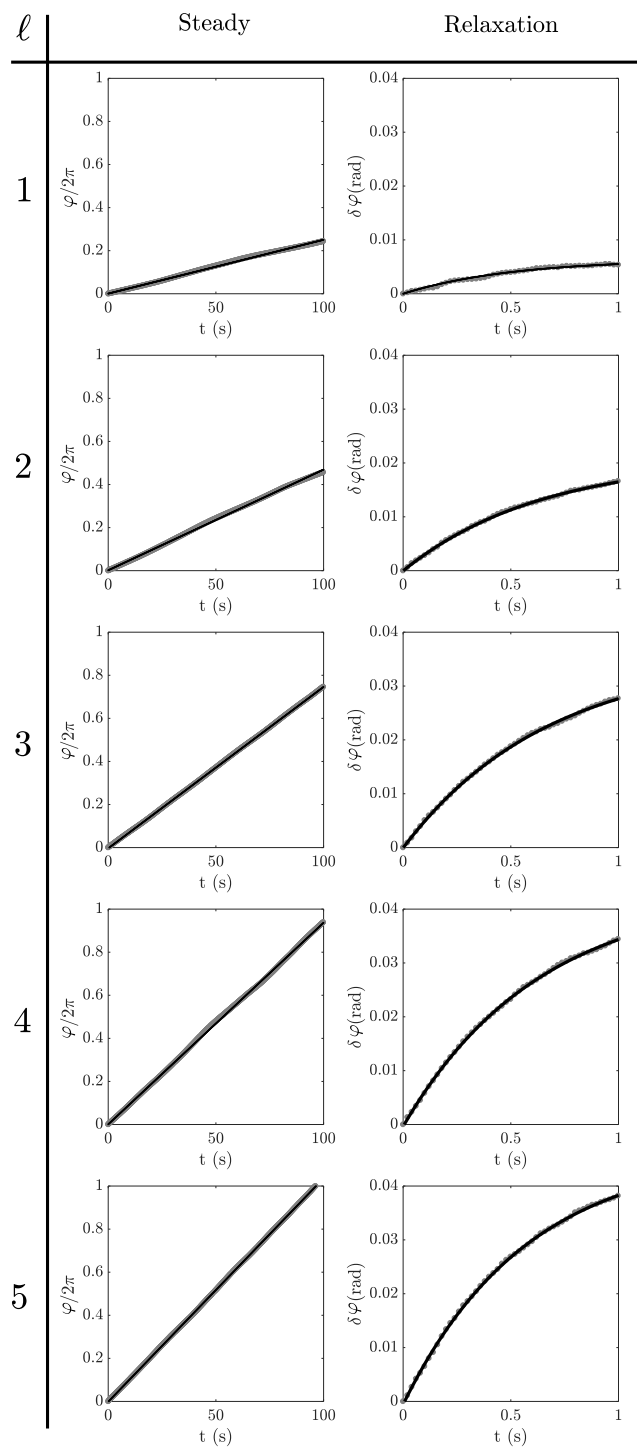


Figure 3.19: Experimental values and fitting of angular displacement as a function of time at steady and relaxation state of helical mirror of $\ell = 1-5$.

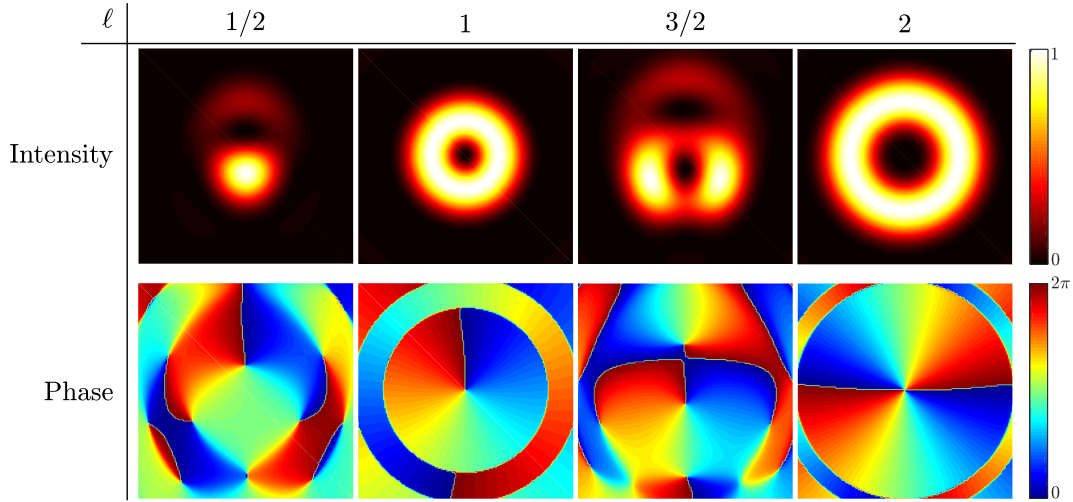


Figure 3.20: Calculated far-field intensity and phase distribution of the wave reflected off from an helical mirror with topological charge $\ell = 0.5, 1.0, 1.5$ and 2.0 .

phase singularity with topological charge $\ell' = -\ell$ is obtained for integer ℓ while a constellation of singularities with charges $\ell = \pm 1$ emerges otherwise. Quantitative agreement is assessed recalling the expression $\Gamma = \frac{\ell P}{\omega}$, which holds for non integer values of ℓ as well. Linear fit of the data displayed in Fig. 3.21(b) using P as adjustable parameter gives $P = 4.0$ mW, which corresponds to a value of power lesser than the one measured.

At this point of the experiment, the reason of this mismatch of power was still a mystery. Knowing that the protocol of extraction of C and $\Omega(t_0)$ was robust, we suspect in the experimental setup used for measuring radiation pressure at normal incidence. For that case, we decided to re-do mass measurement investigations by changing the equipment. Indeed, previous scale (AE Adam, PW 254) was sometimes giving null-mass measurement as sound irradiation of the test-disk is switched on, which were discarded when collecting a set of independent measurements leading to $m = 5.8 \pm 0.3$ mg. We now use another scale (Denver Instrument, M-220) that also has a 0.1 mg precision. The disk, a ℓ -diameter disk is placed on a pillar at 10 cm distance from the transducer (see sketch below). Any spurious wave contribution that does not intercept the disk is discarded by using a blocking plate (few mm-thick Plexiglass plate with a hole having a diameter slightly larger than the diameter of the pillar), see Fig. 3.22. We measure $m = 5.0 \pm 0.2$ mg by repeating 10 times the protocol illustrated in Fig 3.22(b). Namely,

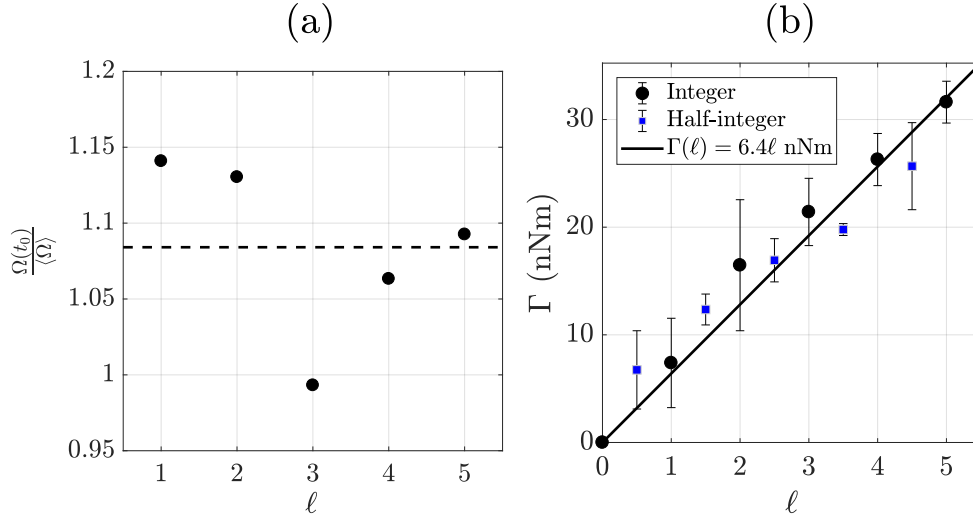


Figure 3.21: (a) Ratio of $\Omega(t_0)$ and $\langle \Omega \rangle$ as a function of the topological charge. (b) Acoustic torque as a function of its topological charge. Markers: experimental data. Solid line: linear fitting.

- 1) zeroing with no sound irradiation on the disk using a plastic beker
- 2) measurement
- 3) check of non-hysteresis once sound irradiation is off

Noting that the helical mirrors have a 30mm diameter, the sought-after acoustic power P expresses is $P = \frac{mgc}{2} \left(\frac{30}{32}\right)^2 = 7.5 \pm 0.3$ mg. We also performed an additional experiment to measure the total power P_0 , which consists to irradiate the scale at 45° incidence angle, by placing the transducer close enough the scale to ensure that all power is reflected, see Fig. 3.22(c). Measured mass $m = 10.4$ mg gives $P_0 = \frac{mgc}{\sqrt{2}} = 24.3$ mW. Then from the simulations shown in Fig. 3.17, we deduce $P = 0.37P_0 = 9.0$ mW. Note that this method is appropriate for an absolute measurement of P_0 , however, it is less recommended for the estimation of P since it relies on propagation simulations while the measurement at normal incidence described above is a direct one.

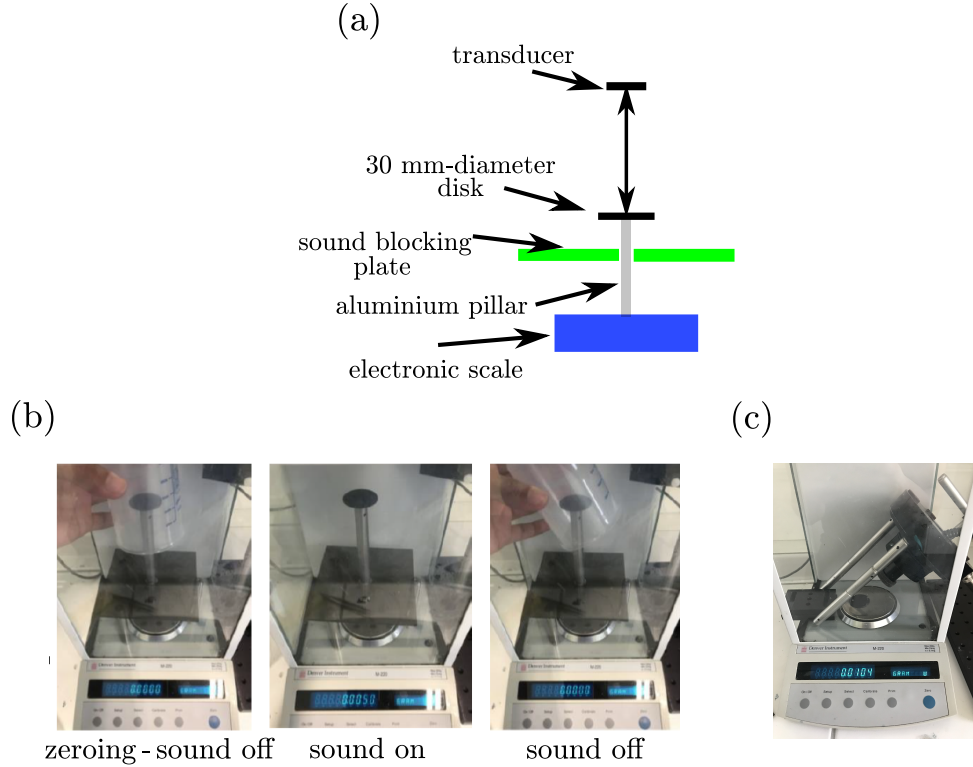


Figure 3.22: Experiment of radiation pressure at $d = 10$ mm for irradiation at normal incidence and 45° using a electronics scale. (a) Sketch of experiment. (b) Snapshots of the experimental measurements at normal incidence. (c) Photo of measurement at 45° .

3.8 Discussion of the power mismatch between theory and experiment

The discrepancy between the power P evaluated from the acoustic torque and force experiments calls for several comments. First, we note the possibility that the acoustic transducer emits power at frequencies other than 100 kHz is neither affecting the acoustic radiation force, which does not depend on the frequency, nor the acoustic radiation torque since the direct scaling $\Gamma \propto \omega^{-1}$ is compensated by the fact that $\ell \propto \lambda^{-1} \propto \omega$. Second, we recall that used expression $\Gamma = \ell P / \omega$ is only valid in the paraxial approximation while any helical mirror a priori does not behave in a paraxial manner in its center as the spiral slope angle $\beta(r) = \arctan[\ell h / (2\pi r)]$ diverges as $r \rightarrow 0$, r being the distance from the center. A quantitative estimation of its impact on the total torque exerted on an helical

mirror is obtained from the basics of the continuum mechanics, which gives

$$\Gamma = \frac{4\pi}{c} \int I(r) \sin \beta(r) \cos^2 \beta(r) r^2 dr \quad (3.8)$$

Here, accounting for the acoustic intensity profile given by the simulations, we obtain that the acoustic torque experiment gives up to $\sim 7\%$ underestimate of the power P with respect to the paraxial framework. Third, the non-ideality of the fabricated helical mirror, whose height is not independent on r in practice. For further discussion check chapter 2. Fourth, we note that the effect of the acoustic rotational streaming phenomenon, which corresponds here to the rotating airflow induced by the dissipation of the acoustic vortex beam in the air, can be safely neglected here since the main source of the viscous torque comes from the liquid due to a large contrast of viscosity ($\eta_{\text{liquid}}/\eta_{\text{air}} \sim 7 \times 10^2$).

These comments being said, we admit that do not have a definitive explanation for the observed acoustic power mismatch.

This study of the direct measurement of the transfer of angular momentum by non-dissipative vortex mode has been accepted in November 2019 for publication in Physical Review Letters journal with the title “Direct mechanical detection and measurement of wave-matter orbital angular momentum transfer by non-dissipative vortex mode conversion”.

Orbital acoustomechanics: a torsional pendulum experiment

In the previous chapter, helical mirrors have shown their effectiveness as non-dissipative acoustic elements for experimental study of the transfer of orbital angular momentum. This was done in the particular case of spinning experiments under constant irradiation. In this chapter we explore the situation of time-dependant excitation, with the aim at realizing a mechanical oscillator driven by orbital angular momentum transfer. For this purpose we choose a torsional pendulum framework, where the helical mirror is placed at the tip of a wire. Under constant irradiation, the torque exerted on the mirror twists the wire up to an angle at which the restoring elastic torque and the acoustic radiation torque are balanced. When periodic time-dependent irradiation is used, a resonant mechanical behaviour can be reached, and leads to an enhanced amplitude of the angular displacement with respect to the static case. Such a study is performed for various topological charges of the helical mirror. As discussed in the first chapter, torsional pendulum approaches have already been implemented in the earliest experiments of the dissipative transfer of orbital angular momentum of sound to matter [33, 34, 35]. However, in all cases, a discrete set of acoustic sources (namely, loudspeakers operating in the audible domain) emitting constant acoustic waves have been used. Therefore, the gain expected from a mechanical resonance has never been exploited so far. Our approach thus goes beyond every of the latter aspects, making it one of a kind. In this chapter we cover the design of the pendulum, the report of our first measurements both in the static and resonant cases, and improved design and instrumentation towards quantitative measurements of non-dissipative acoustic radiation torque.

4.1 Theoretical background: predictions

The torsional pendulum is modelled as a mass-less circular cross-section wire holding the helical mirror on which the torque is applied. The dynamics of the angular displacement of the torsional pendulum is modelled as a forced damped linear oscillator

$$J\ddot{\theta} + \gamma\dot{\theta} + \kappa\theta = \Gamma \quad (4.1)$$

where θ is the angular displacement (see Fig. 4.1), J is the moment of inertia of the helical mirror along the direction of the wire, $\gamma > 0$ is the damping coefficient, $\kappa > 0$ is the torsion constant and $\vec{\Gamma} = \Gamma\vec{z}$ is the external torque applied to the system. In the case of a static torque $\Gamma = \Gamma_{\text{stat}}$, the angular displacement is

$$\theta_{\text{stat}} = \frac{\Gamma_{\text{stat}}}{\kappa} \quad (4.2)$$

An estimate of the static angular displacement can be obtained from the knowledge acquired in the chapter 3. Indeed, κ is related to the natural frequency Ω_0 of the oscillator via the relationship $\Omega_0 = \sqrt{\kappa/J}$ and our acoustic source can deliver an acoustic torque of the order of 10 nNm, see Fig. 3.21(b). Therefore, taking for J a typical the value of our mirrors, namely, $J \sim 10^{-7} \text{ kg m}^3$, we can estimate θ_{stat} as a function of the resonance frequency. The results are shown in Fig. 4.2(a).

In the case of a biased harmonic external torque, $\Gamma(t) = \Gamma_{\text{stat}} + \Gamma_{\text{dyn}} \sin(\Omega t)$ where Ω is the modulation angular frequency and Γ_{dyn} corresponds to the amplitude of the modulated torque, the dynamics of the angular displacement is expressed as

$$\theta(t) = \theta_{\text{stat}} + \delta\theta(\tilde{\Omega}) \sin(\Omega t + \phi(\tilde{\Omega})) \quad (4.3)$$

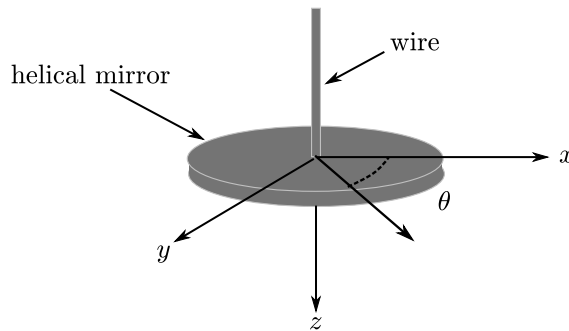


Figure 4.1: Diagram of a torque pendulum consisting on a wire holding an helical mirror. The axis orientation is oriented in the frame of reference of the helical mirror.

where we introduce the amplitude of the angular oscillation

$$\delta\theta(\tilde{\Omega}) = \frac{\Gamma_{\text{dyn}}}{J\Omega_0^2 \sqrt{(1 - \tilde{\Omega}^2)^2 + \left(\frac{\gamma}{J\Omega_0} \tilde{\Omega}\right)^2}} \quad (4.4)$$

and the reduced angular frequency $\tilde{\Omega} = \Omega/\Omega_0$, and the phase

$$\phi(\tilde{\Omega}) = \arctan \left[\frac{\gamma}{J\Omega_0} \left(\frac{1}{1 - \tilde{\Omega}^2} \right) \right] + \phi_0 \quad (4.5)$$

where ϕ_0 is a constant. The maximal angular displacement amplitude $\delta\theta_{\text{max}}$ is reached at the resonant angular frequency

$$\Omega_r = \Omega_0 \sqrt{1 - \frac{1}{2} \left(\frac{\gamma}{J\Omega_0} \right)^2} \quad (4.6)$$

In the limit $\left(\frac{\gamma}{J\Omega}\right)^2 \ll 1$, which is satisfied in our studies, $\Omega_r \approx \Omega_0$ and we have

$$\delta\theta_{\text{max}} = \frac{\Gamma_{\text{dyn}}}{\gamma\Omega_0} \quad (4.7)$$

An estimate of the expected value of $\delta\theta_{\text{max}}$ therefore implies the knowledge of the order of magnitude of the loss parameter γ . For a start, let us consider the viscous torque of a rotating disk, as discussed in chapter 3. This leads us to define, within the Stokes approximation and considering air as the external fluid around the moving disk, the following external loss contribution

$$\gamma_{\text{ext}} = (32/3)\eta R^3 \quad (4.8)$$

where $\eta = 2 \times 10^{-5}$ Pa s is the dynamics viscosity of air and R is the radius of the helical mirror. The validity of above equation implies that the inertial correction to the viscous torque can be neglected, namely, $\alpha\text{Re}^2 \ll 1$ with $\alpha \sim 10^{-3}$ according to Ovseenko [41] and $\alpha \sim 10^{-4}$ according to our investigation reported in chapter 3. To verify this assumption, we note that all our experiments are made for resonant oscillating frequency up to 100 Hz. This leads typically to αRe^2 values up to 1 in the worst case scenario. Therefore, there is no dramatic need for refining the Stokes framework in order to carry out a first evaluation of γ_{ext} .

Still, we note that there is another source of loss in our system. Indeed, the wire behaves as a viscoelastic medium whose losses cannot be neglected a priori. In order to ascertain the last statement, let us recall the experiment of the torsional

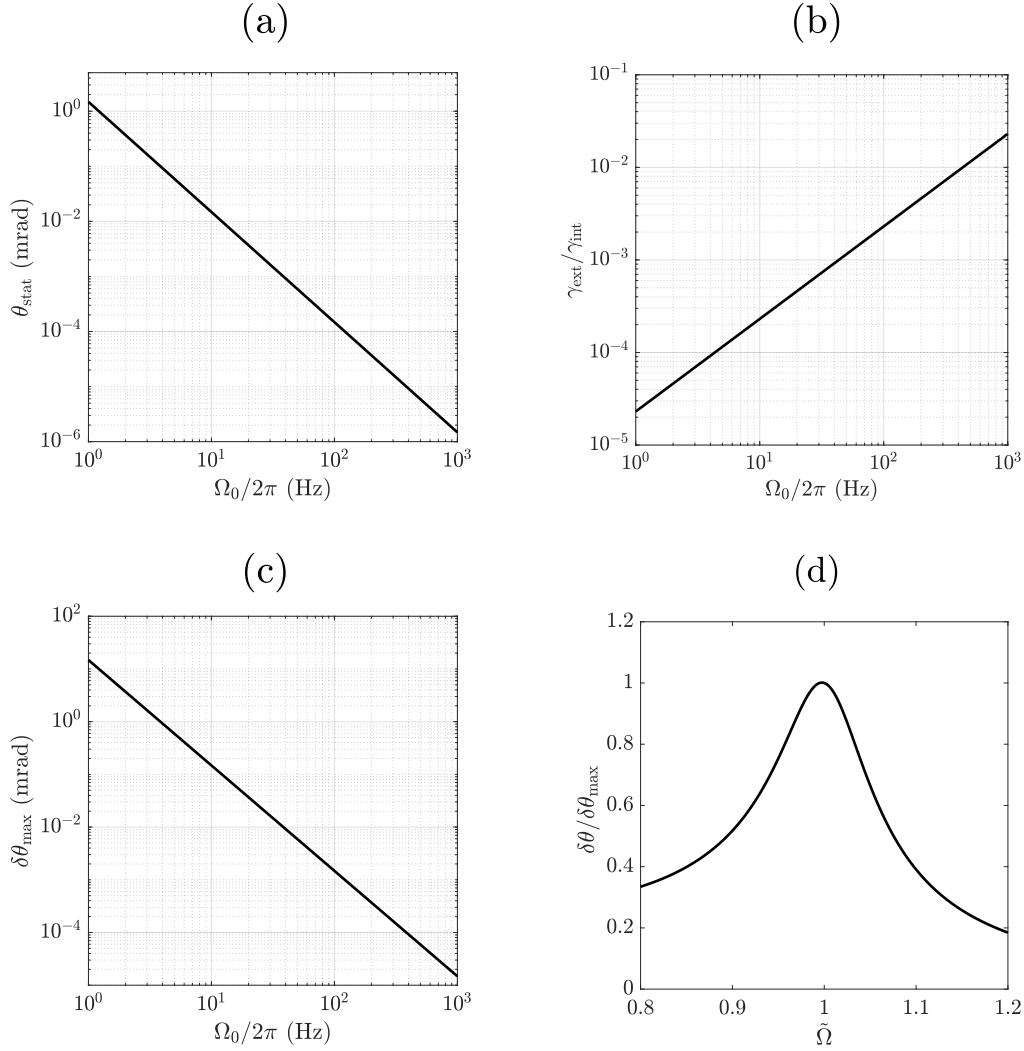


Figure 4.2: (a) Static angular momentum θ_{stat} as a function of the natural frequency of the oscillator. (b) Ratio $\gamma_{\text{ext}}/\gamma_{\text{int}}$ as a function of the natural frequency. (c) Maximum angular displacement at resonance as a function of the natural frequency. (d) Normalized resonance curves for the angular displacement. All these plots are calculated using the following typical parameter that illustrates well the situation we have experimentally explored: $G' = 1$ GPa, $G'' = 0.1$ GPa, $J = 10^{-7}$ Kg m³, $L_w = 50$ mm, $D_w = 1$ mm and $R = 15$ mm

constant of a cylindrical wire of length L_w and diameter D_w fixed at one end. It expresses as

$$\kappa = \frac{\pi D_w^4}{32 L_w} G \quad (4.9)$$

where G is the shear modulus. However, G is complex for a viscoelastic medium. Namely, $G = G' + iG''$ with $(G', G'') > 0$. Therefore, in Eq. (4.1) one has $\kappa =$

$\frac{\pi D_w^4}{32L_w}G' = \kappa'$, while an extra contribution adds to γ_{ext} according to $\gamma = \gamma_{\text{ext}} + \gamma_{\text{int}}$ with

$$\gamma_{\text{int}} = \frac{\kappa''}{\Omega} \quad (4.10)$$

Since for our resin material we have typically $G' \sim 1$ GPa and $G'' \sim 0.1$ GPa (these values are actually coming out from our measurements, as discussed later in this chapter) we can estimate the ratio between the external and internal contributions to the losses. This is summarized in Fig. 4.2(b) where $\gamma_{\text{ext}}/\gamma_{\text{int}}$ is plotted as a function of Ω_0 . It turns out that γ_{int} dominates over γ_{ext} in the range of frequency of interest, and therefore γ_{ext} is neglected in what follows.

As a result, we get

$$\delta\theta(\tilde{\Omega}) = \frac{G''}{G'} \delta\theta_{\text{max}} \left[(1 - \tilde{\Omega}^2)^2 + \left(\frac{G''}{G'} \right)^2 \right]^{-1/2} \quad (4.11)$$

with

$$\delta\theta_{\text{max}} = \frac{\Gamma_{\text{dyn}}}{\kappa''} \quad (4.12)$$

In Fig. 4.2(c) we plot $\delta\theta_{\text{max}}$ as a function of the resonance frequency for $\Gamma_{\text{dyn}} = 10$ nNm and the normalized resonance curve for the angular displacement angular displacement as is shown in Fig. 4.2(d).

4.2 Preliminary experiments

4.2.1 Definition of a pendulum design

It is clear from Figs. 4.2(a) and 4.2(c) that both static and dynamic angular displacement are favoured by small values of the natural frequency. Since our acoustic power supply specifications data sheet mentions minimal modulation frequency of 10 Hz, we prepared a first design for $F_0 = 10$ Hz, with $F_0 = \Omega_0/2\pi$. Also, we decided to work with a wire of length $L_w = 50$ mm and a base of height $H_B = 1$ mm and diameter $D_B = 30$ mm, on which the helical mirror is placed, see Fig. 4.3(a). The diameter of the wire is thus obtained from the expression $\Omega_0 = \sqrt{\kappa'/J}$ with $G' = 1$ GPa as a guess value of the shear modulus [43]. The value of resonance frequency as a function of the radius is illustrated in Fig. 4.3(b) and we choose $D_w = 1$ mm, which corresponds to a resonance frequency of 11.7 Hz.

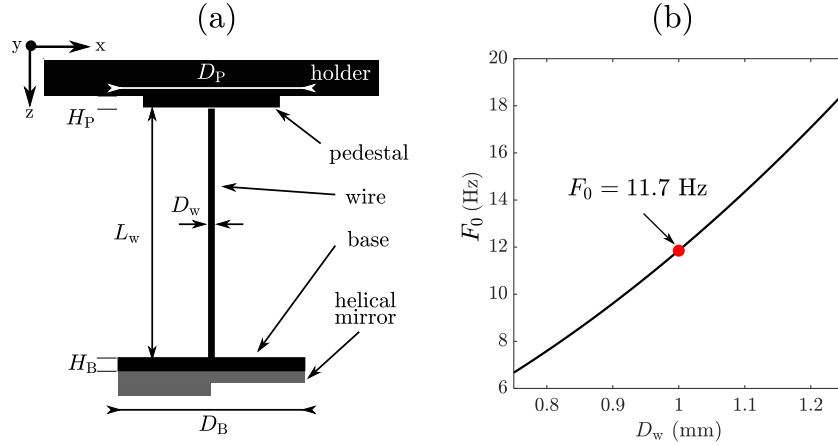


Figure 4.3: (a) Definition of the geometrical parameters of the torsional pendulum, constituted of three parts: a pedestal, a wire and a base. The helical mirror can be placed and removed on-demand at the bottom of the base using double-side tape. (b) Resonance frequency F_0 as a function of the diameter D_w for a wire of length $L_w = 50$ mm and taking moment of inertia $J = 10^{-7}$ kg m³ for the “base+mirror” system.

4.2.2 3D printing: design and fabrication

The initial design of the pendulum was thought as a monolithic “pedestal + wire” structure in order to keep the wire and the pedestal perpendicular to each other by construction, see Fig. 4.3(a). Also, we include a pedestal of height $H_P = 1$ mm and diameter $D_P = 25$ mm at the other end of the wire. By doing so, the pendulum can be easily fixed to a 6-axis mirror mount, which ensures fine tuning of the orientation and position of the pendulum. The modelling of the pedestal-wire and base structures are described as follows, see Fig. 4.4:

- (a) Using the function *cylinder*, we design the pedestal with height $H_P = 1$ mm and diameter $D_P = 25$ mm .
- (b) Using *cylinder*, we design the wire (red) with length $L'_w = 50.3$ mm and diameter $D_w = 1$ mm that is placed perpendicular to the disk surface of the pedestal and centered with it. Here, we choose $L'_w = L_w + 0.3$ mm because the wire will be inserted into the base, as detailed below.
- (c) A smooth transition from the pedestal to the wire is made in order to ease the merging of the pedestal and the wire at the moment of 3D printing. This is done by selecting the option *fillet edge* to generate a connector surface between the pedestal and the wire.

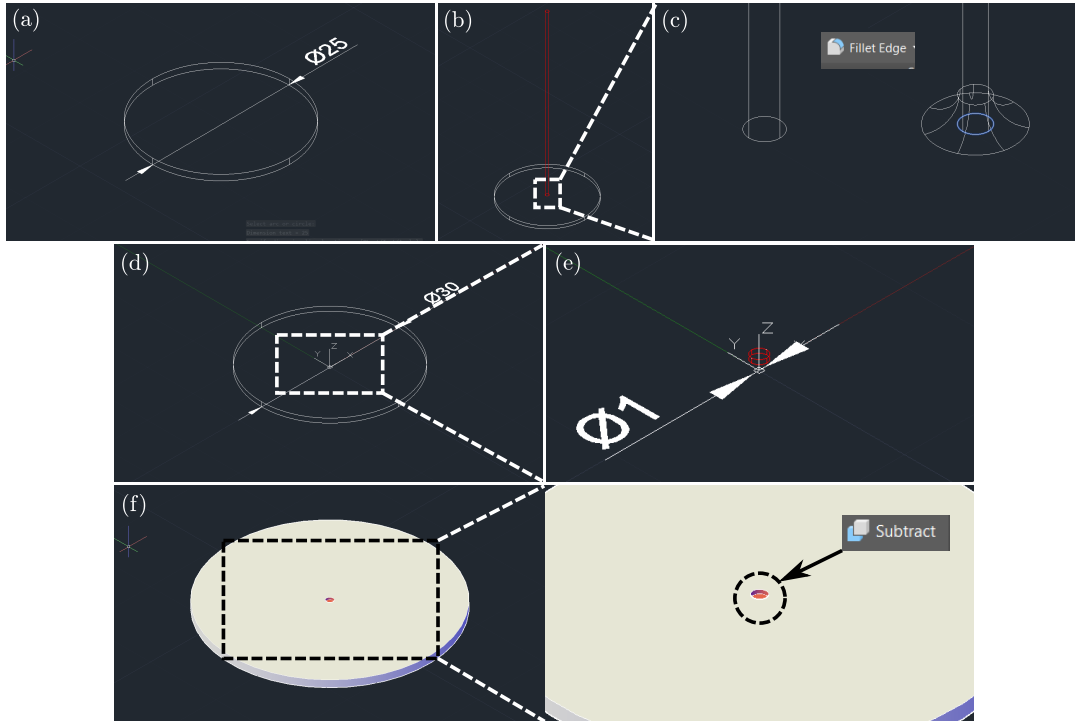


Figure 4.4: Design of pedestal-wire and base structures in AutoCAD. (a) Definition of the pedestal of height $H_P = 1$ mm and diameter $D_P = 25$ mm. (b) Placing the wire with length $L'_w = 50.3$ mm and diameter $D_w = 1$ mm at the center of the pedestal. (c) Connecting the surface of the pedestal with the wire. (d) Defining the base with height $H_B = 1$ mm and diameter $D_B = 30$ mm that corresponds to the diameter of the helical mirrors. (e) Preparing the base to host the wire of the pendulum, a small cylinder of 0.3 mm depth and 1 mm diameter is drawn inside the base. (f) Removing the part corresponding to the latter cylinder defines the hole.

- (d) The base is designed using *cylinder*, selecting a height $H_B = 1$ mm and a diameter $D_B = 30$ mm.
- (e) In order to prepare the junction of the pedestal-wire with the base, we design a hole with 1 mm diameter and 0.3 mm depth at the center of the base where will be inserted, and glued, the tip of the wire.
- (f) Using the function *subtract* and selecting the base and the latter cylinder placed at the center of the base, a hole is formed.

After the design of the pedestal-wire and the base, both objects were sent independently for 3D printing. These two items are connected according to the following process, see Fig. 4.5:

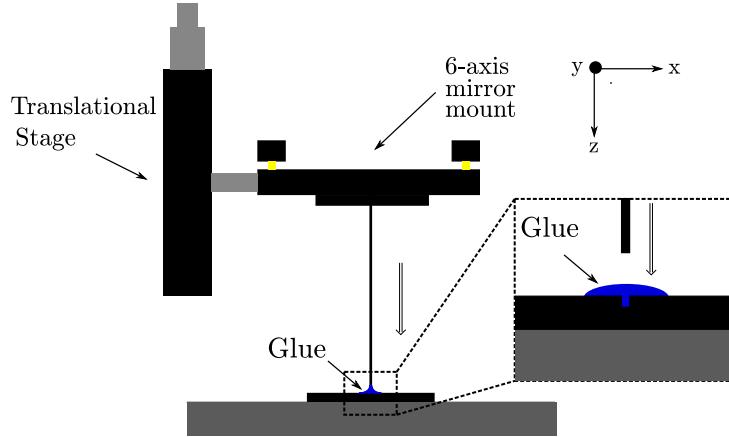


Figure 4.5: Connecting the pedestal-wire with the base. The pedestal-wire is held by a 6-axis mirror mount and translated towards the base with a translational stage. The wire is inserted into the hole of the base and permanently fixed owing to a droplet of glue.

- (a) First, the pedestal-wire item is fixed on a 6-axis mirror mount, with the wire perpendicular to the plane of the experimental table. The mirror mount is fixed to a vertical translation stage ensuring controlled displacement along the z axis.
- (b) The base is placed on the experimental table with the hole facing to the wire. With the 6-axis mirror mount, the wire is aligned with the center of the hole.
- (c) A droplet of glue is placed inside the hole and then we insert the wire into the hole by applying a small force onto the base with the wire. We wait for 5 min. The pendulum structure is ready, yet being fragile. The structure must be further handled with care since it easily breaks if dropped or held from the wire (experienced unfortunate situation!)

4.2.3 Experimental setup

The torsional pendulum is finalized by fixing a helical mirror at the bottom of the base. This is done by placing double-side tape on the flat side of the helical mirror and pressing it with care on the base, paying attention to centering, which is made visually. The transfer of angular momentum upon irradiation of the helical mirror induces an acoustic torque exerted on the pendulum, making it to twist by an angle θ with respect to its initial position that defines the origin, $\theta = 0$.

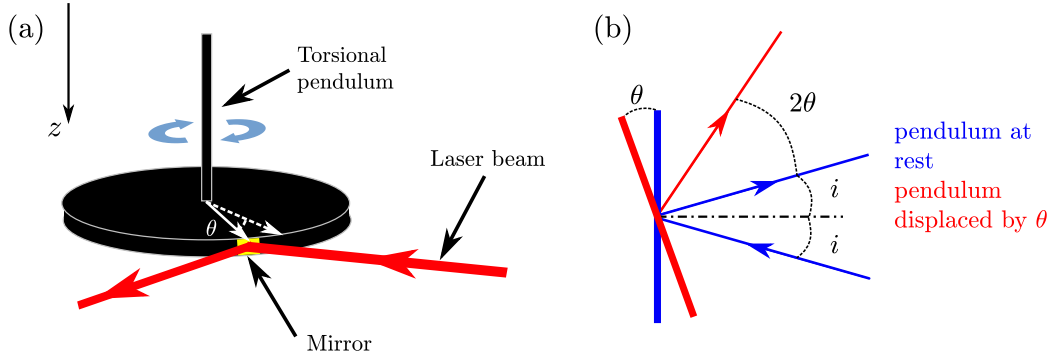


Figure 4.6: (a) Sketch of a laser beam reflected from a small mirror attached to the side of the pendulum. (b) The laser beam impinges onto the mirror attached to the pendulum in the plane of the base, at an angle i with respect to the normal of the mirror (blue). The rotation of the pendulum by an angle θ leads to a deflection of the laser beam by an angle 2θ (red).

To measure this angle of rotation, we attach a small mirror on the side of the base of the pendulum, whose position is monitored by analysing the reflection of a beam impinging onto the mirror, see Fig. 4.6. The mirror is made by breaking a coverslip with $\sim 100 \mu\text{m}$ thickness coated by a 200 nm thick gold layer. A broken part with a few mm^2 area is used as the mirror. As the pendulum is rotated by an angle θ , the reflected beam is deflected by an angle 2θ , see Fig. 4.6(b). In practice, we use a He-Ne laser operating at 633 nm wavelength and focused by a lens L_1 with focal length $f_1 = 50 \text{ cm}$, see Fig 4.7(a). The focal plane is adjusted to coincide with the plane of the mirror. The diameter of the beam on the mirror is 0.5 mm and the small values of deflection angles (of the order of 1 mrad) prevent alignment drawbacks possibly associated with too large angular deviation of the pendulum.

The detection setup is shown in Fig. 4.7(a). The idea is to directly image the position of the reflected beam with a camera placed at the focal plane of a second lens L_2 having a focal length $f_2 = 1 \text{ m}$. The image of the beam spot in the plane of the camera is shown in Fig. 4.7(a). Since the displacement along the x -axis is $2\theta f_2$, a vivid direct visualization of the angular displacement θ implies to choose a situation for which the beam waist diameter $2w$ is at least of the order of $2\theta f_2$. Practically, this means to place L_2 at a large enough distance r from the mirror, keeping in mind the beam diameter D_2 in the plane of L_2 should be smaller than the lens diameter in order to prevent “beam clipping” that would alter the image of the beamspot detected by the camera. We found that $r \sim 6 \text{ m}$, for which

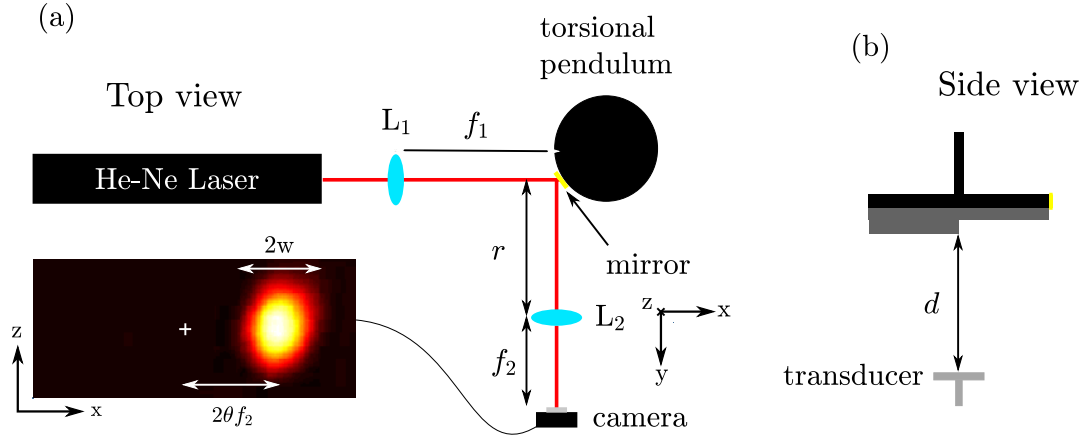


Figure 4.7: (a) Top-view sketch of the experimental setup to detect the mechanical consequence of the acoustic torque exerted on the pendulum. A He-Ne laser beam is focused with a lens L_1 with $f_1 = 500$ mm focal length to a small mirror fixed on the side of the base of the pendulum. The reflected beam propagates over a distance r from the mirror and reach the lens L_2 . The displacement of the laser beam is detected with a camera placed at a distance f_2 from L_2 . The lateral displacement of the laser spot of $2w$ diameter corresponds to $2\theta f_2$ (b) Side-view of the pendulum placed at a distance d and aligned with the acoustic source.

$D_2 \simeq 25$ mm, is a good trade-off that led us to choose a lens L_2 with 2 inches diameter.

4.2.4 First observations

In this section we report on the experimental demonstration of the mechanical detection of orbital angular momentum transfer. This is done by using a helical mirror with $\ell = 4$, placing the acoustic source at a distance $d = 15$ mm from it, see Fig. 4.7(b), setting the acoustic power at a value $\tilde{P}_0 = 5$. At rest (acoustic source “off” using an acoustic beam block) the location of the beam spot observed with the camera defines the origin of the lateral displacement $x = 0$, see Fig. 4.8(a). When the acoustic source is “on” at constant power, we observe a beam spot displacement $x_{\text{stat}} \sim 20 \mu\text{m}$, see Fig. 4.8(b). Then, we extend our observation to the case of a time-varying acoustic power. This is done by external electrical driving of the transducer power supply using a function generator set to a sinusoidal signal with frequency F and peak-to-peak amplitude of $2 V_{\text{pp}}$. As expected, δx strongly depends on F . The resonance is manually searched around the target value of 10 Hz. A maximal displacement $\delta x_{\text{max}} \sim 150 \mu\text{m}$ is found at $F_0 = 13.9$ Hz, see Fig. 4.8(c) that displays the normalized superposition

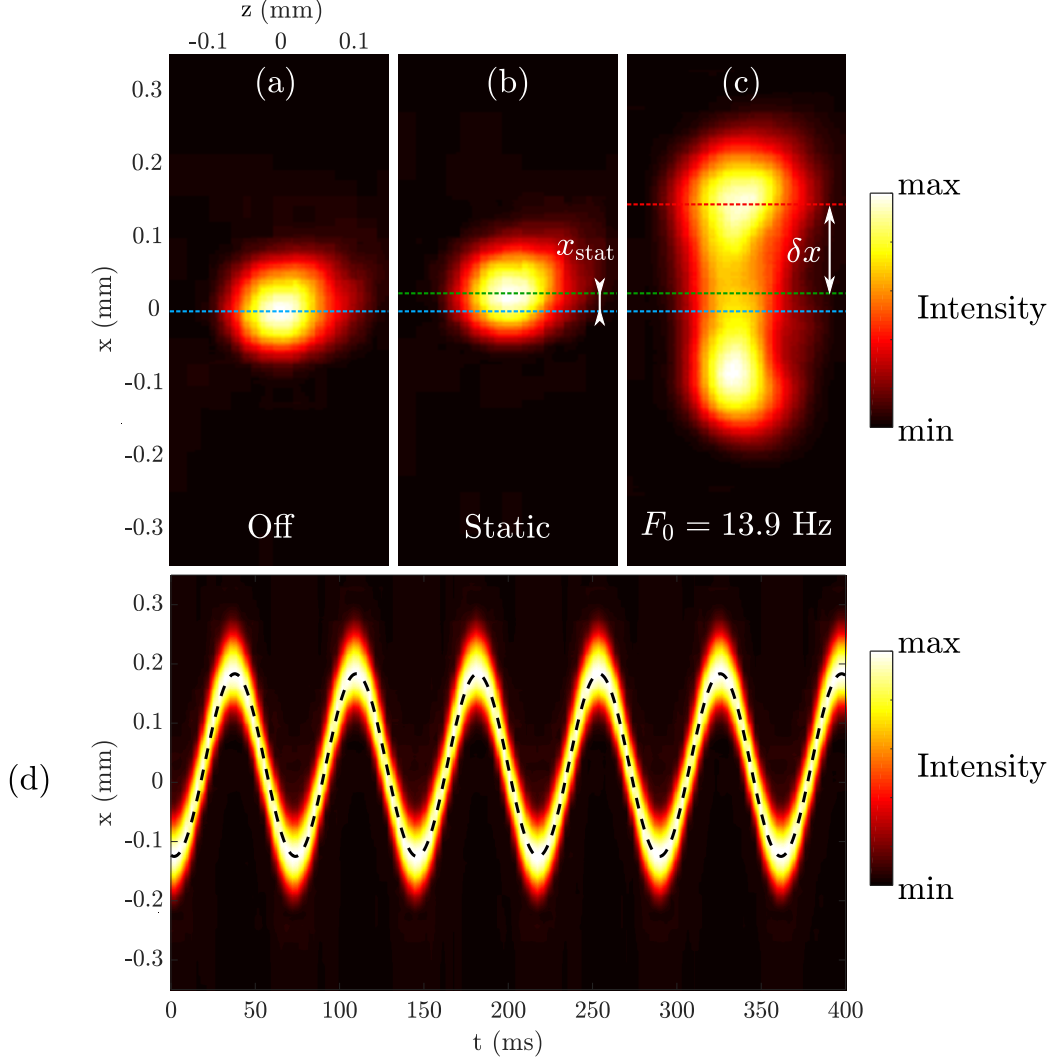


Figure 4.8: Image of position of laser beam spot detected by the camera. (a) Position of the laser beam spot when the acoustic source is blocked (off). (b) The laser beam presents a slight displacement when the source is unblocked (on). (c) Superposition of normalized images of lateral displacement of power source modulated in time. (d) Time resolve displacement of each frame with adjusted sinusoidal curve respect to maximum intensity values.

of all the images of a video recording of 30 s duration and 300 frames per second. The time-resolved displacement is shown in Fig. 4.8(d), where each frame of the video is transformed into a vector by summing the data of an image along the z coordinate. Then, the points of maximum intensity of the latter spatio-temporal dynamics are adjusted according to $\delta x(t) = x_{\text{stat}} + \delta x_{\text{max}} \sin(2\pi Ft + \phi)$ using x_{stat} , δx_{max} , F and ϕ as adjustable parameters. We obtain $x_{\text{stat}} = 29 \mu\text{m}$, $\delta x_{\text{max}} = 154$

μm and $F_0 = 13.9$ Hz, which equal the modulation frequency, as expected. Also, we note that the latter value is close to the guess value $F_0 = 11.7$ Hz inferred from our preliminary estimation, see section 4.2.1.

4.2.5 Quantitative analysis: setup and acquisition

In order to assess quantitatively the observed mechanical resonance, we need to detect and measure the angular displacement of the pendulum as a function of the frequency. This is done by sweeping the frequency between 1 and 30 Hz over a time duration of one hour. Here, the experiment is made using a helical mirror with $\ell = 2$, using the distance $d = 25$ mm (at which we learnt from chapter 3 that the acoustic torque does not vary substantially with small deviations from the nominal distance value) and setting $\tilde{P}_0 = 6.5$. The use of the camera for this purpose implies a huge amount of data to process, as well as possible drawback associated to tiny displacements due to the size of the pixel. To solve these issues, we use a PDP90A lateral effect position sensor (Thorlabs) instead of the camera. The sensor is a squared four-electrode light-controlled variable resistor. The x and y positions of the laser beam impinging on the sensor are determined proportionally to the distributed photocurrent generated at each electrode. Such sensor is independent of the beam shape and can resolve a minimal displacement of $0.75 \mu\text{m}$ at a 635 nm wavelength. The recommended spot size in the plane of the sensor is between 0.2 mm and 7 mm diameter. The sensor is connected to a KPA101 cube (Thorlabs), which is a motion controller that collects the values of the voltage associated to the x and y positions, and total voltage, respectively called XDIF, YDIF and SUM. In this experiment, we focus our attention to the output values of XDIF since the system is aligned in a way that the beam oscillates along the x axis. With the help of a data acquisition system (DAQ) connected to the KPA101 via a BNC cable, we extract and process the analogue signal of voltage as a digital signal giving the value of x .

The angular displacement of the pendulum is retrieved from $\theta = \frac{x}{2D_1}$ where D_1 is the distance at which the pendulum is placed from the sensor. The experimental setup is shown in Fig. 4.9. Note that we do not rely any more on the use of a lens after the reflection of light on the mirror fixed on the pendulum. We use $D_1 \sim 78$ cm, which corresponds to a distance at which the motion of the laser beam is kept in the working area of the sensor, while ensuring a beam diameter

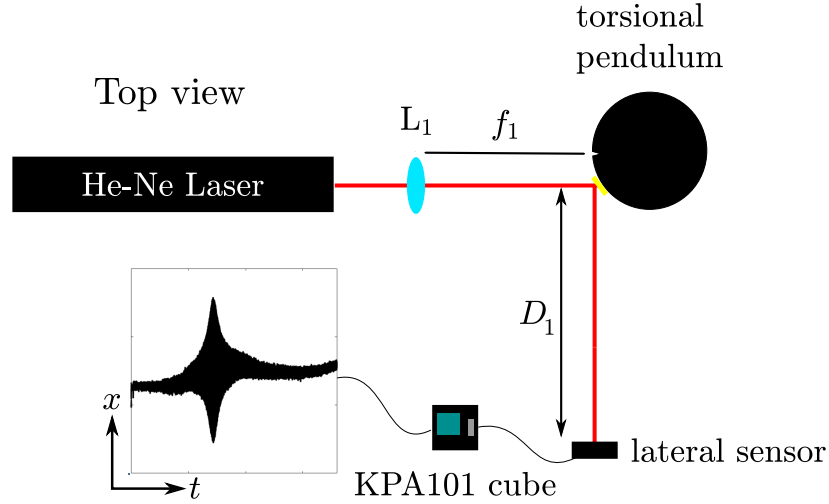


Figure 4.9: Experimental setup for the first measurement of the lateral displacement of the reflected laser beam.

that falls in the recommended range.

4.2.6 Data extraction and preliminary analysis

The experiment described in the previous section is performed four times in order to obtain a robust data set for quantitative analysis. The typical temporal trace $x(t)$ resulting from sweeping experiments is illustrated in the inset of Fig. 4.10(a). The angular displacement amplitude of the oscillation $\delta\theta$ is extracted by the method of wavelet transform. This approach allows to access to the temporal spectrum of the signal as a function of time. In Fig. 4.10(b) we show a temporal window of 300 s duration around the time that corresponds to the resonant frequency $F_0 = 12.25$ Hz of the pendulum. Noteworthy, the angular displacement is not symmetrical with respect to the origin of the oscillation, see label θ_i and red dashed line in Fig. 4.10(a). Indeed, the time trace exhibits a shift of the angular mean position as the driving frequency increases that eventually reach the value of θ_f , see blue dashed line in 4.10(a). This could be explained either by a uncontrolled misalignment of the base of the pendulum during the experiment or a systematic frequency-dependent mean power of the acoustic source that increases with time (that is to say, with the modulation frequency F). Also, in Fig. 4.10(c), we observe the presence of an artefact around 5 Hz whose origin is not properly understood. Finally, in Fig. 4.10(c), we show the experimental

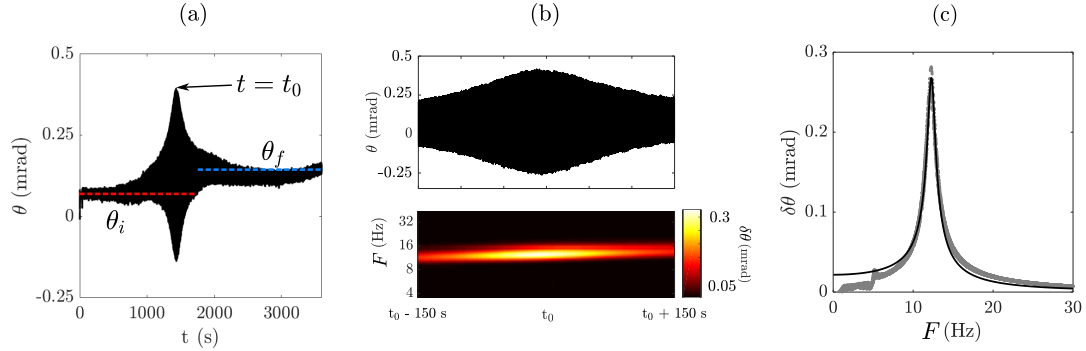


Figure 4.10: (a) Measurement of angular displacement as a function of time during the sweeping frequency experiment for $\ell = 2$, $\tilde{P}_0 = 6.5$ and $d = 25$ mm. (b) Angular displacement dynamics and its wavelet transform counterpart in an interval of 300 s centered on the time t_0 corresponding to the resonance frequency. (c) Reconstructed amplitude of the angular deviation of the driven pendulum (thick gray) and best-fit from the harmonic linear oscillation model (thin curve).

values of $\delta\theta$ as a function of the frequency, which reveals the lineshape of the resonance. The latter curve is adjusted using Eq. (4.11), which gives a fair validation of the description of the system as a linear forced harmonic oscillator. More precisely, the latter fit involves 3 adjustable parameters, namely, $\delta\theta$, G' and G'' (noting that $F_0 = 1/2\pi\sqrt{\kappa'/J}$ is a function of G' only since J is known) which gives $G' = 1.13$ GPa and $G'' = 0.092$ GPa. Still, the tails of the resonance curve are not nicely described, which invites us to check quantitatively the proper use of the wavelet transform technique, and the hypothesis of a frequency-dependent acoustic power. This is the purpose of the next section.

4.3 Towards quantitative experiments

4.3.1 Improved data processing

So far, the file format used to save the data is *.csv*, for which the data is distributed in columns and separated by commas. Such file is converted as a *.mat* file to be used in MATLAB. The inconvenience of *.csv* files is the size of the files reaching up to 1 Gb each, which is found to be a serious drawback for loading the files efficiently. Therefore, we eventually changed it and we further use instead *.tdms* file format, which suits the software LabVIEW that saves the information

in a binary format, which reduces the size of the files by a factor ~ 10 .

4.3.2 Benchmarking the modulated source: model

Here we discuss how the data acquired by the position sensor is processed by wavelet transform method. In order to benchmark the methodology of amplitude extraction via wavelet transform, we consider a signal mimicking the pressure field generated by the source that is linearly modulated both in frequency and amplitude according to

$$s(t) = \left[1 + A(t) \cos(2\pi F(t)t)\right] \cos(2\pi ft) \quad (4.13)$$

where

$$A(t) = \frac{A}{T_{\text{sweep}}}t \quad (4.14)$$

where A is a constant, f is the carrier frequency of the signal and

$$F(t) = f_1 + \frac{f_2 - f_1}{T_{\text{sweep}}}t \quad (4.15)$$

is the swept frequency where f_1 and f_2 correspond to the initial and final frequency of the sweeping process whose time duration is T_{sweep} . Then we recall that

- i) The acoustic intensity is proportional to the mean square of the pressure field.
- ii) The acoustic torque is proportional to the acoustic power.
- iii) The angular displacement is driven by the acoustic power.

Therefore, we are interested in monitor the mean square quantity $\langle s^2(t) \rangle_T$ evaluated over a time window with duration T over which both the relative variation of the modulation amplitude $A(t)$ and the phase $2\pi F(t)t$ can be neglected. This is ideally implies $1/f \ll T \ll T_{\text{sweep}}$, which gives

$$\begin{aligned} \langle s^2(t) \rangle_T &= \langle [1 + A(t) \cos(2\pi F(t)t)]^2 \cos^2(2\pi ft) \rangle_T \\ &\simeq \frac{1}{2} \left(1 + \frac{A^2(t)}{2}\right) + A(t) \cos(2\pi F(t)t) + \frac{A^2(t)}{4} \cos(4\pi F(t)t) \end{aligned} \quad (4.16)$$

We can see from Eq. (4.16) that such signal is the sum of 3 harmonic contributions at zero, $F(t)$ and $2F(t)$ frequencies.

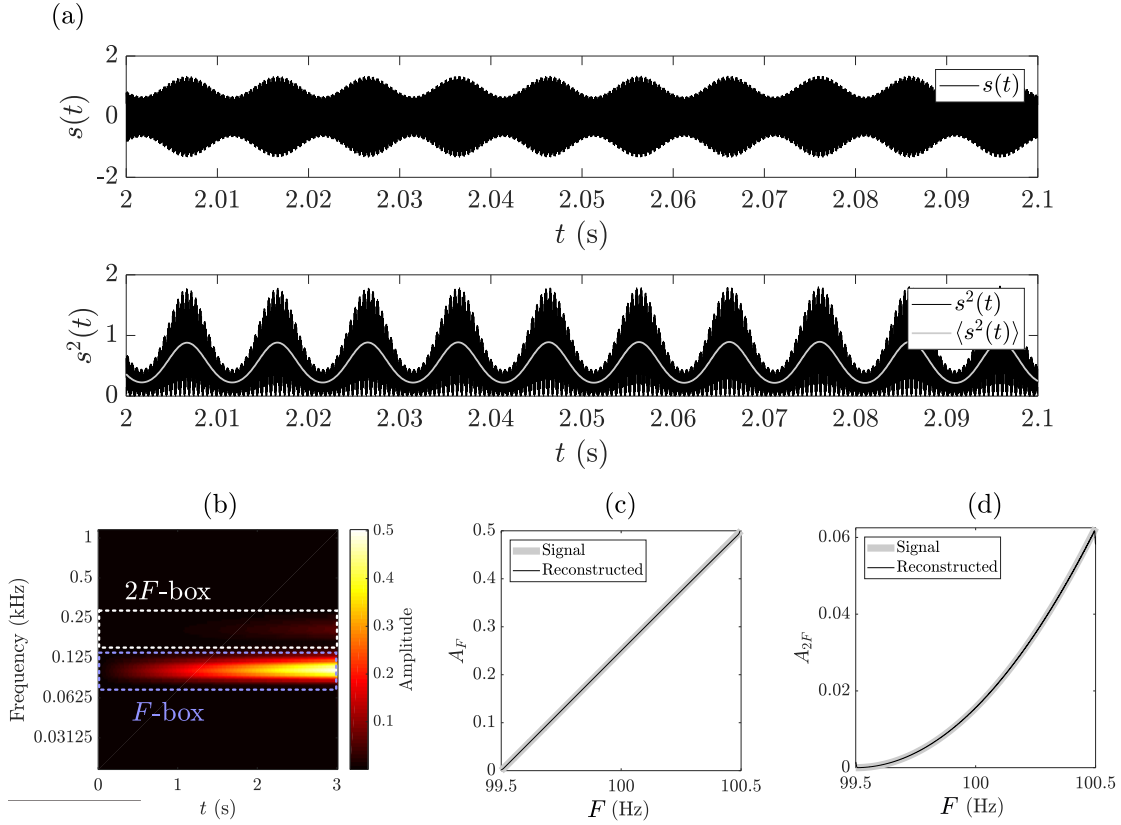


Figure 4.11: (a) Input signals $s(t)$, $s^2(t)$ and $\langle s^2(t) \rangle_T$ in the interval $2 \text{ s} < t < 2.1 \text{ s}$. (b) Wavelet transform of $\langle s^2(t) \rangle_T$. The white and blue dotted boxes correspond to the regions from which the values of A_F and A_{2F} are extracted by looking at the local maxima at each time t . (c,d) Reconstructed signal of A_F and A_{2F} as a function of the frequency (thick gray curve), which are compared to the input signal characteristics (thin dark curves).

In order to be as close as possible to the experimental characterization presented in the next subsection, we examine a signal with $A = 0.5$, $f = 100 \text{ kHz}$, $f_1 = 99.5 \text{ Hz}$, $f_2 = 100.5 \text{ Hz}$, $T_{\text{sweep}} = 3 \text{ s}$, and $T = 1 \text{ ms}$, which satisfy the double inequality mentioned above. Moreover we account for the inherent under sampling of the signal due to the DAQ system. Namely, we use a sampling frequency $f_s = 46 \text{ kHz}$. For the sake of illustration we display in Fig. 4.11(a) $s(t)$, $s^2(t)$ and $\langle s^2(t) \rangle_T$ on the interval $2 \text{ s} < t < 2.1 \text{ s}$. In Fig. 4.11(b), we present the full wavelet transform of $\langle s^2(t) \rangle_T$ where we emphasize two “boxes” labelled “ F -box” and “ $2F$ -box” from which we extract the amplitude A_F and A_{2F} associated to the harmonics F and $2F$ of Eq. (4.16). These amplitudes are compared with the expected values $A_F = A$ and $A_{2F} = A^2/4$. The reconstructed time-dependante amplitudes

A_F and A_{2F} obtained from the wavelet transform present a good agreement with respect to the original signal, indicating that the method of amplitude extraction via wavelet transform is trustworthy, see Fig 4.11(c,d). The method of wavelet transform will be used hereafter for extracting the amplitude of the signal of the lateral displacement sensor associated to the angular displacement of the pendulum.

4.3.3 Benchmarking the modulated source: experiment

The quantitative characterization of the modulated power source is made by replacing the pendulum by a piezoelectric sensor. As done in the experiment made to determine the warming-up time of the acoustic source (see chapter 2), the piezoelectric sensor is placed at a distance that corresponds to a maximal pressure field. The power source is set at $\tilde{P}_0 = 5.0$, and the function generator is set to deliver a sinusoidal wavefront with an amplitude of $2 V_{pp}$, and we sweep the frequency from 1 to 200 Hz in 10 min and we repeat the experiment six times in a row, see Fig. 4.12(a). The frequency sweep corresponding to the first 600 s of experiment is used as a reference to identify precisely the starting point of the sweeping in the next five experiments since the change in the amplitude of modulation at the transition between the 200 Hz and 1 Hz is well defined.

The output signal from the piezoelectric sensor is extracted with a DAQ system and in order to minimize the occurrence of artefacts due to signal under-sampling, the data is extracted with a sampling frequency that is not a multiple integer of the carrier frequency of the source. Specifically, we choose a sampling frequency $f_s = 46$ kHz. The value of the acoustic pressure p is associated with the voltage signal V delivered by the piezoelectric sensor. Since the acoustic intensity is proportional to $\langle p^2 \rangle$, the value $\langle V^2 \rangle$ is proportional to the acoustic power intercepted by the sensor.

The experiment consists to quantify how much is varying the amplitude of the modulated power of the source as a function of the modulation frequency F . In other words, by writing the modulated pressure field at frequency F as

$$p_{\text{mod}}(t) = p_0(1 + \epsilon \cos(2\pi F(t)t) \cos(2\pi ft)) \quad (4.17)$$

where p_0 is a constant and ϵ is the amplitude modulation depth ($0 < \epsilon < 1$), we aim at measuring ϵ . This is done by analysing the mean square of the voltage

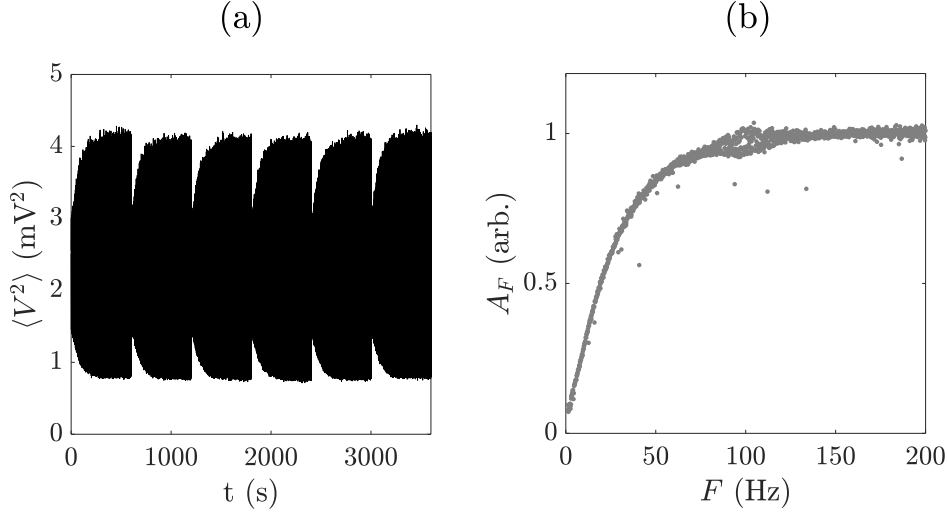


Figure 4.12: (a) Mean square values of the voltage delivered by the piezoelectric sensor for 6 consecutive frequency sweeping experiments over 1 hour. Only the five last sweeping sequences are used for data processing. (b) Value of A_F extracted from the experiment.

measured from the piezoelectric sensor, namely, $\langle V_{\text{mod}}^2(t) \rangle_T \propto \langle p_{\text{mod}}^2(t) \rangle_T$ using a time window $T = 1$ ms. Since we have

$$\begin{aligned} \langle V_{\text{mod}}^2(t) \rangle_T &= A_0 + A_F \cos(2\pi F(t)t) + A_{2F} \cos(4\pi F(t)t) \\ &\propto \frac{1}{2} \left(1 + \frac{\epsilon^2}{2} \right) + \epsilon \cos(2\pi F(t)t) + \frac{\epsilon^2}{2} \cos(4\pi F(t)t) \quad (4.18) \end{aligned}$$

the amplitude of the harmonic contribution at frequency F , A_F , is proportional to ϵ and is measured by wavelet transform processing. The results are shown in Fig. 4.12(b). It appears that the modulation depth depends on the modulation frequency at $F < 50$ Hz, which offers a decent explanation for the imperfect quantitative description of the resonance lineshape for the pendulum with resonant frequency around 10 Hz shown in Fig. 4.10. This invites to design a second generation of pendulum allowing the use of the linear oscillator model driven at constant modulation depth in order to extract quantitative information on the acoustic radiation torque.

4.3.4 Optimal pendulum design

Recalling that angular displacements are larger for small values of the resonance frequency, a trade-off is necessary with the aim at working at constant modulation depth. Therefore, we opt for a target resonance frequency $F_0 = 100$ Hz. From

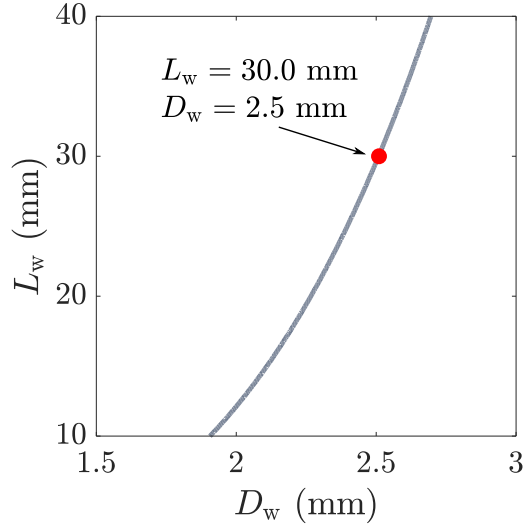


Figure 4.13: Values of L_w and D_w of wire corresponding to a resonance frequency $F_0 = 100$ Hz, taking $G' = 1.13$ GPa and $G'' = 0.092$ GPa

the knowledge of G' inferred from the first generation of pendulum, we define the set of wire parameters (L_w, D_w) that gives $F_0 = 100$ Hz. This is shown in Fig. 4.13, from which we choose $L_w = 30$ mm and $D_w = 2.5$ mm.

In addition, we explore the role of the thickness of the polymerized layer of the 3D printing process. Namely, we compare the behaviour of two pendulums with thickness layer of $10 \mu\text{m}$ and $50 \mu\text{m}$. The experiment is performed at a distance of $d = 25$ mm using a helical mirror with $\ell = 2$, power $\tilde{P}_0 = 5$ and modulation amplitude of the function generator of $2 V_{pp}$. The experimental results are shown in Fig. 4.14, where best fit are also presented. At first, we note that chosen design actually gives $F_0 \sim 100$ Hz as expected. Also, we find $(G', G'') = (1.05 \text{ GPa}, 80 \text{ MPa})$ for $10 \mu\text{m}$ layer and $(0.90 \text{ GPa}, 85 \text{ MPa})$ for $50 \mu\text{m}$ layer. These values are consistent with qualitative expectations. Indeed, on the one hand, thinner 3D printed layers implies deeper photopolymerization process leading to stiffer behaviour, hence $G'(10 \mu\text{m}) > G'(50 \mu\text{m})$. On the other hand, less polymerized layers are expected to provide larger viscous losses, hence $G''(50 \mu\text{m}) > G''(10 \mu\text{m})$. Of course, without a more systematic study, we cannot draw a definitive statement and we stress that above comment remains at the qualitative level. Anyway, the observed variations are not game-changing and we eventually choose a printing layer thickness of $10 \mu\text{m}$ for the final set of experiments that are described in the next section.

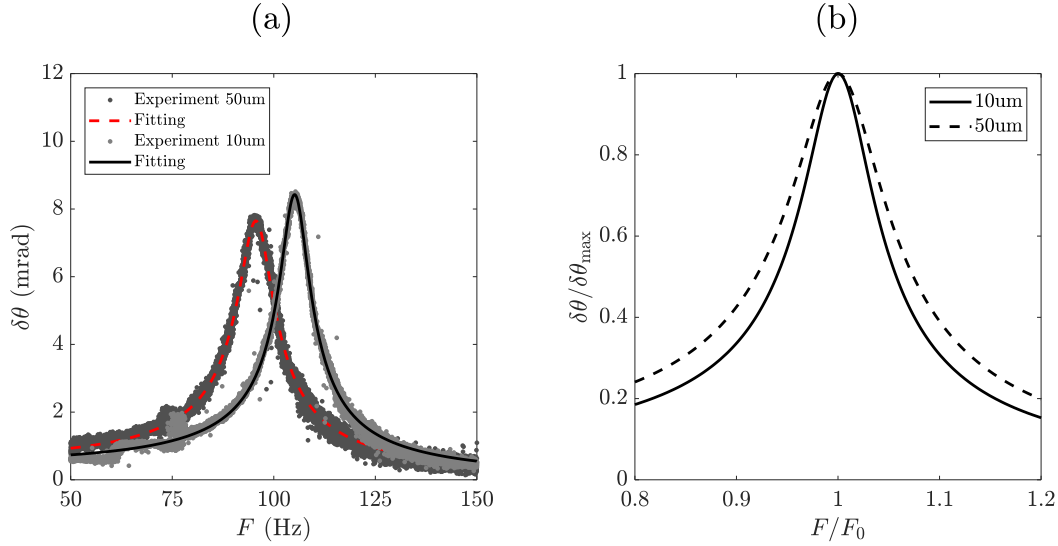


Figure 4.14: (a) Experimental results and fitting curves of the resonant behaviour for pendulum with 50 μm and 10 μm 3D printed thickness layer. (b) Normalized fitted curves. The experiments are performed at a distance of $d = 25$ mm using a helical mirror with $\ell = 2$, power $\tilde{P}_0 = 5$ and modulation amplitude of the function generator of 2 V_{pp}

4.4 Acoustic torque measurements

Helical mirrors with $1 \leq \ell \leq 4$ have been analysed. A set of five independent experiments are performed for each of them, for $d = 25$ mm and $d = 100$ mm. By doing so, we offer the possibility to compare obtained results with those of chapter 3. In all cases, the experiments are performed at $\tilde{P}_0 = 5.0$ and 2 V_{pp} for amplitude modulation. The frequency sweeping is now restricted to the interval of $80 \text{ Hz} < F < 120 \text{ Hz}$. In all the experiments, the lateral displacement sensor is placed at a propagation distance of 6.15 m from the pendulum. The latter value differs from that used for the pendulum with $F_0 \sim 10$ Hz because the latter one provided larger angular displacement, which required to place the sensor closer to the mirror in order to prevent the oscillating beam spot to fall outside the sensor area. The results are summarized in Fig. 4.15. In all cases, a good reproducibility is obtained as demonstrated by the fact that the lineshape of the resonance is clearly observed even though 5 independent experiments are superimposed. We attribute the presence of a few spurious dots in each figure to unavoidable environmental noise of the lab. Each experiment is fitted with Eq. (4.11), using $\delta\theta_{\max}$, G' and G'' as adjustable parameters according to the equation

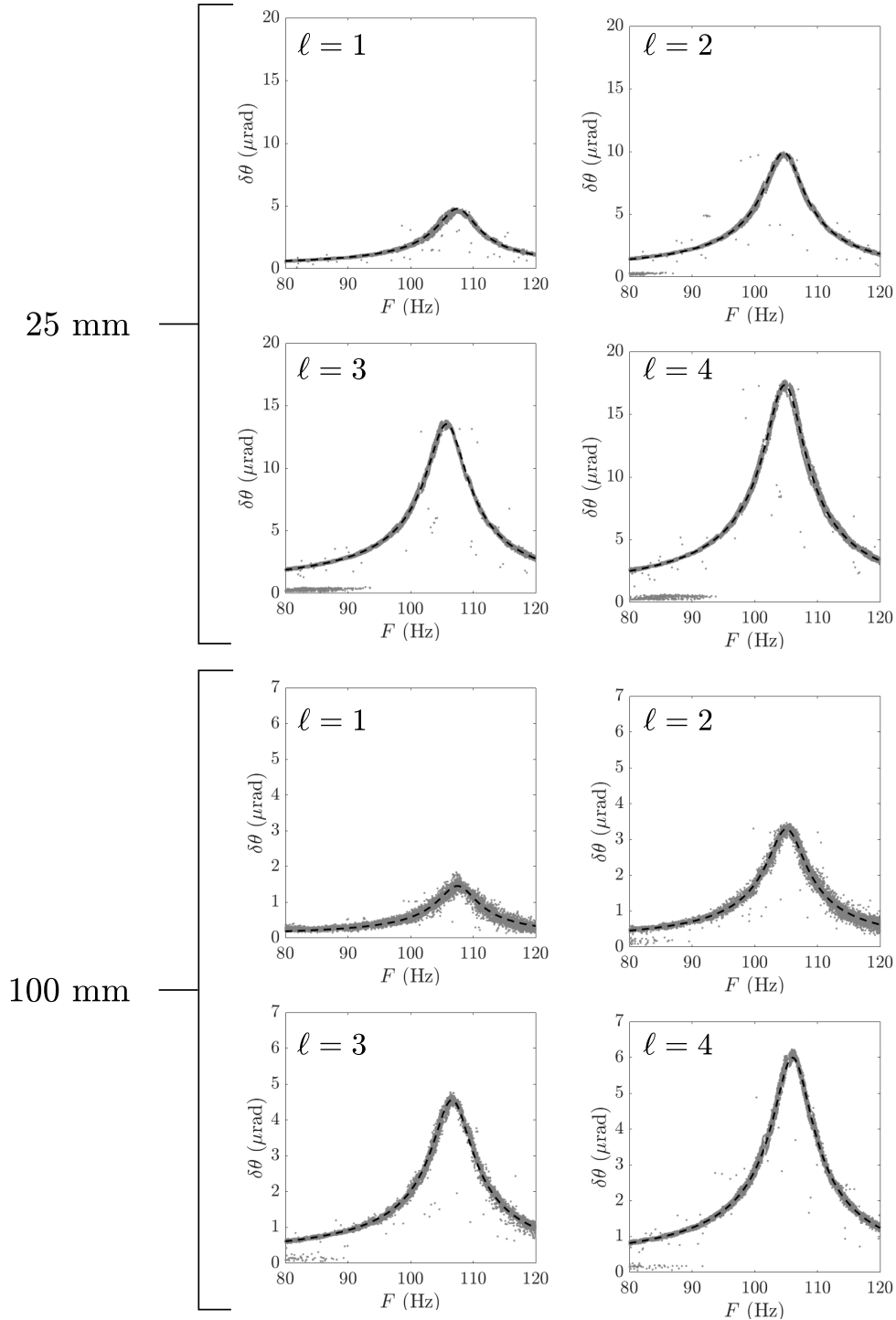


Figure 4.15: Experimental results for helical mirrors with charge $1 \leq \ell \leq 4$ for five independent frequency-sweeping experiments both for $d = 25$ mm and $d = 100$ mm. Other parameters for the experiment are given in the test

$$\delta\theta = \frac{G''/G'}{\sqrt{(1 - (F/F_0)^2)^2 + (G''/G')^2}} \delta\theta_{\max} \quad (4.19)$$

where $F_0 = \frac{1}{2\pi} \sqrt{\kappa'/J}$, using the measured value of J for every of the used helical mirror. The results are summarized in Fig. 4.16. In both cases, $d = 25$ mm and $d = 100$ mm, the angular displacement exhibits a linear behaviour versus ℓ , as expected. Also, both G' and G'' are almost constant on all cases, as expected.

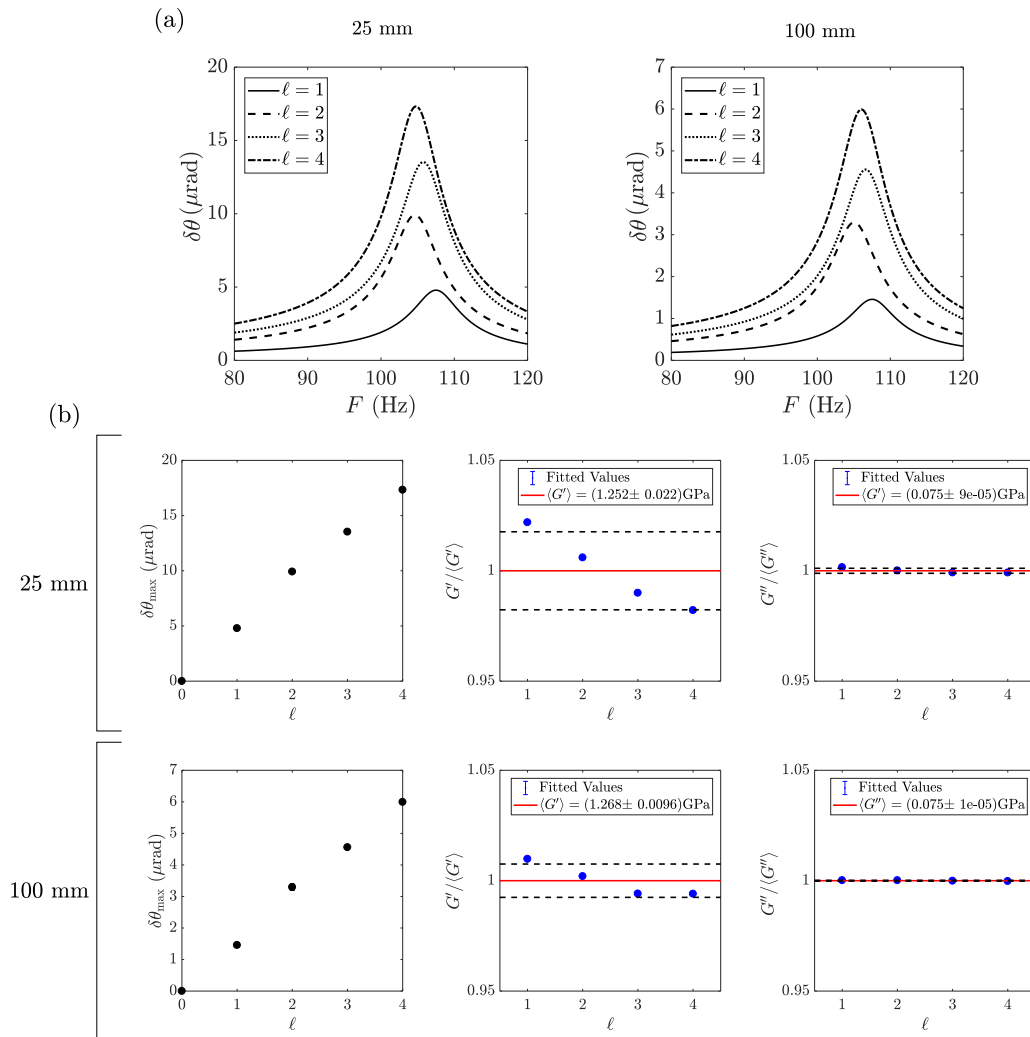


Figure 4.16: (a) Fitted curves angular displacement as a function of frequency for $\ell = 1-4$ in the range of 80-120 Hz for experiments at 25 mm and 100 mm from the transducer. (b) Angular displacement at resonant frequency as a function of ℓ , fitted real and complex shear modulus for different values of ℓ for experiments at 25 mm and 100 mm from the transducer.

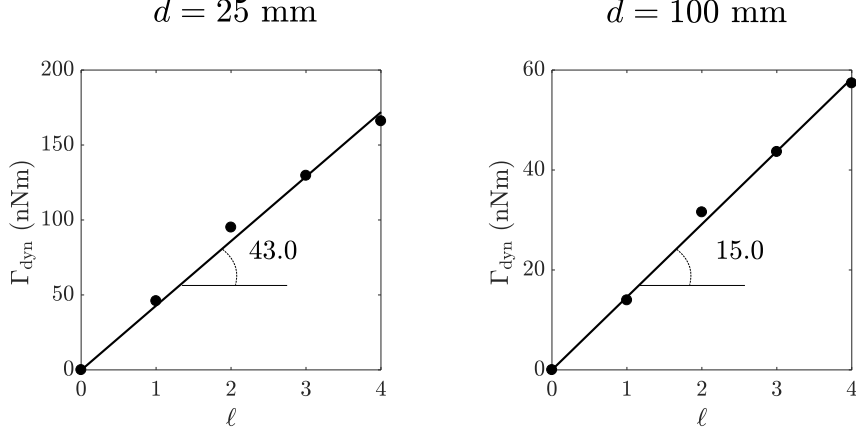


Figure 4.17: Dynamic acoustic torque as a function of the topological charge ℓ for experiments at 25 mm and 100 mm. Solid lines refers to linear adjustment whose corresponding slopes are given in the plots

The final step towards the quantitative assessment of the acoustic radiation torque is to link the measurement of $\delta\theta_{\text{max}}$ with the modulated torque Γ_{dyn} . At first, the idea is to recall their relationship, namely, $\Gamma_{\text{dyn}} = J\Omega_0^2\delta\theta_{\text{max}}$ as expressed in section 4.1. The dependence of Γ_{dyn} as a function of ℓ is shown in Fig. 4.17. Then, we need to link Γ_{dyn} with the intercepted power P by the helical mirror in the absence of modulation, which is eventually compared with the values measured from radiation force experiments, namely, $P = 14.8$ mW at $d = 25$ mm and $P = 7.5$ mW at $d = 100$ mm, see chapter 3.

Recalling that the acoustic intensity is proportional to $\langle V_{\text{mod}}^2 \rangle_T$, see Eq. (4.16), one can express the modulated power intercepted by the helical mirror as

$$P_{\text{mod}}(t) = P \left(1 + \frac{\epsilon^2}{2} \right) + 2\epsilon P \cos(2\pi Ft) + \frac{\epsilon^2}{2} P \cos(4\pi Ft) \quad (4.20)$$

Since we measured only the effect of the F harmonic of the modulated irradiating power when using wavelet transform analysis, we have

$$\Gamma_{\text{dyn}} = \frac{\ell(2\epsilon P)}{\omega} \quad (4.21)$$

The remaining quantity to evaluate is the modulation depth ϵ of the modulated pressure field. This is done by looking at the electrical signal delivered by the piezoelectric sensor, which is proportional to the pressure field. Typical observation at modulation frequency 0 and F are shown in Fig. 4.18(a) at $F = 100$ Hz.

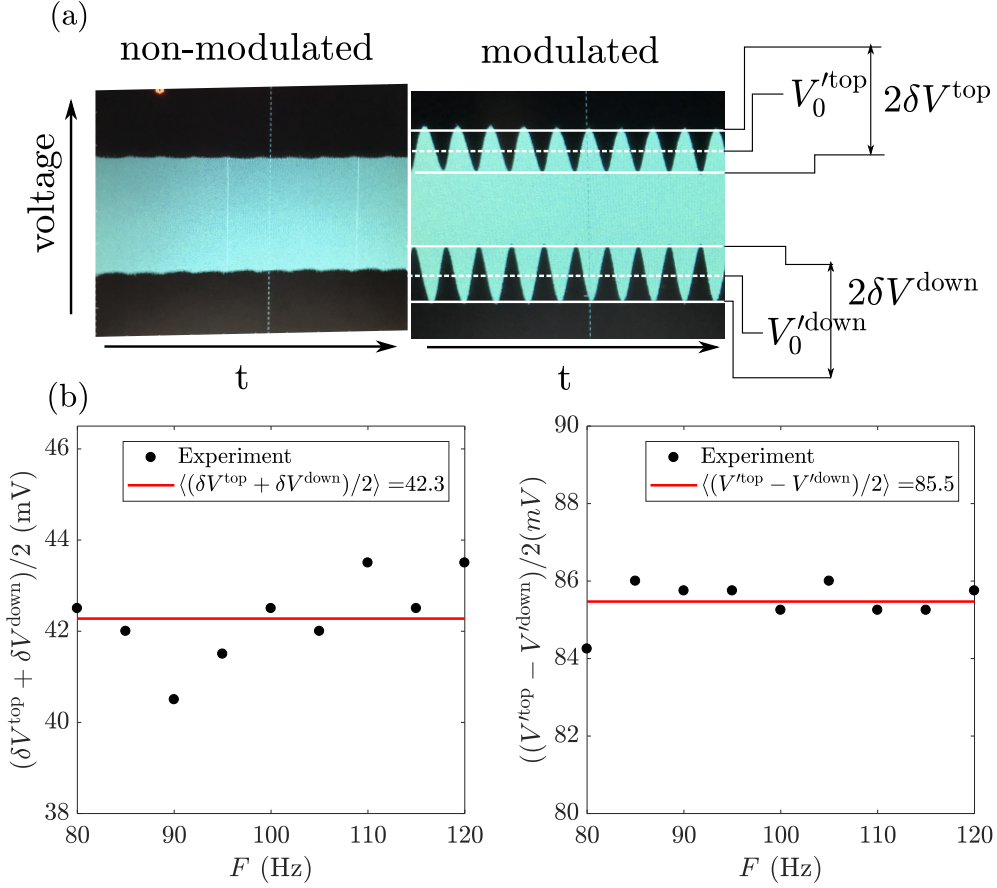


Figure 4.18: (a) Photos of the oscilloscope at non-modulated (left) and modulated (right) pressure field. Values of voltage at constant power V_0 and $2\delta V$ for top and down envelope. (b) values of $(\delta V^{\text{top}} + \delta V^{\text{down}})/2$ and $(V_0'^{\text{top}} - V_0'^{\text{down}})/2$ in the range $80 \text{ Hz} \leq F \leq 120 \text{ Hz}$.

According to the notation introduced in Fig. 4.18(a) we have

$$\epsilon = \frac{(\delta V^{\text{top}} + \delta V^{\text{down}})/2}{(V_0'^{\text{top}} - V_0'^{\text{down}})/2} \quad (4.22)$$

where we account for the top/down asymmetry of the modulator pressure field by averaging the relevant quantity associated with the top/down envelope of the signal. We find $\epsilon = 0.49 \pm 0.01$ over the range of frequencies $80 \leq F \leq 120 \text{ Hz}$, which gives $P = 27.3 \text{ mW}$ for $d = 25 \text{ mm}$ and $P = 9.5 \text{ mW}$ for $d = 100 \text{ Hz}$. Obtained value for $d = 25 \text{ mm}$ is substantially larger than the expected 14.8 mW , which could be attributed to drawback of the cavity effect for such small value of d . However, when the cavity effect can be neglected, which is the case at $d = 100 \text{ mm}$ as discussed in chapter 3, the obtained value departs from the expected value of 7.5 mW by $\sim 30 \%$.

Therefore, we conclude that the pendulum apparatus enables a quantitative measurement of the acoustic radiation torque with a reasonable agreement with respect to the paraxial theory, which was not the case with the spinner approach. The latter fact could be attributed to effects related to the fluid interface, the contact line, and the aperture just above the helical, whose non-trivial impacts on the observed effects have not yet been investigated.

Conclusion and perspectives

In this thesis we reported on our experimental efforts to measure quantitatively the acoustic radiation torque arising from acoustic vortex generation after a sound wave interacts with an helical mirror made of a 3D printed resin. The experiments have been made using ultrasonic waves propagating in the air, which enables dealing with a pure reflective sound-matter process. Such non-dissipative transfer of orbital angular momentum from sound to matter has been treated in the framework of two kinds of independent experiments. First, using freely rotating helical mirror held at an air-fluid interface, which represents an experimental implementation of the idea suggested by Allen et al. [28] in the optical domain that remained so far unrealized whatever the nature of the wave. Second, using a torsional pendulum driven by a modulated acoustic source, which represents the orbital counterpart of the experiment of Beth [27] originally performed to mechanically detect and measure the spin angular momentum of light. In both cases, a quantitative test of the paraxial theory of orbital angular momentum of propagating scalar waves has been made possible owing to complementary acoustic radiation force experiments. It happens that only the pendulum approach enables a satisfying experimental validation of the theory. Now that we have in hands an oscillator driven by the orbital angular momentum of sound, this opens up other experiments where sound could be used to develop sensing applications. To this aim, a relevant improvement to carry out would be to work towards developing enhanced quality factor for the oscillator, which remain modest so far.

Wrinkle Axicons

In this chapter we present the article “Wrinkled axicons: shaping light from cusps” in its totality. This article corresponds to the first project that I developed during my PhD before focusing in the topic of acoustic waves.

Wrinkled axicons: shaping light from cusps

**BENJAMIN SANCHEZ-PADILLA,^{1,2} ALBERTAS ŽUKAUSKAS,³
ARTUR ALEKSANYAN,^{1,2} ARMANDAS BALČYTIS,⁴
MANGIRDAS MALINAUSKAS,³ SAULIUS JUODKAZIS,⁴ AND ETIENNE
BRASSELET^{1,2,*}**

¹*Univ. Bordeaux, LOMA, UMR 5798, F-33400 Talence, France*

²*CNRS, LOMA, UMR 5798, F-33400 Talence, France*

³*Department of Quantum Electronics, Physics Faculty, Vilnius University, Saulėtekio Ave. 10, LT-10223 Vilnius, Lithuania*

⁴*Centre for Micro-Photonics, Faculty of Engineering and Industrial Sciences, Swinburne University of Technology, Hawthorn, VIC 3122, Australia*

**etienne.brasselet@u-bordeaux.fr*

Abstract: We propose a novel class of refractive optical elements by wrinkling the conical surface of a usual (conical) axicon, which leads to geometrical singularities (cusps). Such wrinkled axicons have been fabricated at the micron scale by using three-dimensional femtosecond-laser photopolymerization technique and we report on their experimental and numerical characterization. The beam shaping capabilities of these structures are discussed for both intensity and phase, which includes topological beam shaping that results from azimuthally modulated optical spin-orbit interaction.

© 2016 Optical Society of America

OCIS codes: (350.3950) Micro-optics; (140.3390) Laser materials processing; (260.6042) Singular optics.

References and links

1. S. N. Khonina, V. V. Kotlyar, M. V. Shinkaryev, V. A. Soifer, and G. V. Uspleniev, "The phase rotor filter," *J. Mod. Opt.* **39**, 1147–1154 (1992).
2. J. H. McLeod, "The axicon: a new type of optical element," *J. Opt. Soc. Am.* **44**, 592–592 (1954).
3. O. Ren and R. Birngruber, "Axicon: a new laser beam delivery system for corneal surgery," *IEEE J. Quantum Electron.* **26**, 2305–2308 (1990).
4. D. McGloin and K. Dholakia, "Bessel beams: diffraction in a new light," *Contemp. Phys.* **46**, 15–28 (2005).
5. M. Duocastella and C. B. Arnold, "Bessel and annular beams for materials processing," *Laser Photon. Rev.* **6**, 607–621 (2012).
6. A. Vasara, J. Turunen, and A. T. Friberg, "Realization of general nondiffracting beams with computer-generated holograms," *J. Opt. Soc. Am. A* **6**, 1748–1754 (1989).
7. J. Arlt and K. Dholakia, "Generation of high-order Bessel beams by use of an axicon," *Opt. Commun.* **177**, 297–301 (2000).
8. E. Brasselet, "Optical vortices from closed-loop subwavelength slits," *Opt. Lett.* **103**, 2575–2577 (2013).
9. E. Brasselet, G. Gervinskas, G. Seniutinas, and S. Juodkasis, "Topological shaping of light by closed-path nanoslits," *Phys. Rev. Lett.* **103**, 193901 (2013).
10. M. Malinauskas, A. Zukauskas, S. Hasegawa, Y. Hayasaki, V. Mizeikis, R. Buividas, and S. Juodkasis, "Ultrafast laser processing of materials: from science to industry," *Light Sci. Appl.* **5**, e16133 (2016).
11. A. Ovsianikov, J. Viertl, B. Chichkov, M. Oubaha, B. MacCraith, I. Sakellari, A. Giakoumaki, D. Gray, M. Vamvakaki, M. Farsari, and C. Fotakis, "Ultra-low shrinkage hybrid photosensitive material for two-photon polymerization microfabrication," *ACS Nano* **2**, 2257–2262 (2008).
12. J. Arlt and M. J. Padgett, "Generation of a beam with a dark focus surrounded by regions of higher intensity: the optical bottle beam," *Opt. Lett.* **25**, 191–193 (2000).
13. S. Chavez-Cerda, E. Tepichin, M. A. Meneses-Nava, G. Ramirez, and J. M. Hickmann, "Experimental observation of interfering Bessel beams," *Opt. Express* **3**, 524–529 (1998).
14. D. McGloin, G. Spalding, H. Melville, W. Sibbett, and K. Dholakia, "Three-dimensional arrays of optical bottle beams," *Opt. Commun.* **225**, 215–222 (2003).
15. A. Aleksanyan and E. Brasselet, "Spin-orbit photonic interaction engineering of Bessel beams," *Optica* **3**, 167–174 (2016).
16. K. Y. Bliokh, E. A. Ostrovskaya, M. A. Alonso, O. G. Rodríguez-Herrera, D. Lara, and C. Dainty, "Spin-to-orbital angular momentum conversion in focusing, scattering, and imaging systems," *Opt. Express* **19**, 26132–26149 (2011).

17. K. Y. Bliokh, M. A. Alonso, E. A. Ostrovskaya, and A. Aiello, "Angular momenta and spin-orbit interaction of nonparaxial light in free space," *Phys. Rev. A* **82**, 063825 (2010).
18. P. J. Lavery, D. J. Robertson, G. C. G. Berkhout, G. D. Love, M. J. Padgett, and J. Courtial, "Refractive elements for the measurement of the orbital angular momentum of a single photon," *Opt. Express* **20**, 2110–2115 (2012).
19. M. Mirhosseini, M. Malik, Z. Shi, and R. W. Boyd, "Efficient separation of the orbital angular momentum eigenstates of light," *Nat. Commun.* **4**, 2781 (2012).
20. G. Knöner, S. Parkin, T. A. Nieminen, V. L. Y. Loke, N. R. Heckenberg, and H. Rubinsztein-Dunlop, "Integrated optomechanical microelements," *Opt. Express* **15**, 5521–5530 (2007).
21. E. Brasselet, M. Malinauskas, A. Žukauskas, and S. Juodkazis, "Photo-polymerized microscopic vortex beams generators: precise delivery of optical orbital angular momentum," *Appl. Phys. Lett.* **97**, 211108 (2010).
22. A. Žukauskas, M. Malinauskas, and E. Brasselet, "Monolithic generators of pseudo-nondiffracting optical vortex beams at the microscale," *Appl. Phys. Lett.* **103**, 181122 (2013).

1. Introduction

Lenses are refractive optical elements to focus light and form images. They generally consist of a polished piece of transparent material whose shape defines its use. Spherical lenses correspond to the most popular design where the lens shape is defined by two spherical surfaces. More complex shapes are also common, such as astigmatic lenses whose shape is defined by at least one surface having two distinct radii of curvature. Aspheric lenses are another example where at least one surface has neither spherical nor cylindrical design, which finds use to minimize spherical aberrations. All these cases refer to smooth surface geometries, however some situations imply the use of singular designs such as helical or conical surfaces. The former example refers to refractive spiral phase plates introduced in 1992 [1] that are nowadays widely used to generate optical vortex beams associated with helical wavefronts. The latter case refers to conical lenses, which belong to the family of axicons introduced in 1954 in the context of optical imaging [2].

Unlike usual lenses, axicons are characterized by a long depth of focus defined as $\zeta_0 = w_0/[(n-1)\alpha_0]$ where w_0 is the radius of the beam entering the axicon, n is the refractive index of the axicon, and $\alpha_0 = \arctan(H/R)$ (assumed to be small in the above expression) with H the height of the cone and R the radius of the flat base. Besides imaging applications associated with extended focus region, their practical use also encompasses beam shaping into a ring or the generation of close approximation of non-diffractive Bessel beams, which find many applications such as laser eye surgery [3], optical trapping and optical manipulation [4], or processing of materials [5].

Bessel beams form a family of non-diffractive fields, each element being associated with m th-order Bessel function within the paraxial approximation [4]. In practice, higher-order Bessel beams ($m \geq 0$) can be obtained from Gaussian beams by using binary amplitude masks [6] or from Laguerre-Gaussian beams passing through usual axicons [7]. Here we propose a novel class of higher-order axicons obtained by wrinkling the conical surface of a usual axicon. This is made by introducing cusp deformations of the circular shape of a conical lens, namely hypocycloidal (H) and epicycloidal (E) geometries for the purpose of demonstration. As such, this work can be viewed as the birefringence-free three-dimensional (3D) extension of a previous study dedicated to the topological shaping of light from form-birefringent cuspy metallic nanoslits [8, 9].

2. Design and fabrication

Wrinkled axicons are fabricated at the micron scale by using 3D femtosecond-laser photopolymerization technique [10], the fabrication parameters being given below. This is illustrated in Fig. 1 that displays scanning electron microscope images of H- and E-axicons of various order m that refers to the number of cusps of any cross-section of the optical element in a plane perpendicular to the axicon axis. The corresponding designs are obtained by constructing cones with base (located at $z = 0$) having hypocycloidal or epicycloidal shapes. On the one hand,

H-axicons of order $m \geq 3$ are defined by their surface

$$x_{Hm}(\rho, \theta) = \frac{\rho R}{m} \left\{ (m-1) \cos \theta + \cos[(m-1)\theta] \right\}, \quad (1)$$

$$y_{Hm}(\rho, \theta) = \frac{\rho R}{m} \left\{ (m-1) \sin \theta - \sin[(m-1)\theta] \right\}, \quad (2)$$

$$z_{Hm}(\rho) = (1 - \rho)H, \quad (3)$$

with $0 \leq \theta \leq 2\pi$ and $0 \leq \rho \leq 1$. On the other hand, E-axicons of order $m \geq 1$ are defined by

$$x_{Em}(\rho, \theta) = \frac{\rho R}{m+2} \left\{ (m+1) \cos \theta - \cos[(m+1)\theta] \right\}, \quad (4)$$

$$y_{Em}(\rho, \theta) = \frac{\rho R}{m+2} \left\{ (m+1) \sin \theta - \sin[(m+1)\theta] \right\}, \quad (5)$$

$$z_{Em}(\rho) = (1 - \rho)H, \quad (6)$$

also with $0 \leq \theta \leq 2\pi$ and $0 \leq \rho \leq 1$. Note that the parametrization variable θ should not be confused with the usual azimuthal angle ϕ the (x, y) plane that satisfies $\tan \phi = y/x$.

In practice, various microscopic wrinkled axicons with fixed $R = 50 \mu\text{m}$ are prepared using already well established direct laser writing 3D lithography technique [10] using the SZ2080 material [11] doped with 2 wt% 2-benzyl-2-(dimethylamino)-4'-morpholinobutyrophenone (from Sigma Aldrich) acting as a photoinitiator. The employed setup consisted of femtosecond light source (Pharos, from Light Conversion) with 300 fs pulse width, 515 nm central wavelength, 200 kHz repetition rate and $35 \mu\text{W}$ optical power. Sample translation stages are synchronized with galvanometric-scanner for beam deflection (assembled by Altechna R&D). The beam is focused via microscope objective with magnification $63\times$ and numerical aperture $\text{NA} = 1.4$. The microstructures are realized by writing successive nested shells, which is implemented via 3D Poli software (from Femtika). The first shell is the outer one that is defined by Eqs. (1-6). Inner shells are then written by reducing both R and H by a common factor, the number of steps being dependent on the aspect ratio of the structure. For instance, four shells are enough for $\alpha_0 = 5^\circ$ in order to have fully polymerized structure in its entire volume, hence without need of additional

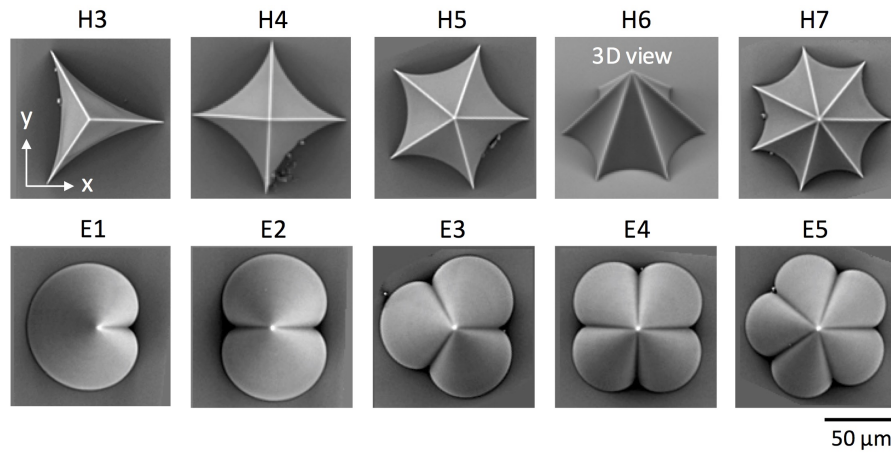


Fig. 1. Scanning electron microscope images of hypocycloidal and epicycloidal axicons of order m , Hm ($m = 3$ to 7) and Em ($m = 1$ to 5), following the designs given by Eqs. (1-6) for $R = 50 \mu\text{m}$ and $H = 50 \mu\text{m}$. All the structures are imaged from top, except H6-axicon that is observed at oblique incidence in order to emphasize the three-dimensional character of the microstructures.

UV post-cure. Prior to direct laser writing, the SZ2080 material [11] is successively heated at 40, 70 and 90°C for 20 min. After exposure, the sample is immersed in 4-methyl-2-pentanone for 1 h. Obtained structures are inspected using scanning electron microscope (Hitachi TM-1000) with no additional deposition of conductive layer. A typical example is given in Fig. 1 in the case $R = H$, hence $\alpha_0 = 45^\circ$ while further optical characterization is made for smaller values of α_0 , namely $\alpha_0 = 5^\circ$ and 15° .

3. Optical characterization

3.1. Far-field analysis

Beam shaping capabilities of wrinkled axicons H_m ($3 \leq m \leq 6$) and E_m ($1 \leq m \leq 3$) with $R = 50 \mu\text{m}$ are experimentally assessed, first by determining their angular spectrum. This is done by placing the sample in the focal plane of a lens illuminated by a Gaussian laser beam at wavelength $\lambda = 633 \text{ nm}$. Obtained beam waist radius at $\exp(-2)$ from its maximum intensity is $w_0 = 20 \mu\text{m}$. Then Fourier transform of the latter plane is realized by using microscope objective ($100\times$, $\text{NA} = 0.8$) whose back focal plane is imaged on a camera using a relay lens. Results are shown for $\alpha_0 = 15^\circ$ in the second line of Fig. 2, where the first line corresponds to direct natural light imaging of the structures. In contrast to usual axicons that are characterized by ring shape Fourier spectrum, one obtains non-closed-path spectra for wrinkled axicons that are characterized by an azimuthally dependent angle $\alpha(\phi) \neq \alpha_0$ whose expression in the limit of small α_0 is

$$\alpha_{Xm}(\phi) = \frac{\alpha_0 R}{\left[x_{Xm}^2(1, \theta(\phi)) + y_{Xm}^2(1, \theta(\phi)) \right]^{1/2}}, \quad (7)$$

with $X = (H, E)$. Experimental data is compared to simulations in the third line of Fig. 2 that shows the far-field intensity pattern I_{FF} associated with the 2D Fourier transform of the field in the plane of the sample neglecting the diffraction inside the optical element. Namely,

$$I_{\text{FF}} \propto \left| \text{FFT} \left[t_{Xm}(r, \phi) \exp(-r^2/w_0^2) \right] \right|^2, \quad (8)$$

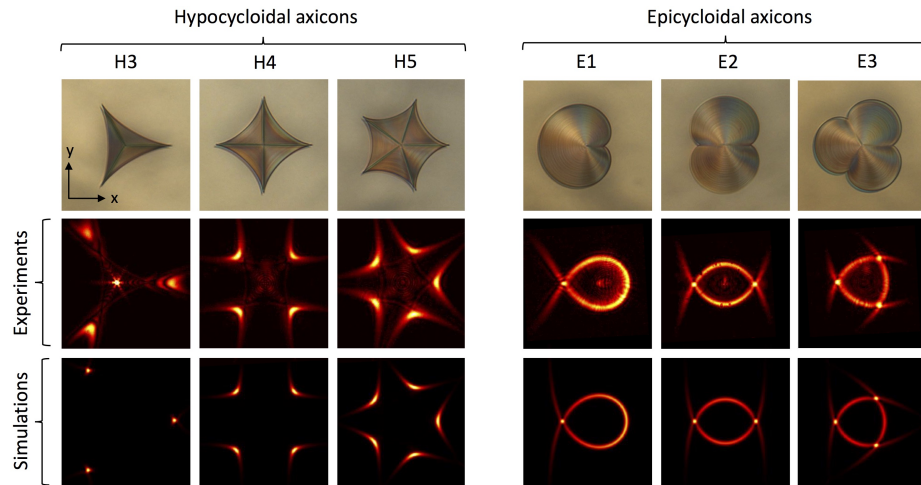


Fig. 2. Upper line: natural light imaging of a set a wrinkled axicons of hypocycloidal and epicycloidal types. Middle line: far field intensity distribution obtained by Fourier transform with a microscope objective for $R = 50 \mu\text{m}$ and $\alpha_0 = 15^\circ$. Bottom line: simulations from fast Fourier transform of the field just after the structure neglecting diffraction, see Eqs. (7) and (8).

where $k = 2\pi/\lambda$, $n = 1.5$, FFT refers to 2D fast Fourier transform, and

$$t_{Xm}(r, \phi) = \exp[-ikr(n-1)\alpha_{Xm}(\phi)] \quad (9)$$

is the complex amplitude transmittance mask of the wrinkled axicon Xm . Fair agreement between experimental data and calculations is obtained though we note the presence of unexpected non-zero on-axis intensity that is more pronounced for lowest-order wrinkled axicons. This can be understood noting that the incident Gaussian beam tail leaks out of the finite-size structure.

3.2. Propagation analysis: scalar treatment

The propagation behavior is retrieved by imaging the intensity distribution at distance z from the sample by translating a microscope objective ($100\times$, $NA = 0.8$) along the z axis, the distance between objective and camera being kept constant. Experimental data are shown in Fig. 3 both for hypocycloidal and epicycloidal axicons, where the propagation distance is normalized to the azimuth-averaged depth of focus

$$\zeta_{Xm} = \frac{\zeta_0}{2\pi} \int_0^{2\pi} \frac{\alpha_0}{\alpha_{Xm}(\phi)} d\phi. \quad (10)$$

Observations are compared to simulations in Fig. 3 by using scalar beam propagation method based on 2D fast Fourier transform. Namely, the intensity pattern at z , $I(x, y, z)$, is evaluated following

$$I \propto \left| \text{FFT}^{-1} \left\{ \exp(ik_z z) \text{FFT} \left[t_{Xm}(r, \phi) \exp(-r^2/w_0^2) \right] \right\} \right|^2, \quad (11)$$

where FFT^{-1} refers to 2D inverse fast Fourier transform and $\exp(ik_z z)$, with $k_z = (k^2 - k_x^2 - k_y^2)^{1/2}$, is the propagation operator in the Fourier domain. Overall agreement is obtained whatever the propagation distance. Note that observed differences at $z = 0$ are merely due to the fact

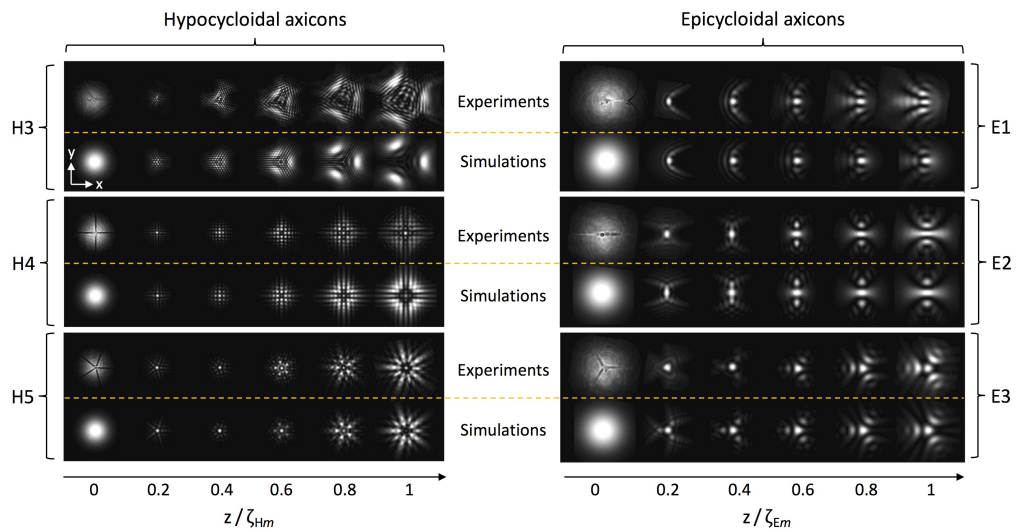


Fig. 3. Propagation analysis for a set of wrinkled axicons of hypocycloidal and epicycloidal types for $R = 50 \mu\text{m}$ and $\alpha_0 = 5^\circ$. For each structure, experimental intensity patterns in the (x, y) plane as a function of normalized propagation distance z/ζ_{Xm} are compared to beam propagation method following Eq. (11). All images are normalized to their maximal values in order to appreciate the intensity patterns despite overall intensity decrease with z .

that 3D optical elements are modeled by 2D phase masks, which prevents by construction the observation of the ridges of wrinkled axicons in the simulations.

In particular, on-axis intensity modulation may be interesting in the field of optical manipulation, in the context of so-called optical bottles [12] that refer to null intensity surrounded by bright regions in 3D. See for instance the sequence of intensity patterns at $z/\zeta_{H4} = (0.4, 0.6, 0.8)$ for H4-axicon. This is explored more quantitatively by plotting the on-axis intensity distribution, as shown in Fig. 4(a) for a set of Hm -axicons with $w_0 = 20 \mu\text{m}$, which indicates that higher-order hypocycloidal axicons are not favorable for on-axis intensity modulation. On the other hand, the number of oscillations increases with the incident beam waist, as shown in Fig. 4(b) for $w_0 = 20, 40$ and $60 \mu\text{m}$. Arguably, the contrast of on-axis intensity modulation is not optimal, still there are a few other better strategies to generate optical bottle arrays. One can mention the use of interferences between two Bessel beams [13], the use of Laguerre-Gaussian beams with higher-order radial index passing through usual axicon [14] or more recently the use of a birefringent axicon [15].

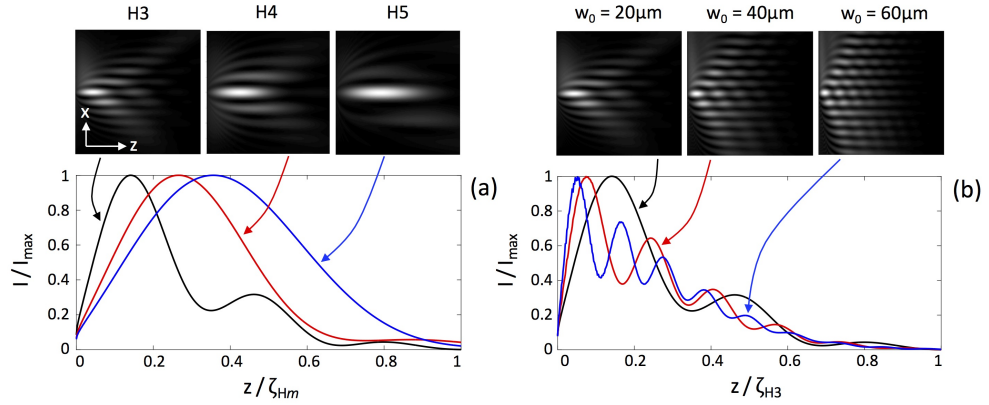


Fig. 4. (a) Calculated on-axis intensity as a function of the propagation distance for wrinkled axicons H3 (black curve), H4 (red curve) and H5 (blue curve) with $R = 50 \mu\text{m}$, $\alpha_0 = 5^\circ$ and $w_0 = 20 \mu\text{m}$. (b) Same as in panel (a) for H3-axicon and incident beam waist $w_0 = 20, 40$ and $60 \mu\text{m}$. For both panels, upper images correspond to the corresponding intensity patterns in the plane (x, z) for $-20 \mu\text{m} \leq x \leq 20 \mu\text{m}$ and $0 \leq z/\zeta_{Hm} \leq 1$.

3.3. Propagation analysis: full vectorial treatment

Although above intensity spatial modulation along the three spatial coordinates obtained within a scalar approach provides with a satisfying zero-order description of the field in the limit of small α_0 angle, the scalar approach misses beam shaping features associated with the vectorial nature of light. Indeed, it is known that focusing (i.e., nonparaxiality) is associated with spin-orbit interaction of light [16]. In the present case the focusing properties of the wrinkled axicons are azimuthally modulated as a consequence of the ϕ -dependent apex of the structures. We thus expect azimuthal features associated with the vectorial nature of light. This is investigated by performing numerical simulations of the propagation of light at the output of the structures by using a FDTD software package (FDTD Solutions, Lumerical Solutions, Inc.). The simulations do not only take into account the 3D character of the optical field, they also consider the 3D nature of the structures in contrast to scalar approach that describes the 3D structures as 2D phase masks. Practically, numerical analysis is performed for wrinkled axicons with $R = 10, 15$ and $20 \mu\text{m}$ and $\alpha_0 = 10^\circ, 15^\circ$ and 20° under plane wave illumination along the z axis. Also, we impose almost null transmission for the incident light outside the basis of the structure at $z = 0$

by placing there a perfect electrical conductor. This leads to define the azimuth-averaged depth of focus as $\zeta'_0 = R/[(n-1)\alpha_0]$ for a regular axicon and

$$\zeta'_{Xm} = \frac{\zeta'_0}{2\pi} \int_0^{2\pi} \frac{\alpha_0^2}{\alpha_{Xm}^2(\phi)} d\phi \quad (12)$$

for a Xm -axicon. The case of an arbitrary uniform incident polarization state is constructed by exploiting the linear superposition principle from two basic simulations performed for each structure, namely by using x -polarized and y -polarized incident light. In addition, the simulation box $x \times y \times z$ dimensions are $2R \times 2R \times \zeta'_{Xm}$ and perfectly matched layer is placed at its surface boundary, which prevents from unwanted effects that may arise from finite-size calculation volume and from the way the opaque mask outside the structure basis at $z = 0$ is modeled, namely by a material with refractive index $710 + i710$.

Here we consider both left- and right-handed circular polarization states described by the unit vectors $(\mathbf{x} + \sigma i\mathbf{y})/\sqrt{2}$ with helicity $\sigma = \pm 1$. Indeed, such cases allow clear identification of nonparaxial manifestation of spin-orbit interaction of light, as illustrated in the well-known situation of a regular axicon [17] whose results are illustrated in the first line of Fig. 5 for

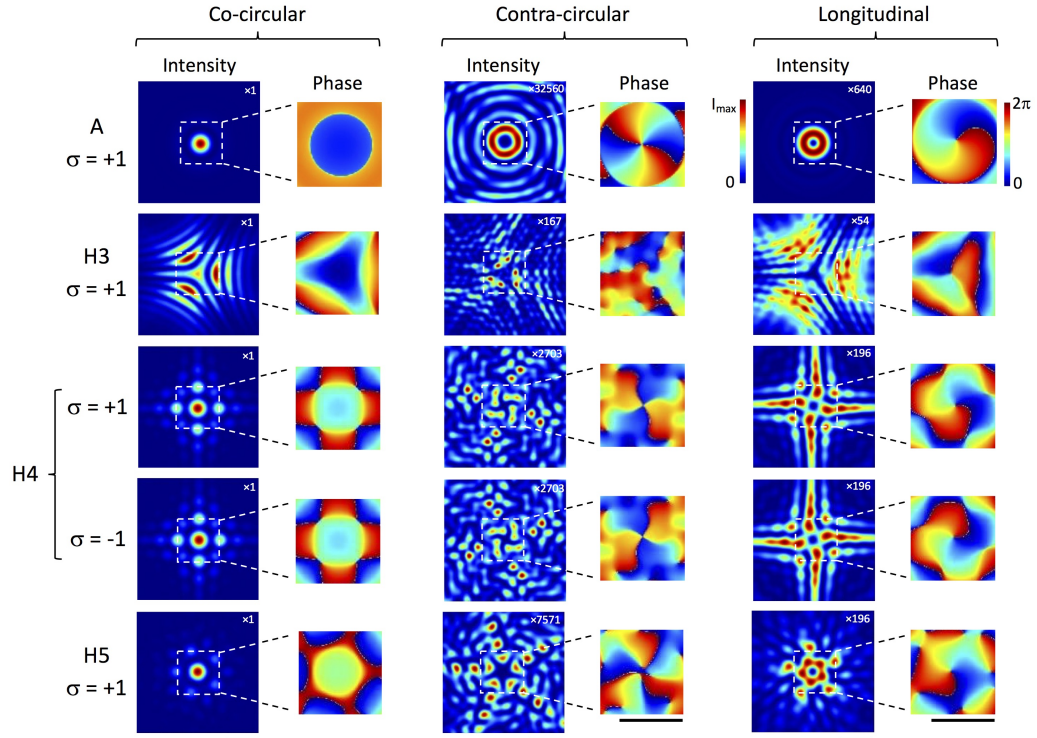


Fig. 5. FDTD simulations of the vectorial content of light in the plane located at a distance $z = \zeta'_{Hm}/2$ from the basis of a regular axicon (A) and hypocycloidal axicons H3, H4 and H5 in the case $R = 10 \mu\text{m}$ and $\alpha_0 = 10^\circ$. See text for details on simulations parameters. Incident field in a circularly polarized plane wave with helicity $\sigma = +1$, the case $\sigma = -1$ being also shown for H4 structure. Both intensity and phase of co-circularly (σ polarized), contra-circular ($-\sigma$ polarized) and longitudinal (z polarized) components of the output light field. Scale bar at the bottom of each column refers to $5 \mu\text{m}$. The factor indicated on intensity panels refers to the ratio between the maximal intensity of the considered field component and of the co-circular component.

$\sigma = +1$, $R = 10 \mu\text{m}$ and $\alpha_0 = 10^\circ$. Namely, the contra-circularly polarized component of the output light field carries on-axis optical phase singularity with topological charge $\ell = 2\sigma$, as seen from the phase pattern that has an azimuthal dependence of the form $\ell\phi$. In addition, the longitudinal field component carries a phase singularity with charge $\ell = \sigma$. We note that the residual (unexpected [17]) broken axisymmetry of the intensity pattern of the contra-circular component is due to the square-shaped cross-section of the simulation box.

The situation is rather different for wrinkled axicons, as illustrated in Fig. 5 for hypocycloidal axicons Hm with $m = (3, 4, 5)$ also for $\sigma = +1$, $R = 10 \mu\text{m}$ and $\alpha_0 = 10^\circ$. Indeed, the circulation of the phase around the z axis nearby the z axis now depends on the order m of the axicon, namely we have $\ell = \sigma(2 - m)$. This implies a m -dependent optical spin-orbit interaction that echoes previous work on 2D form-birefringent cuspy metallic nanoslits [8, 9]. Indeed it was shown that hypocycloidal nanoslits are associated with the generation of optical phase singularities with topological charge $\ell = \sigma(2 - m)$ for the contra-circular component of the output light field, as observed here for 3D birefringence-free cuspy structures. Moreover, the helicity-dependent manifestation of the spin-orbit interaction is also checked, see Fig. 5 in the case of H4-axicon whose behavior is presented both for $\sigma = \pm 1$. Still, we note that higher-order structures eventually lead to splitting of the on-axis high-charge singularity as observed in the case of nanoslits [8, 9].

For epicycloidal geometries, the expected topological charge for the contra-circular component is $\ell = \sigma(2 + m)$ [8, 9], however on-axis higher-order topological diversity was shown not to follow such a behavior due to string translational symmetry breaking and ensuing substantial splitting of high-charge vortices. Similarly conclusions are obtained for Em -axicons. Finally, we note that our full set of simulations shows that the use of higher values of either R or α_0 also leads to high-charge splitting.

4. Conclusion

Wrinkled axicons represent a step in the conception of 3D optical elements endowed with cusps. To date, one can mention transformation-optics 3D refractive optical element enabling the measurement and sorting of orbital angular momentum of light [18, 19]. The use of cuspy designs has also been proposed previously with 2D nanoslits used to generate optical vortices from spin-orbit interaction of light owing to azimuthally varying form birefringence [8, 9]. In the context of singular optics, the particular case of hypocycloid and epicycloid curves considered here also brings spin-orbit interaction features that are associated with nonparaxiality instead of anisotropy. In addition, from the micro-optical component point of view, the fabrication of microscopic wrinkled axicons extends the set of singular optical elements fabricated by 3D direct laser writing, which was restricted so far to spiral phase plates and usual axicons [20–22].

Funding

French State managed by the French National Research Agency (ANR) in the frame of the Investments for the future Programme IdEx Bordeaux LAPHIA (ANR-10-IDEX-03-02), CONACYT Mexico, and NATO grant number SPS-985048.

Acknowledgments

Authors acknowledge the access to the swinSTAR supercomputer at Swinburne University of Technology that has been used to perform the FDTD simulations

Bibliography

- [1] B. SANCHEZ-PADILLA, A. ŽUKAUSKAS, A. ALEKSANYAN, A. BALČYTIS, M. MALINAUSKAS, S. JUODKAZIS, AND E. BRASSELET, “Wrinkled axicons: shaping light from cusps”, *Optics Express* **24**, 24075 (2016).
- [2] E. BRASSELET, “Optical vortices from closed-loop subwavelength slits”, *Optics Letters* **38**, 2575 (2013).
- [3] Y. SHEN, X. WANG, Z. XIE, C. MIN, X. FU, Q. LIU, M. GONG, AND X. YUAN, “Optical vortices 30 years on: OAM manipulation from topological charge to multiple singularities”, *Light: Science & Applications* **8**, 90 .
- [4] C. R. BENTLEY, “Secular increase of gravity at South Pole station”, *Antarctic Snow and Ice Studies II* **16**, 191 (1971).
- [5] G. D. Q. ROBIN *et al.*, “Radio echo exploration of the Antarctic ice sheet”, *International Association of Scientific Hydrology Publication* **86**, 97 (1970).
- [6] J. NYE, R. KYTE, AND D. THRELFALL, “Proposal for measuring the movement of a large ice sheet by observing radio echoes”, *Journal of Glaciology* **11**, 319 (1972).
- [7] J. F. NYE AND M. V. BERRY, “Dislocations in wave trains”, *Proceedings of the Royal Society of London. A. Mathematical and Physical Sciences* **336**, 165 (1974).
- [8] N. BARANOVA AND B. Y. ZEL’DOVICH, “Dislocations of the wave-front surface and zeros of the amplitude”, *Zh. Eksp. Teor. Fiz.* **80**, 1789 (1981).
- [9] N. BARANOVA, B. Y. ZEL’DOVICH, A. MAMAEV, N. PILIPETSKY, AND V. SHKUNOV, “Dislocation density of the wave front with a speckle structure of the light fields”, *JETP Lett.* **83**, 1702 (1982).

-
- [10] N. BARANOVA, A. MAMAEV, N. PILIPETSKY, V. SHKUNOV, AND B. Y. ZEL'DOVICH, "Wave-front dislocations: topological limitations for adaptive systems with phase conjugation", *Journal of the Optical Society of America* **73**, 525 (1983).
- [11] O. BRYNGDAHL, "Radial-and circular-fringe interferograms", *Journal of the Optical Society of America* **63**, 1098 (1973).
- [12] S. KHONINA, V. KOTLYAR, M. SHINKARYEV, V. SOIFER, AND G. USPLENIEV, "The phase rotor filter", *Journal of Modern Optics* **39**, 1147 (1992).
- [13] M. KRISTENSEN, M. BEIJERSBERGEN, AND J. WOERDMAN, "Angular momentum and spin-orbit coupling for microwave photons", *Optics Communications* **104**, 229 (1994).
- [14] M. BEIJERSBERGEN, R. COERWINKEL, M. KRISTENSEN, AND J. WOERDMAN, "Helical-wavefront laser beams produced with a spiral phaseplate", *Optics Communications* **112**, 321 (1994).
- [15] A. G. PEELE *et al.*, "Observation of an x-ray vortex", *Optics Letters* **27**, 1752 (2002).
- [16] F. TAMBURINI, E. MARI, A. SPONSELLI, B. THIDÉ, A. BIANCHINI, AND F. ROMANATO, "Encoding many channels on the same frequency through radio vorticity: first experimental test", *New Journal of Physics* **14**, 033001 (2012).
- [17] K. MIYAMOTO, K. SUIZU, T. AKIBA, AND T. OMATSU, "Direct observation of the topological charge of a terahertz vortex beam generated by a Tsurupica spiral phase plate", *Applied Physics Letters* **104**, 261104 (2014).
- [18] B. T. HEFNER AND P. L. MARSTON, "An acoustical helicoidal wave transducer with applications for the alignment of ultrasonic and underwater systems", *The Journal of the Acoustical Society of America* **106**, 3313 (1999).
- [19] S. GSPAN, A. MEYER, S. BERNET, AND M. RITSCH-MARTE, "Optoacoustic generation of a helicoidal ultrasonic beam", *The Journal of the Acoustical Society of America* **115**, 1142 (2004).

-
- [20] R. WUNENBURGER, J. I. V. LOZANO, AND E. BRASSELET, “Acoustic orbital angular momentum transfer to matter by chiral scattering”, *New Journal of Physics* **17**, 103022 (2015).
- [21] N. HECKENBERG, R. MCDUFF, C. SMITH, AND A. WHITE, “Generation of optical phase singularities by computer-generated holograms”, *Optics Letters* **17**, 221 (1992).
- [22] I. BASISTIY, V. Y. BAZHENOV, M. SOSKIN, AND M. V. VASNETSOV, “Optics of light beams with screw dislocations”, *Optics Communications* **103**, 422 (1993).
- [23] H. LAROCQUE, I. KAMINER, V. GRILLO, G. LEUCHS, M. J. PADGETT, R. W. BOYD, M. SEGEV, AND E. KARIMI, “‘Twisted’ electrons”, *Contemporary Physics* **59**, 126 (2018).
- [24] C. W. CLARK, R. BARANKOV, M. G. HUBER, M. ARIF, D. G. CORY, AND D. A. PUSHIN, “Controlling neutron orbital angular momentum”, *Nature* **525**, 504 (2015).
- [25] A. SADOWSKY, “Ponderomotive action of electromagnetic and light waves on crystals”, *Part I: Theory Acta et Commentationes imp. Universitatis Jurievensis* **7**, n1 (1899).
- [26] J. H. POYNTING, “The wave motion of a revolving shaft, and a suggestion as to the angular momentum in a beam of circularly polarised light”, *Proceedings of the Royal Society of London. Series A, Containing Papers of a Mathematical and Physical Character* **82**, 560 (1909).
- [27] R. A. BETH, “Mechanical detection and measurement of the angular momentum of light”, *Physical Review* **50**, 115 (1936).
- [28] L. ALLEN, M. W. BEIJERSBERGEN, R. SPREEUW, AND J. WOERDMAN, “Orbital angular momentum of light and the transformation of Laguerre-Gaussian laser modes”, *Physical Review A* **45**, 8185 (1992).
- [29] M. PADGETT AND R. BOWMAN, “Tweezers with a twist”, *Nature Photonics* **5**, 343 (2011).

-
- [30] B. T. HEFNER AND P. L. MARSTON, “Acoustical helicoidal waves and Laguerre-Gaussian beams: Applications to scattering and to angular momentum transport”, *The Journal of the Acoustical Society of America* **103**, 2971 (1998).
- [31] J.-L. THOMAS AND R. MARCHIANO, “Pseudo angular momentum and topological charge conservation for nonlinear acoustical vortices”, *Physical Review Letters* **91**, 244302 (2003).
- [32] J. LEKNER, “Acoustic beams with angular momentum”, *The Journal of the Acoustical Society of America* **120**, 3475 (2006).
- [33] K. VOLKE-SEPÚLVEDA, A. O. SANTILLÁN, AND R. R. BOULLOSA, “Transfer of angular momentum to matter from acoustical vortices in free space”, *Physical Review Letters* **100**, 024302 (2008).
- [34] K. SKELDON, C. WILSON, M. EDGAR, AND M. PADGETT, “An acoustic spanner and its associated rotational Doppler shift”, *New Journal of Physics* **10**, 013018 (2008).
- [35] Y. LI, G. GUO, J. TU, Q. MA, X. GUO, D. ZHANG, AND O. A. SAPOZHNIKOV, “Acoustic radiation torque of an acoustic-vortex spanner exerted on axisymmetric objects”, *Applied Physics Letters* **112**, 254101 (2018).
- [36] A. ANHÄUSER, R. WUNENBURGER, AND E. BRASSELET, “Acoustic rotational manipulation using orbital angular momentum transfer”, *Physical Review Letters* **109**, 034301 (2012).
- [37] C. E. DEMORE, Z. YANG, A. VOLOVICK, S. COCHRAN, M. P. MACDONALD, AND G. C. SPALDING, “Mechanical evidence of the orbital angular momentum to energy ratio of vortex beams”, *Physical Review Letters* **108**, 194301 (2012).
- [38] W. LI, M. KE, S. PENG, F. LIU, C. QIU, AND Z. LIU, “Rotational manipulation by acoustic radiation torque of high-order vortex beams generated by an artificial structured plate”, *Applied Physics Letters* **113**, 051902 (2018).

-
- [39] D. BARESCH, J.-L. THOMAS, AND R. MARCHIANO, “Orbital angular momentum transfer to stably trapped elastic particles in acoustical vortex beams”, *Physical review letters* **121**, 074301 (2018).
- [40] K. G. FOOTE, “Discriminating between the nearfield and the farfield of acoustic transducers”, *The Journal of the Acoustical Society of America* **136**, 1511 (2014).
- [41] Y. G. OVSEENKO, “Refined formulas for the resistance torque of an ellipsoid of revolution and a circular disk rotating in an infinite incompressible viscous fluid”, *Fluid Dynamics* **4**, 100 (1969).
- [42] N.-S. CHENG, “Formula for the viscosity of a glycerol- water mixture”, *Industrial & engineering chemistry research* **47**, 3285 (2008).
- [43] J. T. CANTRELL *et al.*, “Experimental characterization of the mechanical properties of 3D-printed ABS and polycarbonate parts”, *Rapid Prototyping Journal* **23**, 811 (2017).